NTNU

Norwegian University of
Science and Technology

Finite temperature *ab initio* simulations of the lattice thermal conductivity of XNiBi, X=(Sc, Y, La), based half-Heuslers

Ingeborg Treu Røe

Nanotechnology
Submission date: June 2017
Supervisor: Sverre Magnus Selbach, IMA
Co-supervisor: Ole Martin Løvvik, SINTEF / UiO

Norwegian University of Science and Technology
Department of Materials Science and Engineering

Summary

Over the past few years, the half-Heusler materials have attracted attention for their potential within thermoelectric applications. This is mainly due to the flexibility of half-Heusler crystal structure. The half-Heuslers comprise three elements, XYZ, that crystallize in the face-centered cubic structure F$\bar{4}$3m. Thus, materials that comprise nontoxic, environmentally friendly, inexpensive and abundant elements are possible. Moreover, many of these half-Heuslers are low band gap semiconductors with good electrical properties, making them attractive for thermoelectric applications. On the other hand, the half-Heuslers are associated with too high lattice thermal conductivity to be applicable as thermoelectric materials. However, previous studies suggest that the lattice thermal conductivity may be reduced through materials' engineering, where two of the most common methods proposed in literature are alloying on one of the atomic sites, and nanostructuring.

Consequently, the present work investigates the effect of alloying on the X-position relative to the Bi-position of XNiBi, X=(Sc, Y or La), based half-Heuslers using density functional theory together with the temperature dependent effective potential method. The different half-Heusler alloys are described within the virtual crystal approximation, and the lattice thermal conductivity is calculated with the Boltzmann transport equation within the relaxation time approximation. This enables independent investigations of different contributions to the lattice thermal conductivity. In the $Sc_xY_yLa_{1-x-y}NiBi$ alloys, the minimum lattice thermal conductivity was calculated to 4.3 W/mK for $Sc_{0.24}La_{0.76}NiBi$ even though the maximum mass-disorder occurs for higher concentrations of Sc. This behaviour may be explained by the dominance of the anharmonic contributions to the lattice thermal conductivity. Consistent with the results from the specialization project, increasing the concentration of La in $Sc_xY_yLa_{1-x-y}NiBi$ was shown to increase the anharmonic scattering of the acoustic phonon modes. Since the mass-disorder in $Sc_xY_yLa_{1-x-y}NiBi$ primarily targets the optic phonon modes, which carry less heat than the acoustic, the alloying on the X-position does not reduce the lattice thermal conductivity efficiently. Alloying on the Bi-position of YNiBi with As or Sb, on the other hand, targets the acoustic phonon modes. Thus, the lattice thermal conductivity is reduced to 2.4 W/mK in $YNiBi_{0.36}As_{0.64}$. The impact of the scattering of acoustic phonon modes on the lattice thermal conductivity is further emphasized in the nanostructured materials. Through a simple model for grain boundary scattering, nanoscaled grains were introduced to the bulk materials such that the acoustic phonon modes were targeted. Consequently, in the $Sc_xLa_{1-x}NiBi$ binary alloy with grains of 50 nm in diameter, the minimum lattice thermal conductivity is reduced with more than 45% compared to the minimum value of the bulk alloys; from 4.3 W/mK for $Sc_{0.24}La_{0.76}NiBi$ to 2.4 W/mK for $Sc_{0.5}La_{0.5}NiBi$.

The present work indicates that the lattice thermal conductivity of XNiBi, X=(Sc, Y or La), based half-Heuslers may be reduced sufficiently through nanostructuring and alloying to be competitive with state-of-the-art thermoelectric materials. Moreover, the understanding of how different mechanisms influence the lattice thermal conductivity achieved in this work may aid the continued progress of the performance of thermoelectric materials.

Sammendrag

Halv-Heuslere har i løpet av de siste årene tiltrukket seg mye oppmerksomhet fordi de egner seg som termoelektriske materialer. Det er den fleksible strukturen til halv-Heuslerne gir disse ettertraktede egenskapene. Strukturen består av tre elementer, XYZ, som krystallisereres i den flatesentrerte kubiske krystallstrukturen, $F\bar{4}3m$. Mange ulike elementer kan inngå i denne strukturen. Følgelig finnes det flere halv-Heuslere som er bygget opp av lite giftige, miljøvennlige og billige grunnstoffer. I tillegg er ofte halv-Heuslere halvledere med smalt båndgap, og dermed gode elektriske egenskaper. Derfor kan de egne seg for bruk i termoelektriske elementer. På den andre siden har de relativt høy termisk gitterledningsevne. Dette fører til at de er lite effektive som termoelektriske materialer. Likevel viser tidligere studier at gitterledningsevnen kan reduseres ved hjelp av målrettet materialdesign, der de to mest brukte metodene i litteraturen baserer seg på substitusjon av et av elementene i halv-Heusleren med et fremmedelement, og på nanostrukturering av bulkmaterialet.

I denne masteroppgaven blir den relative effekten av substitusjon på X-plassen kontra Bi-plassen i halv-Heuslere basert på XNiBi, X=(Sc, Y eller La), undersøkt ved hjelp av temperatureavhengige *ab initio* simuleringer. De ulike halv-Heuslerlegeringene er beskrevet innenfor en virtuell krystalltilnærming, og den termiske gitterledningsevnen beregnet ved hjelp av Boltzmanns transportligning og relaksasjonstidtilnærmingen. Dermed kan uavhengige undersøkelser av ulike bidrag til den termiske gitterledningsevnen gjennomføres. I $Sc_xY_yLa_{1-x-y}NiBi$ ble den minste termiske gitterledningsevnen på 4.3 W/mK beregnet for $Sc_{0.24}La_{0.76}NiBi$ til tross for at det er mer uorden på X-plassen ved høyere konsentrasjoner av Sc. Resultatene indikerer at fonon-fonon (uharmoniske) bidragene dominerer den termiske gitterledningsevnen. I tråd med funnene i prosjektoppgaven, fører en økning av La-konsentrasjonen i $Sc_xY_yLa_{1-x-y}NiBi$ til økt fonon-fonon spredning av de akustiske fononmodene. Masse-uordensspredningen, derimot, retter seg i første rekke mot de optiske fononmodene, som leder mindre varme enn de akustiske. Følgelig har substitusjon på X-plassen av XNiBi, X=(Sc, Y eller La), liten effekt på den termiske gitterledningsevnen. Substitusjon av Bi med As eller Sb, derimot, fører til spredning av de akustiske modene. Dermed kan den termiske ledningsevnen effektivt reduseres til 2.4 W/mK i $YNiBi_{0.36}As_{0.64}$. Betydningen av å spre de akustiske fononmodene er understreket i beregningene av den termiske gitterledningsevnen til de nanostrukturerte materialene. Korn med diameter på 50 nm ble introdusert i materialene. Ved hjelp av en enkel modell for spredning av fononer på korngrenser, ble den påfølgende spredningen av de akustiske fononmodene inkludert i beregningene slik at den minste termiske gitterledningsevnen i $Sc_xLa_{1-x}NiBi$-legeringen ble redusert med 45% i forhold til den minste termiske ledningsevnen til bulklegeringen. Det vil si at en reduksjon fra 4.3 W/mK i $Sc_{0.24}La_{0.76}NiBi$ til 2.4 W/mK i $Sc_{0.55}La_{0.45}NiBi$ ble observert.

Resultatene i denne oppgaven indikerer at den termiske gitterledningsevnen til XNiBi, X=(Sc, Y or La), baserte halv-Heuslere kan reduseres tilstrekkelig ved hjelp av legering og nanostrukturering til at materialene er konkurransedyktige med kommersialiserte termoelektriske materialer. I tillegg er en innsikt i hvordan ulike mekanismer påvirker den termiske gitterledningsevnen oppnådd. Denne innsikten kan bidra til den forsatte utviklingen av egenskapene til termoelektriske materialer.

Preface

This master thesis have been carried out at the Norwegian University of Science and Technology (NTNU) at the Department of Material Science and Engineering as a part of my master's degree in nanotechnology. The present work is a continuation of my specialization project, *DFT simulations of phonon propagation in the thermoelectric half-Heusler XNiBi (X = Sc, Y or La)*, that was conducted during the fall of 2016. The specialization and master project has been supervised by Assoc. Professor Sverre M. Selbach at NTNU and Professor II Ole Martin Løvvik at the University of Oslo (UiO). The idea behind the projects is credited to Professor II Ole Martin Løvvik. Since this is a continuation of the specialization project, parts of the theory have been improved and reused in this thesis.

Acknowledgements

I would like to give a warm thanks to both on my supervisors, Sverre M. Selbach and Ole Martin Løvvik, for their valuable guidance and close follow up throughout the course of this project. Their dedication, time and knowledge have been of great importance to the progress of the project. A special thanks to Sverre for the financial support, allowing me to visit Ole Martin in Oslo.

I would also like to extend my appreciation to PhD candidate Simen Eliassen for his help and feedback on the results achieved in the present project. In addition, I thank the members of the inorganic materials group and the DFT group at the Department of Materials Science for many fruitful discussions and good feedback on my work.

Ingeborg Treu Røe
Trondheim, June, 2017

Contents

List of Tables

List of Figures

Abbreviations

AIMD *ab initio* molecular dynamics

BTE Boltzmann transport equation

BZ Brillouin zone

DFT density functional theory

DOS density of states

FCC face-centered cubic

GGA generalized gradient approximation

HTC high-throughput computations

LDA local density approximation

LO longitudinal optic

MD molecular dynamics

PBE Perdew, Burke and Ernzerhof

PBEsol Perdew, Burke and Ernzerhof revisited for solids

RTA relaxation time approximation

TDEP temperature dependent effective potential

TO transverse optic

VCA virtual crystal approximation

VASP Vienna *Ab initio* Simulation Package

ZR zone refining

Chapter 1

Introduction

1.1 Motivation

The demand for energy is increasing as more countries worldwide prosper. Simultaneously, the pollution of the environment from the extraction and use of the energy continues, and the challenges arising from global warming increase in prevalence and severity. To meet the energy demand in a sustainable way, a transition from fossil to renewable energy sources is required. In addition, more efficient utilization of the energy may reduce the emission of greenhouse gasses significantly. The industrial sector contributes to 21% of the global greenhouse gas emissions[1]. However, in the US, between 20% and 50% of the energy consumed by the industry is reported to be wasted as heat[2]. Consequently, there is a call for efficient waste heat recovery systems.

Thermoelectric devices are promising for waste heat recovery applications due to their ability to convert heat directly to electricity. As opposed to traditional waste heat recovery systems utilizing, for example, the Kalina cycle[3], the thermoelectric devices are not based on mechanically moving parts, and are therefore less space consuming and associated with higher stability and reliability. On the other hand, the typical energy conversion efficiency of thermoelectric devices is less than 15%[4], [5]. In some niche markets, such as in space applications, where the access to heat is unlimited or the cost is unimportant compared to the space consume and stability of the device, thermoelectric devices are utilized. However, for general commercial purposes, the conversion efficiency is too low to be competitive with traditional waste heat recovery systems.

There are two factors that reduce the conversion efficiency of the thermoelectric devices. Firstly, the design of the device introduces energy losses at junctions between different constituents. Secondly, the thermoelectric materials are in themselves limiting the conversion efficiency. As a result, improvements of this technology may be achieved through better device designs, or through improved material performance. Even though there are methods that improves the performance of the current thermoelectric materials, such as nanostructuring, many of the state-of-the-art materials are associated with rare, expensive, toxic or environmentally harmful elements[6]. Consequently, thermoelectric materials that outperform the state-of-the-art thermoelectrica, but at the same time are inexpensive, abundant, nontoxic and less harmful to the environment, are needed.

The half-Heusler materials have attracted attention for their potential as thermoelectric materials that may comprise non-toxic, more abundant and less expensive elements[6], [7]. Moreover, they are narrow band gap semiconductors with better electrical properties than many of the best thermoelectric materials[8]. However, they are associated with high thermal conductivity which reduces the energy conversion efficiency. Since the thermal conductivity of half-Heuslers largely is dominated by the lattice thermal conductivity[9], efforts are made to reduce the lattice thermal conductivity. Thus, the good electrical properties of the half-Heuslers are maintained while the thermal conductivity is reduced, resulting in an increased conversion efficiency. Although several half-Heuslers meet the requirements of the new generation of thermoelectric materials, only a few are well studied. Therefore, this thesis aims on exploring new possible thermoelectrica within the half-Heusler segment

1.2 Previous work

This thesis is a continuation of the specialization project performed in the fall of 2016 by the author where the phonon dispersion relations and lattice thermal conductivity of three pure half-Heuslers, XNiBi with X=(Sc, Y or La), was investigated using density functional theory (DFT) calculations in combination with the temperature dependent effective potential (TDEP) method. The lattice thermal conductivity was calculated to 12.3 W/mK, 8.9 W/mK and 5.8 W/mK for ScNiBi, YNiBi and LaNiBi, respectively. The decrease in the thermal conductivity from ScNiBi to LaNiBi was found to be caused by the decreasing acoustic-optic phonon band gap from ScNiBi to LaNiBi. This caused an increase in the anharmonic scattering of the acoustic phonons in LaNiBi compared to ScNiBi, resulting in the decrease in the lattice thermal conductivity. A summary of the specialization project may be found in Appendix A.

1.3 Aim of the thesis

The objective of this thesis is to extend the study on the thermal properties of the XNiBi, X=(Sc, Y or La), half-Heuslers to include scattering mechanisms beyond anharmonic scattering. The impact of mass disorder, both on the X- and the Bi-position of XNiBi, X=(Sc, Y or La), will be studied. In addition, the effect of nanostructuring of the half-Heuslers will be investigated. An understanding of how the different mechanisms influence the thermal properties of the materials is sought through finite temperature *ab initio* simulations using DFT and the TDEP method. Moreover, the simulation methods utilized in this thesis provide an unique opportunity to control different parameters, and, thus, enable further investigations into the mechanisms governing the thermal properties.

Chapter 2

Background

This chapter is intended to give an introduction to the key concepts governing the performance of a thermoelectric material. Moreover, it provides the reader with an insight into the structure of the materials under investigation, and the impact of the structure on the thermoelectric performance. In the last part of the chapter, special attention will be given to the properties that determine the heat conduction of the materials.

2.1 Thermoelectricity

2.1.1 Thermoelectric effect

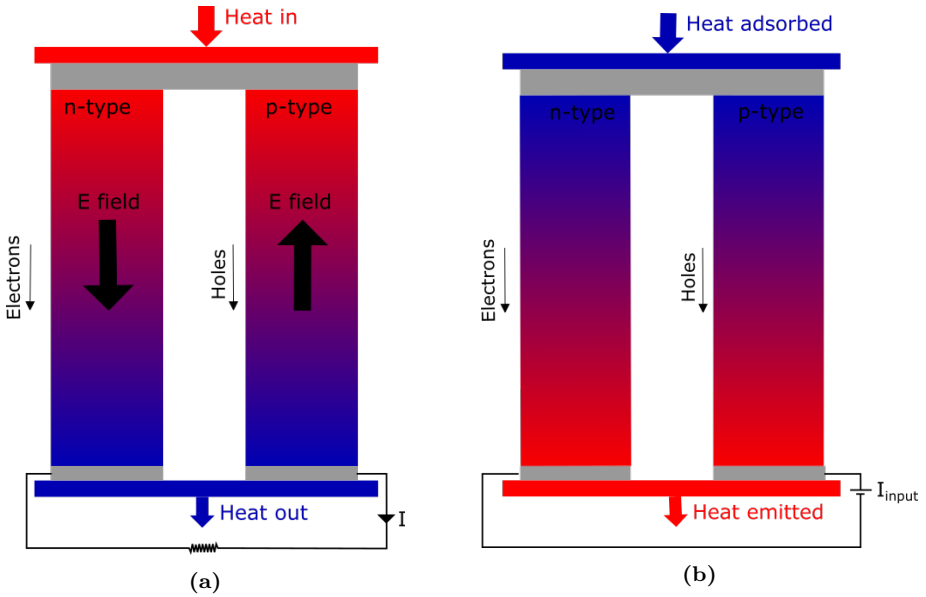

Figure 2.1: Illustrations of a) the Seebeck effect and b) the Peltier effect

The thermoelectric effect describes two phenomena: the Seebeck effect and the Peltier effect. The Seebeck effect involves direct conversion of a temperature gradient to an electrical current as illustrated in figure 2.1a. Oppositely, the Peltier effect, shown in figure 2.1b, converts a voltage difference directly to a temperature gradient.

2.1.2 Seebeck effect

The Seebeck effect was first discovered in 1821 by T. J. Seebeck[10]. As a temperature gradient is imposed across the material, the charge carriers on the hot side are excited to higher energy states. Thus, an imbalance in the occupation of the density of states with higher energy at the hot compared to the cold side is created. This cause the charge carriers to diffuse from the hot to the cold side of the material. The diffusion of charge carriers creates an electric field opposing the temperature gradient. When the diffusion caused by the electric field equals the thermal diffusion, the equilibrium state is reached. The equilibrium voltage difference is proportional to the temperature difference:

$$\alpha = -\frac{\Delta V}{\Delta T} \tag{2.1}$$

where α is the Seebeck coefficient, V is the voltage and T is the temperature.

The Seebeck coefficient is a material dependent parameter. The sign and magnitude of the Seebeck coefficient is related to an asymmetry of the electron distribution around the Fermi level. In metals, the asymmetry is small because the conduction of electrons in one direction implies conduction of holes in the opposite. Thus, the Seebeck voltage is cancelled out resulting in a small Seebeck coefficient. In semiconductors, however, the conduction is either dominated by p- or n-type carriers. Hence, the electron density around the Fermi level is asymmetric, and the Seebeck coefficient larger.

2.1.3 Peltier effect

In 1834, the French physicist J. C. A. Peltier found that the "opposite Seebeck effect" takes place if a voltage difference is applied across thermoelectric materials; then a temperature gradient is created. Unlike Joule heating, the Peltier effect does not involve resistive heating, but transfer of heat carried by the major charge carriers. The heat flow per unit time is given by:

$$\dot{Q} = \Pi I \tag{2.2}$$

where Π is the Peltier coefficient and I is the current.

Since the charge carriers inherently transfer heat, the Seebeck and Peltier effects are coupled through the Thompson relation[11]:

$$\Pi = \alpha T \tag{2.3}$$

2.1.4 Thermoelectric figure of merit

The dimensionless figure of merit, zT, is often used to describe the performance of a thermoelectric material. The figure of merit depends on the material's properties, and is a function of the Seebeck coefficient, α, the electrical conductivity, σ, the thermal conductivity, κ and the temperature, T, as follows:

$$zT = \frac{\alpha^2 \sigma}{\kappa} T \tag{2.4}$$

There are two independent contributions to the thermal conductivity, κ: $\kappa = \kappa_c + \kappa_l$, where κ_c is the charge carrier thermal conductivity, and κ_l is the lattice thermal conductivity. κ_c is coupled to the electrical conductivity, σ, through the Wiedemann-Franz law[11]:

$$\kappa_c = \sigma L T \tag{2.5}$$

where L is the Lorentz number and T the temperature. In metals, where σ and thus κ_c is large, κ_c dominates the thermal conductivity. Although equation 2.4 shows that a high σ is desired, the corresponding high κ_c, and κ, of metals neutralizes the temperature gradient that drives the generation of the current in the thermoelectric materials. In addition, the Seebeck coefficient is inversely related to the charge carrier concentration as shown in figure 2.2, and low for metals as discussed in section 2.1.2. Consequently, metals are poor thermoelectric materials.

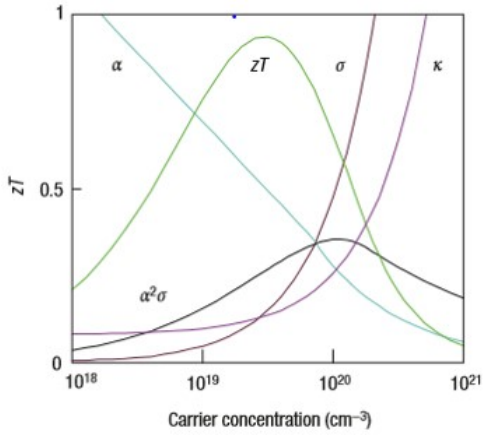

Figure 2.2: The figure of merit, zT, Seebeck coefficient, α, and the electrical and thermal conductivity, σ and κ, as a function of the charge carrier concentration. Figure from Snyder et al.[12]

Figure 2.2 shows that the optimum figure of merit is achieved for charge carrier concentrations associated with narrow band gap semiconductors. Since the electrical conductivity is lower, κ_c is reduced while the Seebeck coefficient is increased. Thus, the semiconductors are better suited for thermoelectric applications than metals. Moreover, κ is determined by both κ_c and κ_l. Since the two contributions are independent of each other, there are ways to further reduce the lattice thermal conductivity, and thus the total thermal conductivity, without changing the electrical properties of the semiconductor.

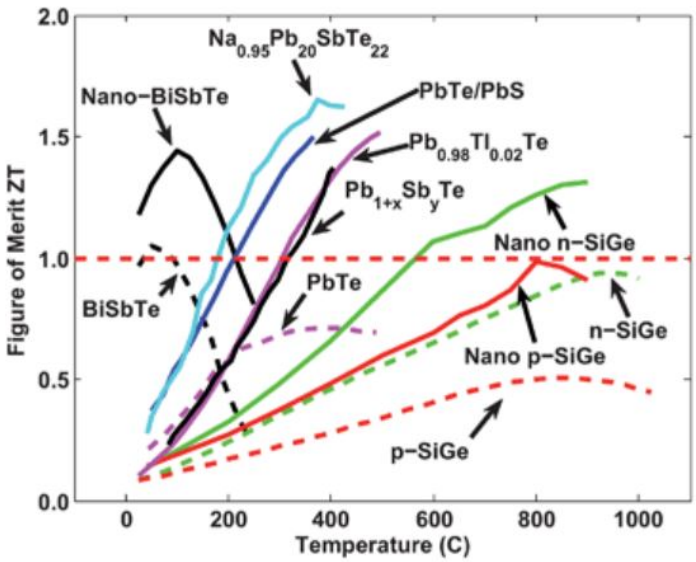

Figure 2.3: The figure of merit as a function of temperature for state-of-the-art thermoelectric materials. The dashed lines show the maximum zT values of the bulk materials while the solid lines show the zT values of modified materials for example by bulk nanostructuring. From Minnich et. al[13]

The figure of merit is a quantitative measure of the thermoelectric performance, and is therefore convenient to use when multiple thermoelectric materials are compared. However, it may give a false image of the applicability of the material. For up-scaled industrial purposes, factors relating to the expense and complexity of the material synthesis route, and the stability, durability, toxicity and environmental impact of the material are also important. In figure 2.3, the figure of merit as a function of temperature for the state-of-the-art thermoelectric materials is shown. Although values of zT up to 2 is achieved, many of the materials are associated with high toxicity and environmental impact, and low material availability resulting in high cost. Some examples of this are the bismuth and lead tellurides. Consequently, there is a call for thermoelectric materials that are mechanically and thermally stable, inexpensive and non-toxic, while the thermoelectric performance remains competitive with the current state-of-the-art thermoelectrica. One of the promising alternatives is the thermoelectric half-Heuslers.

2.2 Half-Heusler materials

2.2.1 Crystal structure

The arrangement of the atoms in a periodically ordered material is described by the crystal structure. The smallest collection of atoms that is repeated throughout the material, constitutes the unit cell. The unit cell is described by lattice vectors. The vector between any two points in the lattice may be described by a linear combination of the lattice vectors, $\mathbf{r} = a\mathbf{a_1} + b\mathbf{a_2} + c\mathbf{a_3}$ where a, b and c are integers and $\mathbf{a_1}$, $\mathbf{a_2}$ $\mathbf{a_3}$ are the lattice vectors for the lattice.

The half-Heusler materials crystallizes in a cubic crystal structure with space group number 216. The space group number corresponds to F$\bar{4}$3m in the Hermann-Mauguin notation.This structure comprises three joined fcc latices of three different elements, X, Y and Z. The structure may also be illustrated as combination of the rock-salt, XY, and the zinc blend, YZ, structure as shown in figure 2.4.

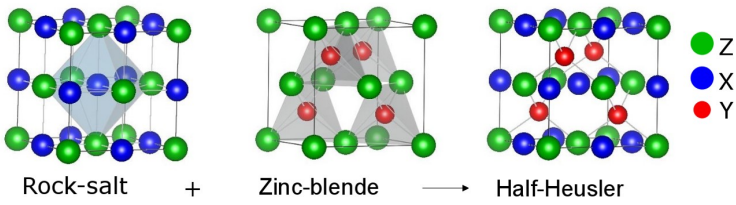

Figure 2.4: Illustration of the half-Heusler crystal structure F$\bar{4}$3m with space group number 216

In the half-Heusler structure, the primitive cell (or unit cell) consists only of three atoms, one of each element, as illustrated in figure 2.5. In the primitive cell, the lattice vectors are not orthogonal, but 60 degrees on each other. Table 2.1 shows the lattice vectors and the atomic positions relative to the Cartesian coordinates.

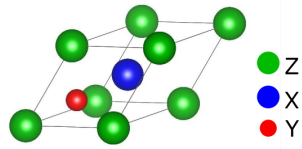

Figure 2.5: The primitive cell of the half-Heusler structure

Table 2.1: The coordinates of the primitive lattice vectors and atom positions relative to Cartesian coordinates. a is the lattice parameter of the cubic half-Heusler structure (F$\bar{4}$3m)

	Cartesian coordinates				Cartesian coordinates		
Lattice vector	x	y	z	Atom	x	y	z
a	0	$\frac{a}{2}$	$\frac{a}{2}$	X	0	0	0
b	$\frac{a}{2}$	0	$\frac{a}{2}$	Y	$\frac{1}{4}$	$\frac{1}{4}$	$\frac{1}{4}$
c	$\frac{a}{2}$	$\frac{a}{2}$	0	Z	$\frac{1}{2}$	$\frac{1}{2}$	0

While the half-Heusler structure loses some symmetry compared to the fcc structure of a single element, it is highly symmetric compared to most other thermoelectric materials. Furthermore, the atomic packing factor remains close to that of the (close-packed) fcc structure. These characteristics with the half-Heusler structure has implications for the material's properties as discussed in the next section.

2.2.2 Material properties

The half-Heusler structure may comprise many different combinations of elements. This flexibility is visualized in figure 2.6 where the colour coding of the elements corresponds to the position of the atoms in figure 2.5. Many of these elements meet the requirements of non-toxicity, abundance, and mechanical and thermal stability[6], [7]. In addition, the half-Heuslers that comprise 18 valence electrons, are often narrow band gap semiconductors. Consequently, they have high electrical conductivity and high Seebeck coefficients[14].

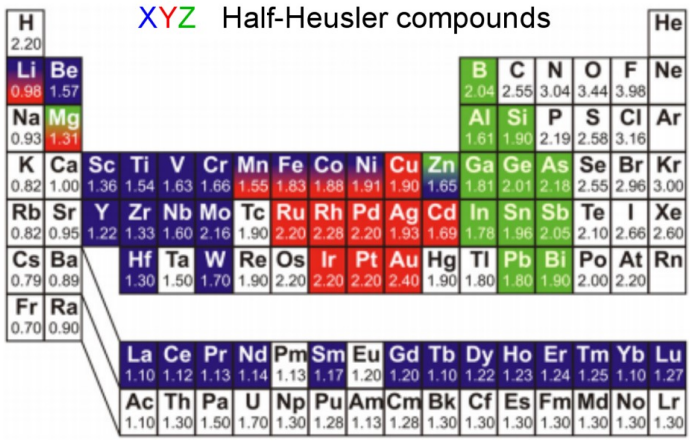

Figure 2.6: The periodic table of elements illustrating the possible elements that may comprise a half-Heusler structure. The colour coding corresponds to the atomic positions of the half-Heusler shown in figure 2.5. Adapted from Graf et al.[14]

On the other hand, the high symmetry and close packing of the half-Heusler crystal structure generally results in high thermal conductivity. Several half-Heusler materials have thermal conductivity above 10 W/mK. This is almost five times the thermal conductivity of commercial bismuth telluride[15], which crystallizes as a trigonal crystal with lower symmetry than the half-Heusler structure. Despite the good electrical properties of the half-Heuslers, the high thermal conductivity reduces the figure of merit from equation 2.4 to the degree that the thermoelectric performance of the half-Heuslers is not competitive with the bismuth tellurides.

Still, the thermal conductivity of many half-Heuslers is dominated by the lattice contribution[9]. It may therefore be reduced without affecting the electrical properties of the materials. One common approach to reduce the lattice thermal conductivity is to dope the material with one or more specific element. This approach has been successfully performed on the XNiSn (X = Ti, Zr, Hf) half-Heusler system where the lattice thermal conductivity has been reduced by 45% at Hf-doping of TiNiSn to $Ti_0.8Hf_0.2NiSn$[9]. Although some experimental studies indicate that this doping results in phase-mixed materials, the reduction in thermal conductivity has also been reproduced in computational studies by isoelectronic substitution of the X-position of TiNiSn. This thesis will therefore explore the effect of isoelectronic substitution on the lattice thermal conductivity.

2.2.3 XNiBi, X=(Sc, Y or La), based half-Heuslers

Despite the amount of possible half-Heusler materials, only a few, such as the XNiSn (X = Ti, Zr, Hf), is well studied. This study is a continuation of earlier work (see Appendix A), where the lattice thermal conductivity of three half-Heuslers, XNiBi (X = Sc, Y, La), was computed using atomistic simulation methods. The three half-Heuslers were chosen based on a list of 75 thermodynaically stable structures developed by Carrete and co-workers[7], and the requirements of lower material costs, higher abundance and lower toxicity compared to the existing thermoelectric materials. While the contribution from anharmonic scattering was investigated in the specialization project, the goal of the present work is to extend the investigation of the XNiBi, X=(Sc, Y or La), based half-Heuslers to include additional scattering mechanisms. Consequently, the effect of the chemical composition of the half-Heuslers on the lattice thermal conductivity is investigated through isoelectronic substitution. Moreover, the effect of nanostructuring is explored.

2.3 Lattice dynamics

In this project, the mechanisms of heat conduction in XNiBi, X=(Sc, Y or La), based materials are studied. Heat is conducted through materials by means of collective atomic motions, or lattice vibrations. Mathematically, these lattice vibrations can be described in terms of phonons. Phonons are wave packages that propagate through the material with a certain velocity given by the frequency and direction of propagation, and they can be described both by classical and quantum mechanical theory. In the classical theory, the harmonic approximation is utilized. While the phonon dispersion relation can be described this way, anharmonicity is not included in the theory. Thus, properties requiring a finite phonon life time, such as the thermal conductivity, must be accounted for using the quantum mechanical approach. This chapter therefore starts out with an introduction to the classical approach before describing the quantum mechanical theory underlying the thermal conductivity.

2.3.1 Potential energy and force constants

In section 2.2.1 the crystal structure was defined as a repetitive pattern with the primitive cell being the smallest repeated unit. Each atom in a crystal structure has a designated position, the equilibrium position. At 0K the atoms are resting in their equilibrium positions. However, as the temperature is increased, and thermal energy added to the system, the atoms start to deviate from their equilibrium positions with a distance $\boldsymbol{u}$. $\boldsymbol{u}$ is called the displacement, and contributes to the potential energy of the system. The contribution from the displacements can be quantified by Taylor expanding the potential energy as follows;

$$U = U_0 + \frac{1}{2}\sum_{ij}\sum_{\alpha\beta}\Phi_{ij}^{\alpha\beta}u_i^\alpha u_j^\beta + \frac{1}{3!}\sum_{ijk}\sum_{\alpha\beta\gamma}\Phi_{ijk}^{\alpha\beta\gamma}u_i^\alpha u_j^\beta u_k^\gamma + \cdots \tag{2.6}$$

where U_0 is the potential energy of the lattice at 0K, α, β, γ are indicies for the Cartesian coordinates, u_i^α is the component in the α-direction of the displacement of atom i (in the unit cell), and $\Phi_{ij}^{\alpha\beta} = \frac{\partial^2 U}{\partial u_i^\alpha \partial u_j^\beta}|_{u=0}$ and $\Phi_{ijk}^{\alpha\beta\gamma} = \frac{\partial^3 U}{\partial u_i^\alpha \partial u_j^\beta \partial u_k^\gamma}|_{u=0}$ are the

second and third order force constants, respectively. They describe the force on one atom as other atoms are displaced from their equilibrium positions, as illustrated in figure 2.7. Note that the first order force constant is not included in equation 2.6 because $\Phi_i^\alpha = \frac{\partial U}{\partial u_i^\alpha} = 0$

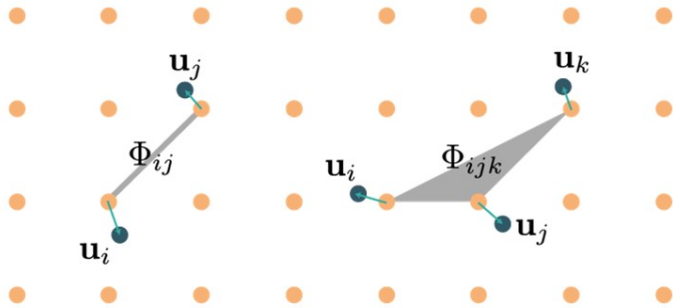

Figure 2.7: Illustration of the second and third order force constants. From N. Shulumba [16]

The force constants determines the interactions between the atoms in the lattice, and can describe the propagation of atomic vibrations. However, for each pair and triplet of atom, there is a second and third order force constant matrix, $\mathbf{\Phi_{ij}}$ and $\mathbf{\Phi_{ijk}}$, each comprising nine and 27 elements, respectively. Consequently, there is, in theory, an infinite amount of force constants. Fortunately, the amount of force constants can be reduced by imposing a set of symmetry operations; Firstly, the periodicity of a crystal lattice allows a shift of all atomic positions by a lattice vector without any changes to the potential energy. Secondly, the derivatives of the potential energy are commutative, and therefore the force constants are symmetric. Thirdly, the force constants are invariant to the symmetry operations belonging to the space group of the lattice. Lastly, translating all atoms in the lattice with an arbitrary displacement, or rotating the lattice with an infinitesimal amount, effectively leaves the lattice, and the potential energy, unchanged.

While the force constants describes the resulting force on one atom as one or multiple other atoms in the lattice are displaced, the concept of phonons describes the lattice vibrations through motion of plane waves. Although the two descriptions are related to one another, the phonons are described in the reciprocal space rather than the real space. Therefore, to understand the concept of phonons, the reciprocal space must be introduced.

2.3.2 Reciprocal space

The conduction of heat through a material involves vibration of planes of atoms in the crystal. While the crystal structure of an ordered material is conveniently described in real space by the unit cell and the atomic coordinates, the reciprocal space is required for a formal mathematical representation of the crystal planes[17].

The reciprocal space describes the orientation of the lattice planes. Therefore, the lattice vectors of the real and reciprocal space are connected through $\mathbf{a}^* = \frac{2\pi}{V_{cell}}\mathbf{b} \times \mathbf{c}$, $\mathbf{b}^* = \frac{2\pi}{V_{cell}}\mathbf{c} \times \mathbf{a}$ and $\mathbf{c}^* = \frac{2\pi}{V_{cell}}\mathbf{a} \times \mathbf{b}$ where $\mathbf{a}$, $\mathbf{b}$ and $\mathbf{c}$ are the real space lattice vectors,

and $\mathbf{a}^*$, $\mathbf{b}^*$ and $\mathbf{c}^*$ are the reciprocal lattice vectors. Similar to the real space lattice, any point in a given reciprocal lattice can be described by the reciprocal lattice vector, $\mathbf{G} = h\mathbf{a}^* + k\mathbf{b}^* + l\mathbf{c}^*$, where h, k, l are integers. Since the dimensions of the reciprocal space are the inverse of length, the vectors describing the wavelength and direction of propagating waves are well defined in reciprocal space:

$$u(\mathbf{r}) = u_0 \, e^{i\mathbf{q}\cdot\mathbf{r}} \tag{2.7}$$

where u_0 is the amplitude, and $\mathbf{q}$ is the reciprocal wave vector. The magnitude of the wave vector is related to the wavelength, λ, of the propagating wave by $|\mathbf{q}| = \frac{2\pi}{\lambda}$ while the direction of the wave vector corresponds the direction of propagation in the real lattice. A consequence of this formalism is that any two vectors whose wave vectors differ by one reciprocal lattice vector have the same effect on the real space lattice point $\mathbf{R} = U\mathbf{a} + V\mathbf{b} + W\mathbf{c}$, as seen in the following;

$$\begin{aligned} \mathbf{q}' &= \mathbf{q} + \mathbf{G} \\ \mathbf{G}\cdot\mathbf{R} &= 2\pi(hU + kV + lW) \\ \mathbf{q}'\cdot\mathbf{R} = \mathbf{k}\cdot\mathbf{R} + \mathbf{G}\cdot\mathbf{R} &= \mathbf{q}\cdot\mathbf{R} + 2\pi(hU + kV + lW) \end{aligned} \tag{2.8}$$

Since hU+kV+LW equals an integer, the waves with wave vector **q** and **q'** are equivalent.

$$u_{q'}(\mathbf{R}) = u_0 \, e^{i\mathbf{q}'\cdot\mathbf{R}} = u_0 \, e^{i(\mathbf{q}\cdot\mathbf{R} + 2\pi(hU+kV+lW))} = u_q(\mathbf{R}) \tag{2.9}$$

Thus, all unique information is found in the space defined by the reciprocal lattice vector, which is called the first Brillouin zone (1BZ).

2.3.3 Harmonic approximation

The wave description of the lattice vibrations is related to the force constants through the vibrational Hamiltonian, $\hat{H}$, and the equations of motion. The vibrational Hamiltonian is an expression of the total energy of the system, and includes the kinetic energy and the potential energy of the vibrating lattice. In the harmonic approximation, the potential energy is truncated after the second order, such that the vibrational Hamiltonian is written as:

$$\hat{H} = U_0 + \sum_i \sum_\alpha \frac{(p_i^\alpha)^2}{2m_i} + \frac{1}{2}\sum_{ij}\sum_{\alpha\beta} \Phi_{ij}^{\alpha\beta} u_i^\alpha u_j^\beta \tag{2.10}$$

where p_i^α is the component of the momentum in the α direction. Using the relations $\dot{u}_i^\alpha = \frac{\partial \hat{H}}{\partial p_i^\alpha} = \frac{p_i^\alpha}{m_i}$ and $\dot{p}_i^\alpha = \frac{\partial \hat{H}}{\partial u_i^\alpha} = -\sum_j \sum_\beta \Phi_{ij}^{\alpha\beta} u_j^\beta$, the equation of motion becomes

$$m_i \ddot{u}_i^\alpha = -\sum_j \sum_\beta \Phi_{ij}^{\alpha\beta} u_j^\beta \tag{2.11}$$

The phonons may also be described as plane waves with wave vector $\boldsymbol{q}$:

$$u_i^\alpha = \frac{1}{m_i} \sum_{\mathbf{q}} A_{\mathbf{q}} e^{i\mathbf{q}\cdot\mathbf{r} - \omega t} \tag{2.12}$$

Thus, inserting equation 2.12 back into equation 2.11 yields an expression relating the frequency of the wave, ω, to the force constants, $\Phi_{ij}^{\alpha\beta}$:

$$m_i \ddot{u}_i^\alpha = \omega^2 u_i^\alpha = -\sum_j \sum_\beta \Phi_{ij}^{\alpha\beta} u_j^\beta \tag{2.13}$$

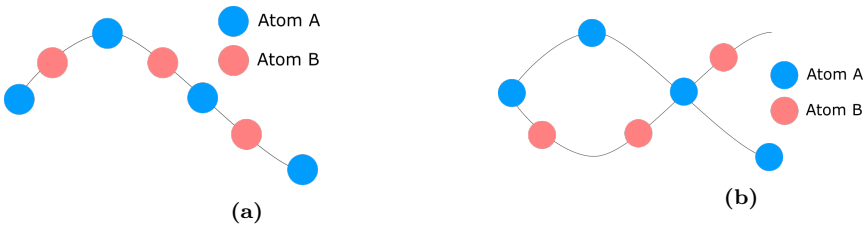

Figure 2.8: Illustrations of a 1D diatomic lattice with a) acoustic phonon mode where the atoms oscillate in-phase, and b) optic phonon mode where the atoms oscillate out-of-phase

In a crystal with N atoms per unit cell, there are 3N solutions to equation 2.13 that all are functions of the wave vector. Therefore, the total solution, $\omega(\mathbf{q})$, which is called the phonon dispersion relation, consists of 3N modes of vibration. Physically, the different modes can be assigned to different patterns of vibration. For example, the atoms can either vibrate in-phase or out-of-phase relative to each other as illustrated for a one-dimensional material comprising two different elements in figure 2.8a and 2.8b. In a three-dimensional crystal, there are always three in-phase, or acoustic, modes, and 3N-3 out-of-phase, or optic, modes. Since the pattern of vibration is different for the acoustic and the optic modes, they are associated with different frequencies. The acoustic and optic modes can be clearly distinguished as the acoustic modes goes to zero at the Brillouin zone center: $\omega \to 0$ as $q \to 0$. Moreover, the motion of the atoms can either be longitudinal (i.e. parallel to the propagation of the phonon) or transverse (i.e. perpendicular to the propagation of the phonon). In some cases, the symmetry of the lattice is broken such that the arrangements of the atoms in the longitudinal and transverse direction are different. As a result, the energies and frequencies associated with the longitudinal and transverse modes are different. This is called longitudinal-transverse splitting. Note that the phonon dispersion relation is positive. Negative values are indicative of instabilities in the crystal structure and therefore a way to control whether the material is thermodynamically stable.

Since all unique information is contained within the 1BZ (as discussed in section 2.3.2), only wave vectors within the 1BZ are accounted for in the phonon dispersion relation. Figure 2.9 shows the dispersion relation of the ScNiBi half-Heusler. There are three atoms in the primitive cell, and therefore nine phonon modes. Three of these are acoustic (showed as red in figure 2.9); one longitudinal and two transverse. The remaining six modes are the longitudinal (in purple) and transverse (in blue) optic modes. Due to different arrangements of the atoms in the transverse and longitudinal directions , the phonon dispersion relation of ScNiBi exhibits longitudinal optic-transverse optic (LO-TO) splitting.

The colouring of the modes in figure 2.9 reflects the amount of heat that each mode carries (i.e. red modes carry most heat and blue least). The amount of heat carried by the mode λ is, amongst others, determined by the group velocity $v_\lambda = \frac{d\omega_\lambda}{dq}$. The group

velocity is in turn related to the lattice thermal conductivity; $\kappa_\lambda \sim v_\lambda$, which will be showed in the following section. As seen in figure 2.9, the slope of the acoustic modes is steeper than that of the optic modes. Consequently, the acoustic modes contribute more to the thermal conductivity than the optic.

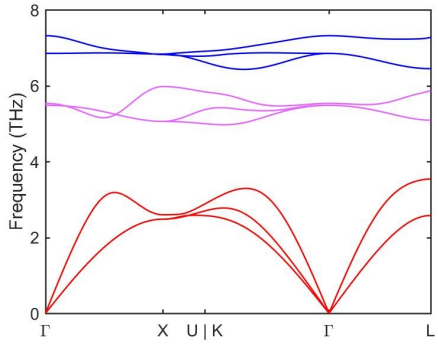

Figure 2.9: The phonon dispersion relation, $\omega(\mathbf{q})$, of the ScNiBi half-Heusler. The acoustic modes are coloured red, the longitudinal optic are purple and the transverse optic are blue

In the harmonic approximation, the potential energy only includes the second order force constants. Thus, the atoms in the lattice are treated as classical springs with spring constant q. The spring constant represents the bond strength between pairs of atoms, and is determined by the atom-atom interaction and the distance between the atoms. While this approximation is convenient to find the phonon dispersion relation, it results in non-interacting phonons. Consequently, the phonons may propagate through the material undisturbed, and properties such as the lattice thermal conductivity becomes infinite. In real materials, however, there are several mechanisms that scatter the phonons and makes the lattice thermal conductivity finite. To account for this anharmonicity, higher order terms must be included in the potential energy, and the phonons must therefore be described by the theory of quantum mechanics rather than by the classical approach.

2.3.4 Lattice thermal conductivity

The lattice thermal conductivity is found by solving the Boltzmann transport equation (BTE) for phonons. The heat current in the α-direction, J_α, arising when a temperature gradient is applied in the same direction, ∇T_α, is determined by the group velocity of the phonon modes λ, and the non-equilibrium distribution function, n_λ:

$$J_\alpha = \frac{1}{V} \sum_\lambda \hbar \omega_\lambda v_{\lambda\alpha} n_{\lambda\alpha} \tag{2.14}$$

where $v_{\lambda\alpha} = \frac{d\omega_\lambda}{dq}$ is the group velocity of the phonon mode λ, and ω_λ is the phonon dispersion relation. The non-equilibrium distribution function describes the number of phonons of the mode λ. Assuming that the thermal gradient is small, the non-equilibrium distribution function can be written as

$$n_{\lambda\alpha} \approx \overline{n}_\lambda - v_{\lambda\alpha} \tau_{\lambda\alpha} \frac{d\overline{n}_\lambda}{dT} \frac{dT}{d\alpha} \tag{2.15}$$

where τ_λ is the relaxation time of the phonon mode λ. Since the equilibrium occupation does not carry any heat, the heat current is given by $J_\alpha = \frac{1}{V}\sum_\lambda \hbar\omega_\lambda v_{\lambda\alpha} v_{\lambda\alpha}\tau_{\lambda\alpha}\frac{d\overline{n}_\lambda}{dT}\frac{dT}{d\alpha}$. Here, the heat capacity can be recognized as $c_\lambda = \hbar\omega_\lambda\frac{d\overline{n}_\lambda}{dT}$. Fourier's law, $J = \kappa\nabla T$, then relates the heat current to the thermal conductivity, κ:

$$\kappa_{\alpha\beta} = \frac{1}{V}\sum_\lambda c_\lambda v_{\alpha\lambda} v_{\beta\lambda}\tau_{\beta\lambda} \tag{2.16}$$

The temperature dependence of the thermal conductivity is determined by the heat capacity, relaxation time and group velocity. At low temperatures, the temperature dependence is dominated by the heat capacity, which is determined by the Debye model[18]. Hence, κ varies as T^3. At high temperatures, however, the lattice vibrations become increasingly anharmonic, meaning that phonon-phonon scattering events to an increasing degree determine the thermal properties of the material. This phenomenon may be implicitly accounted for in the relaxation time, and causes the thermal conductivity to decrease as $\frac{1}{T}$.

2.3.5 Relaxation time

The relaxation time, $\tau_{\alpha\lambda}$, describes the time the phonon mode λ travels in the α-direction before it is scattered, and depends on the mechanism of the scattering. While there are several different scattering events that may occur in a lattice, this report is mainly concerned with phonon-phonon (anharmonic), mass-disorder and grain boundary scattering. In the relaxation time approximation, these scattering events are considered independent of one another, and the total relaxation time, τ_{tot}, may be expressed using Mathiesen's rule:

$$\frac{1}{\tau_{tot}} = \frac{1}{\tau_{anh}} + \frac{1}{\tau_{md}} + \frac{1}{\tau_{gb}} \tag{2.17}$$

where τ_{anh}, τ_{md} and τ_{gb} are the anharmonic, mass-disorder and grain boundary relaxation times, respectively.

Anharmonic scattering

Anharmonic scattering occurs when phonon modes interact with each other. Even though there is no limit to the order of the phonon interactions, the strength of four-phonon interactions is, in general, two or three orders of magnitude weaker than three-phonon interactions[19]. Consequently, only the three-phonon interactions are considered, and the potential energy surfaces in equation 2.6 is truncated after the third order force constant. The three-phonon interactions describe the creation of one phonon from two other phonons, or the creation of two phonons from one. In figure 2.10, an example of the first case is shown. Although the phonons are not particles in the classical sense, they are assigned a momentum, $\hbar\omega$, and must obey both energy and momentum conservation.

$$\begin{aligned} \mathbf{q} + \mathbf{q}' + \mathbf{q}'' &= \mathbf{G} \\ \omega + \omega' + \omega'' &= 0 \end{aligned} \tag{2.18}$$

On the other hand, the momentum is only conserved up to a reciprocal lattice vector, G. In other words, since all unique information is found in the 1BZ, phonon interactions

where the resulting phonons end up outside the 1BZ, are projected back into the 1BZ. This is called Umklapp scattering and is illustrated in figure 2.10b for a three-phonon interaction. Upon projection back to the 1BZ, the direction of the ohonon is reversed or changed. Therefore, Umklapp scattering reduces the thermal conductivity as opposed to normal phonon interaction, illustrated in figure 2.10a.

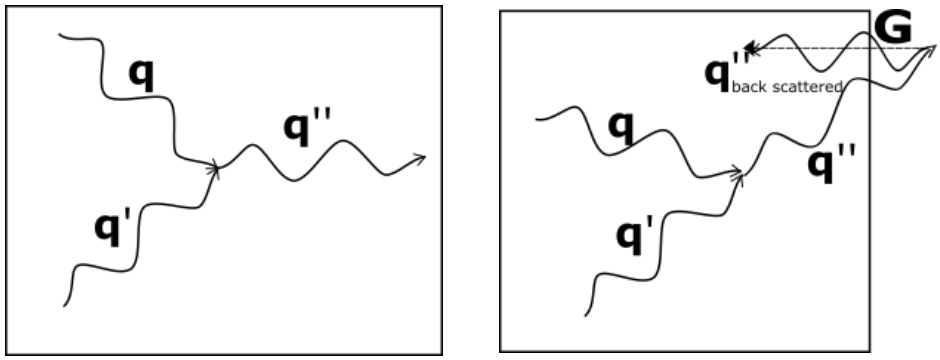

Figure 2.10: Illustration of a) a normal three-phonon interaction, and b) an Umklapp three-phonon interaction. The 1BZ is illustrated by the solid rectangle

Anharmonic relaxation time The anharmonic relaxation time is a complex function of the dispersion relation and the temperature. Considering only the three-phonon interactions, the relaxation time is determined by the third order force constants and the distribution functions of the interacting phonons λ, λ' and λ'' such that $\tau_{anh}^{-1} \sim \sum_{ijk} \sum_{\alpha\beta\gamma} |\Phi_{ijk}^{\alpha\beta\gamma}|^2 \cdot f[n_\lambda, n_{\lambda'}, n_{\lambda''}]$[20]. Here, $f[n_\lambda, n_{\lambda'}, n_{\lambda''}]$ is a functional of the distribution functions which also accounts for the momentum conservation conditions from equation 2.18.

Since optic phonons contribute less to the thermal conductivity than acoustic, anharmonic scattering of the optic phonons does not reduce the thermal conductivity significantly. However, the optic phonons may interact with the acoustic phonons and increase the number of acoustic Umklapp scattering events. The degree of optic-acoustic interaction is determined by the frequency gap between the acoustic and optic phonons given by the phonon dispersion relation (see figure 2.9). Smaller gap yields more optic-acoustic phonon interactions, and thus reduced acoustic phonon relaxation time. In addition, the degree of anharmonicity depends on the temperature. At medium and high temperatures, the phonons may access more phonon modes. Hence, the amount of three-phonon scattering events increases, and the relaxation time decreases.

Mass-disorder

Due to the high symmetry of the half-Heulsler crystal structure discussed in section 2.2.1, the lattice thermal conductivity is generally high. Alloying of the materials introduces random variations in atomic mass and interatomic bond stiffness, and reduces the symmetry of the lattice. The alloying elements disturb the propagation of the phonons and cause scattering as illustrated in figure 2.11. Consequently, the thermal conductivity is reduced.

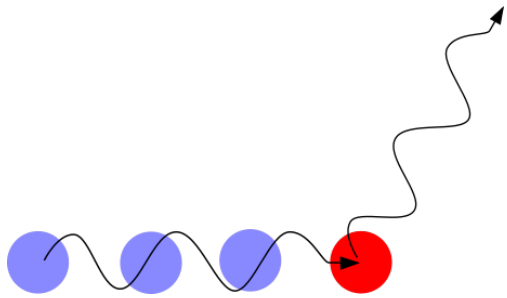

Figure 2.11: Illustration of mass-disorder scattering. The red atom represents the substitute in the 1D material. The substitute constitutes the scattering center.

Mass-disorder relaxation time The degree of disorder introduced in the crystal structure upon alloying, may be described by the mass-disorder parameter, M_{var}, which is given by the deviation of the substituted element from the elemental average of the crystal[19].

$$M_{var}(\mathbf{i}) = \sum_j f_j \left(1 - \frac{m_j(\mathbf{i})}{\overline{m}}\right)^2 \tag{2.19}$$

Here, $m_j(\mathbf{i})$ is the mass of element on the ith position, f_j is fractional concentration of the element on the ith position, and $\overline{m} = \sum_j f_j m_j$ the average mass of the lattice. The mass-disorder relaxation time is then given by the phonon dispersion relation and the mass-disorder parameter as

$$\tau_{md}^{-1} \sim \omega^2 \sum_i M_{var}(\mathbf{i}) \tag{2.20}$$

While anharmonic scattering is highly temperature dependent, mass-disorder scattering is less affected by the temperature. On the other hand, it also scatters the phonons with the lowest frequencies less efficiently[21], [22].

Grain boundary scattering

Real materials are seldom monocrystalline, but are comprised of grains of different sizes and orientations. At the boundaries between the grains, the phonons are scattered due to the changing orientation of the crystal structure. In a way, the lattice symmetry is broken across the boundary, causing the phonons to be scattered as illustrated in figure 2.12. The grain boundary scattering is perhaps the most flexible scattering mechanism considered in this thesis as it targets the phonons with mean free paths comparable to the size of the grains. Thus, the grain sizes may be tuned through material engineering to scatter the phonons carrying the most heat.

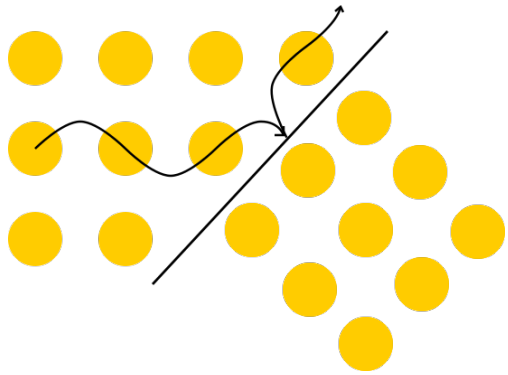

Figure 2.12: Illustration of phonon scattering at a grain boundary, represented by the black diagonal line.

Grain boundary relaxation time Although the description of the grain boundary scattering is complex due to the variety of the boundaries that may exist, the scattering may be estimated by assuming purely diffusive scattering across the boundaries. Then the grain boundary scattering relaxation time is given by[23]:

$$\frac{1}{\tau_{gb}} = \frac{v_\lambda}{L} \tag{2.21}$$

where L is the grain size and v_λ is the group velocity.

Chapter 3

Background for *ab initio* simulations

Ab initio simulations based on density functional theory (DFT) utilize quantum mechanical laws and principles rather than empirical data to model thermodynamical properties of materials. Thus, the methods may be applied to general cases where experimental data is not available. However, DFT is a ground-state theory, and all calculations are therefore performed at 0 K. The most crucial effects of thermal vibrations may be included through the harmonic and quasiharmonic approximations, but the effects of anharmonicity beyond the thermal expansion are still excluded[24]. In the present work, the temperature dependent effective potential (TDEP) method is utilized with DFT calculations to account for the anharmonicity of the system. This chapter therefore introduces the fundamentals and application of the TDEP method. In addition, an introduction to DFT and its application through the Vienna *Ab initio* Simulation Package (VASP), is given.

3.1 Density functional theory

Density functional theory (DFT) is a quantum mechanical modelling method that approximates the 0 K ground state electron density of many-body systems. Thus, materials properties such as the lattice parameter and the electronic band gap may be found. This section gives an overview of the fundamentals of DFT, but is not meant to give a deep understanding of the theory. The reader is referred to the book "Density Functional Theory - A Practical Introduction" [25] for a more thorough introduction to DFT.

3.1.1 Schrödinger Equation

The complete quantum state of a system is described by its wavefunction, ψ, which is found by solving the Schrödinger equation. Although the Schrödinger equation may be solved analytically for simple systems, such as the Hydrogen atom, the equation becomes intractable for more complex many-body systems. In a crystalline solid, for example, the interactions between nuclei and electrons, each individual nucleus and all other nuclei, and each individual electron and all other electrons must be considered.

The equation is simplified using the Born-Oppenheimer approximation, where the motion of the electrons is assumed independent of the motion of the nuclei. The time-independent Scgrödinger equation may then be written as

$$\left[-\frac{\hbar^2}{2m}\sum_{i=1}^{N}\nabla_i^2+\sum_{i=1}^{N}V(\mathbf{r_i})\sum_{i=1}^{N}\sum_{j<i}U(\mathbf{r_i},\mathbf{r_j})\right]\psi=E\psi \tag{3.1}$$

where ψ is the total electron wavefunction and E is the ground state energy. The three terms in the bracket are, from left to right, the kinetic energy of each electron, the interaction energy between each electron and the collection of (fixed) nuclei, and the interaction energy between different electrons. Since the total electron wavefunction is a superposition of the N individual wavefunctions, $\psi=\psi_1(\mathbf{r})\psi_2(\mathbf{r})...\psi_N(\mathbf{r})$, equation 3.1 can be solved for each individual electron. Nevertheless, in a bulk material, the system quickly becomes too complex and large to solve for the electron wavefunctions.

3.1.2 Hohenberg-Kohn theorems

While the many-body Schrödinger equation is too complicated to solve explicitly, it may be solved implicitly by utilizing the Hohenberg-Kohn theorems. The first Hohenberg-Kohn theorem states that *the ground state energy from Schrödinger's equation is a unique functional of the electron density.* In other words, the ground state energy, E, in equation 3.1, is related to the electron density, n($\mathbf{r}$).

$$E=E[n(\mathbf{r})] \tag{3.2}$$

Moreover, the second Hohenberg-Kohn theorem says that *the electron density that minimizes the energy of the overall functional is the true electron density corresponding to the full solution of the Schrödinger equation.* Since the electron density is related to the individual electron wavefunction, ψ_i, with

$$n(\mathbf{r})=2\sum_{i=1}\psi_i^*(\mathbf{r})\psi_i(\mathbf{r}) \tag{3.3}$$

the N dimensional problem is in theory reduced to a "simple" three dimensional optimization problem. Unfortunately, neither the first nor the second theorem reveals the true form of the energy functional. Consequently, the energy functional must be approximated. If equation 3.1 is rewritten for the individual electron wavefunctions,

$$\left[-\frac{\hbar^2}{2m}\nabla^2+V(\mathbf{r})+V_H(\mathbf{r})+V_{XC}(\mathbf{r})\right]\psi_i(\mathbf{r})=\epsilon_i\psi_i(\mathbf{r}) \tag{3.4}$$

the two first terms in the bracket are the same as the two first in equation 3.1 (describing the electron kinetic energy and the interaction energy between electron and the collection of nuclei). While the two first terms are known, the two last comprise the unknown electron-electron interaction. However, the Hartree potential, V_H, describing the the repulsion between the electron in equation 3.4 and the electron density, may be calculated:

$$V_H(\mathbf{r})=e^2\int\frac{n(\mathbf{r'})}{|\mathbf{r}-\mathbf{r'}|}d^3r' \tag{3.5}$$

The Hartree potential includes an electron self-interaction, which is corrected for by the exchange-correlation potential, V_{XC}.

3.1.3 The Exchange-Correlation Functional

The self-interaction of the Hatree potential can be corrected for in several ways. The local density approximation (LDA) takes advantage of the fact that the exchange-correlation potential is precisely known for the uniform electron gas, where the electron density is independent of the position, $\mathbf{r}$. Thus, we assume that for every position, $\mathbf{r}$, the potential is equal to the known potential for constant electron density:

$$V_{XC} = V_{XC}^{electron\ gas}[n(\mathbf{r})] \tag{3.6}$$

Although the LDA is easily applied to many systems, it is not the most accurate approximation. The general gradient approximation (GGA) takes the gradient of the electron density into account. Several variations of the GGA have been developed. In this project, the Perdew-Burke-Ernzerhof revised for solids (PBEsol) functional is utilized. In PBEsol, empirical parameters are accounted for. Thus, the functional may yield higher physical accuracies when properties such as the lattice parameter is calculated[26].

3.1.4 Computational approaches to DFT

The electronic and ionic convergence loop

Since the Hartree potential (equation 3.5) is a function of the electron density, solving the Schrödinger equation using the Hohenberg-Kohn theorems is an iterative process:

1. Guess an initial electron density
2. Calculate the Hartree potential from equation 3.5
3. Calculate the energy from the summed potentials given a specified exchange-correlation functional
4. Solve for the single electron wavefunction in the Kohn-Sham equation (equation 3.4)
5. Using this single electron wavefunction and equation 3.3, find the electron density
6. Use the found electron density as the new "guessed" density and go back to step 1

This loop is called the electronic convergence loop.

Once the minimum energy is reached, and the ground state electron density found, the forces between the ions in the lattice can be calculated. The Hellmann-Feynman force acting on an ion j, is given by:

$$\mathbf{F_j^{H-F}} = -\frac{\delta E}{\delta \mathbf{R_j}} \tag{3.7}$$

where E is the Kohn-Sham energy and $\mathbf{R}_j$ is the position of ion j.

When the equilibrium crystal structure is desired, the Hellmann-Feynman forces are used to move the ions such that the net forces acting on the ions are minimized. For every new configuration of the ions in the lattice, the electronic convergence loop must be performed.

Energy cutoff and k-point density

In crystalline solids, the single electron wavefunction from equation 3.4 is expressed as a plane wave with the periodicity of the crystal lattice.

$$\psi_{\mathbf{q}(r)} = \sum_{G} c_{\mathbf{q}+\mathbf{G}} e^{i(\mathbf{q}+\mathbf{G})\mathbf{r}} \tag{3.8}$$

where $\mathbf{q}$ is the wave vector, $\mathbf{G}$ is a reciprocal lattice vector and $\mathbf{r}$ is the position of the ion in the unit cell.

Hence, to find the wavefunction for each $\mathbf{q}$, the summation in equation 3.8 must run over infinitely many $\mathbf{G}$ vectors. This would be computationally very costly. To limit the summation, the total energy of the wavefunction is considered:

$$E = \frac{\hbar^2}{2m}|\mathbf{k}+\mathbf{G}|^2 \tag{3.9}$$

From thermodynamics, we know that the system seeks to minimize its energy. Therefore, the lower energy states are more important than the higher. Thus, only the $\mathbf{G}$ vectors up to a set maximum, $\mathbf{G}_{cut}$, are considered. Then the cutoff energy is given by: $E_{cut} = \frac{\hbar^2}{2m}G_{cut}^2$. The appropriate cutoff energy, E_{cut}, is found for each unique system, and is determined by the convergence of the system with respect to the cutoff energy. Higher E_{cut} yields better convergence, but requires more computational power.

Another numerical simplification is to discretize the 1BZ to avoid continuous integration over all possible wave vectors within the 1BZ. The integration space is replaced by discrete mesh, and the density of the mesh points determines the accuracy of the calculations. Higher k-point density yields more accurate calculations, but are also more computationally costly. The minimum density for which the system converges is therefore chosen as the k-point density used in the calculations on that system.

Pseudopotentionals

The computational cost of the DFT calculations may be further reduced freezing the core electrons and the nucleus, and replacing them with a constant potential that matches various physical properties[25]. This is called the pseudopotential. The pseudopotential is given for isolated atoms, but there may be several variations for one single element depending on the number of valence electrons. While potentials with many valence electrons, so-called hard potentials, can be more accurate, they require higher cutoff energies. Thus, they are more computationally exhausting, and not appropriate for all calculations. The soft potentials, on the other hand, have fewer valence electrons and require lower cutoff energies, but at the expense of the accuracy of the calculations.

3.1.5 Accuracy and limitations of DFT calculations

The accuracy of the DFT calculations is affected in two ways. The numerical accuracy describes the deviation of the calculated results from the true mathematical results, and is determined by the convergence of the calculations. Consequently, the energy cutoff, k-point density and pseudopotentials control the numerical accuracy. On the other hand, completely converged calculations does not necessarily provide physically accurate results. This is a consequence of the approximated exchange-correlation

functional, which may yield inaccurate Hellmann-Feynmann forces (equation 3.7), and reduce the physical accuracy of the calculations. Since the distance between the atoms in a lattice affects the phonons of that lattice (as discussed in section 2.3.3), it is important to achieve physically accurate lattice constants in this project. Therefore, the PBEsol functional is utilized.

3.1.6 Vienna *Ab initio* Simulation Package

The Vienna *Ab initio* Simulation Package (VASP) is a computer simulation program that uses DFT for atomic scale materials modelling. In the following, a brief introduction to the basic input files of VASP is given. More details about the input parameters may, however, be found in Appendix B. In addition, the reader is referred to the articles by Kresse and coworkers[27]–[30] for a better understanding of the theoretical background of the simulation package. A practical introduction to VASP may also be found in the VASP manual[31].

Input files

The four most basic and important input files in VASP are the INCAR, POSCAR, POTCAR and KPOINTS files. All VASP calculations require (at least) these files to perform the DFT calculations. While the files are described briefly in the following, no specific examples are given. The reader is referred to B for examples of POSCAR, KPOINTS and INCAR files.

INCAR The INCAR file defines what we want VASP to calculate. In addition, it describes how the calculations are performed. In the following, the most important INCAR tags/parameters for the calculations performed in the present work are described.

POSCAR The POSCAR file gives information on the unit cell or supercell, i.e. the position of each atom as well as the length and direction of the lattice vectors. A supercell is an assembly of several unit cells, and is used in calculations where a larger structure is required to obtain the desired accuracy.

POTCAR The POTCAR file defines the pseudopotentials to be used for each different atom in the system.

KPOINTS The KPOINT file defines the k-point density for the calculations. The density is given as a number of k-points to be used in each direction. For the face-centred cubic lattice, the k-mesh is given as a×a×a, where a is the number of k-points on the mesh in the a lattice direction.

Output files

There are a number of output files from VASP. In this project, however, the following files are the most important:

OUTCAR The OUTCAR file is the most important output file in VASP. It contains all the information from the performed calculation including total energies, forces, pressures in the lattice and band gaps.

CONTCAR The CONTCAR file has valid POSCAR format, and is written after every ionic step. it can therefore be used for "continuing" jobs. For *ab initio* molecular dynamics (discussed in section 3.2), the CONTCAR contains the actual coordinates and velocities of the atoms in the supercell.

3.2 *Ab initio* molecular dynamics

Despite the fact that the system is assumed to be in its ground state (i.e. at 0 K) in DFT calculations, *ab initio* molecular dynamics (AIMD) provides a way to simulate real time evolution of the system at *finite* temperatures using DFT[16]. In the Born-Oppenheimer approximation the motion of the electrons and the nuclei is considered independent of one another (as discussed in section 3.1.1) because the nuclei move slower than the electrons. Thus, the nuclei may be considered as classical particles that obey the Newtonian mechanics, $\dot{r}_i = \frac{p_i}{m_i}$ and $\dot{p}_i = f_i$, where $\mathbf{r}_i$ is the position of, $\mathbf{p}_i$ is the momentum of, m_i is the mass of and $\mathbf{f}_i$ is the force action on atom i in lattice with n atoms. The forces acting on the atoms at a given time are calculated using DFT as described in the previous section. These forces are related to the velocity and position of the atoms at the next time step, δt, through numerical integration of the equations of motion. The integration is performed using a Verlet algorithm where the position is expanded around t[31];

$$r_i(t + \delta t) = r_i(t) + \dot{r}_i(t)\delta t + \ddot{r}_i(t)\delta t^2 \tag{3.10}$$

In addition, the average velocity of the atoms in the lattice is controlled by the temperature in the canonical ensemble:

$$\begin{aligned} \frac{1}{2} m \overline{(\dot{r}^2)} &= \frac{k_B T}{2} \\ \Rightarrow \frac{1}{2} \sum_{i=1}^{3n} m_i \dot{r}_i^2 &= \frac{k_B T}{2} \end{aligned} \tag{3.11}$$

Consequently, the velocity and position of the atoms at time, t, are controlled by the set temperature, T, and the forces calculated using DFT.

Since the starting point of AIMD calculations is the lattice with all atoms in their equilibrium position, an initial displacement of the atoms is required to perform the numerical integration. Practically, this is done by assigning an initial velocity to each individual atom such that the equilibration time is minimized.

AIMD is an integral part of VASP, and specifications about how to run AIMD calculations in VASP is found in Appendix B.2.

3.3 Temperature dependent effective potential method

The temperature dependent effective potential (TDEP) method is a set of algorithms and methods for finite temperature lattice dynamics. TDEP runs with VASP or any

other software providing atomic displacement and force data. This could be DFT-based software or software running molecular dynamics using empirical force fields. The TDEP method accounts for anharmonic effects (beyond the thermal expansion) by including terms beyond the second order in the Taylor expansion of equation 2.6. Thus, finite temperature properties may be calculated directly.

In this project, the TDEP method is utilized with VASP to calculate the dispersion relations and thermal conductivity of the half-Heusler alloys. The following section is mostly based on the journal articles by Olle Hellman and coworkers[32]–[34], and may be reviewed if a more thorough understanding of the TDEP method is desired. In addition, the TDEP website[23] gives a practical overview of the background and features of the TDEP method.

3.3.1 *Ab initio* molecular dynamics

In the TDEP method, the effects of finite temperatures are included in the forces acting on the lattice through the AIMD described in section 3.2. The AIMD is performed in the canonical ensemble[34]. Thus, the lattice is allowed to vibrate according to the set temperature as described in equation 3.11. The forces acting on the atoms in the lattice at a time given time, and thus at given atomic displacements, are calculated using DFT. During one AIMD run, N_{tdep} pairs of forces, F_i^t, and displacements, u_i^t, for the atom in position i are sampled with time spacing $t_{step} = \frac{t_{tot}}{N_{tdep}}$. The collection of forces acting on the lattice at the time, t, $\mathbf{F^t_{DFT}}$ is considered the "true" forces, and includes both harmonic and anharmonic contributions.

3.3.2 Model Hamiltonian

Although the forces calculated using DFT include anharmonicity, the force constants are required to access the finite temperature properties (as discussed in the previous chapter). A model Hamiltonian expanded to the third order force constant is therefore created.

$$\hat{H}_{model} = U_0 + \sum_i \sum_\alpha \frac{(p_i^\alpha)^2}{2m_i} + \frac{1}{2}\sum_{ij}\sum_{\alpha\beta} \tilde{\Phi}_{ij}^{\alpha\beta} u_i^\alpha u_j^\beta + \frac{1}{3!}\sum_{ijk}\sum_{\alpha\beta\gamma} \tilde{\Phi}_{ijk}^{\alpha\beta\gamma} u_i^\alpha u_j^\beta u_k^\gamma \quad (3.12)$$

where $\tilde{\Phi}_{ij}^{\alpha\beta}$ and $\tilde{\Phi}_{ijk}^{\alpha\beta\gamma}$ are the symmetry irreducible model force constants, and u_i^α is the actual displacement from the AIMD in section 3.3.1. The (model) forces acting on the lattice is then given as

$$\tilde{F_i^\alpha} = \sum_j \sum_\beta \tilde{\Phi}_{ij}^{\alpha\beta} u_j^\beta + \frac{1}{2}\sum_{jk}\sum_{\beta\gamma} \tilde{\Phi}_{ijk}^{\alpha\beta\gamma} u_j^\beta u_k^\gamma \quad (3.13)$$

The model forces, $\tilde{\mathbf{F}}$ can now be compared to the "true" forces at each time step, $\mathbf{F^t_{DFT}}$, and the model force constants updated such that the difference between the "true" and the model forces is minimized:

$$\min_\Phi \Delta\mathbf{F} = \frac{1}{N_{tdep}} \sum_{t=1}^{N_{tdep}} |\mathbf{F^t_{DFT}} - \tilde{\mathbf{F}}^\mathbf{t}|^2 \quad (3.14)$$

As opposed to the force constants defined in equation 2.6, the model force constants may be interpreted more as polynomial fitting parameters than derivatives of the

potential. Therefore they implicitly include all orders of anharmonicity, which are explicitly present in the "true" forces from the AIMD. The second and third order (model) force constants can now be used to calculate the harmonic and anharmonic properties such as the phonon dispersion relation and lattice thermal conductivity as described in section 2.3.3 and 2.3.4.

3.3.3 Computational cost

Even though the AIMD provides a route to directly extract the anharmonic properties of the material, a large number of time steps is required for the force constants to converge. Performing DFT force calculations with the required accuracy therefore becomes a costly and time consuming procedure. The TDEP method solves this problem by performing low precision AIMD force calculations yielding low accuracy force constants. These force constants are then utilized together with a Monte Carlos routine to generate n structures with different displacements (in accordance with the force constants). Here, $n << N_{tdep}$, but still span the time space such that the displacements of the different structures are independent of one another. The "true" forces acting on each structure are calculated with high accuracy using DFT, and high accuracy force constants are found using the same procedure as described in section 3.3.2.

Size of the supercell

The AIMD described in section 3.2 is a real space method. Since the wavelengths of the phonons may be larger than the size of the unit cell, the AIMD may have to be performed on supercells comprising several unit cells[16]. Since the cost of the DFT calculations scales with the cube of the system size, the convergence of the force constants with respect to the size of the supercell should be tested to avoid extra cost.

3.3.4 Implementation of TDEP

Generally, the TDEP method involves the following steps:

1. Relaxation of the supercell using DFT
2. Performance of an N_{tdep}-step low-accuracy AIMD calculation on the relaxed supercell
3. Extraction of the pairs of forces and displacements from the N_{tdep} steps of the AIMD calculations
4. Calculation of the third and second order force constants
5. Generation of n displaced structures based on the force constants. Here $n << N_{tdep}$
6. Performance of high-accuracy static DFT force calculation on each of the n structures
7. Extraction of the pairs of forces and displacements from the n structures
8. Calculation of the third and second order force constants

9. Calculation of temperature dependent properties such as phonon dispersion relation and lattice thermal conductivity

3.3.5 Simulation of alloys

This thesis aims on simulating the effect of partial substitutions on the X-position of the XNiBi, X=(Sc, Y or La), half-Heuslers. As a substitute is introduced to the lattice, the original symmetry of the lattice is broken, causing mass-disorder scattering of the phonons to occur as discussed in section 2.3.5. Accordingly, the number of symmetry irreducible force constants increases. Thus, computations of the force constants soon become intractable since fewer symmetry operations can be applied to the calculations as described in section 2.3.1. Consequently, methods where the number of symmetry irreducible force constants are reduced, must be utilized to calculate the thermal properties of alloys.

Virtual crystal approximation

In the virtual crystal approximation (VCA), the full symmetry of the original lattice is preserved upon alloying[35]. This is achieved by inserting an averaged element in the position where the substitution occurs. Consider, for example, the $A_{1-x}B_x$ alloy. In the case of real alloying, the A and B elements are randomly distributed on the atomic sites of the lattice such that the total concentration of A is $1-x$ and of B is x. In the virtual crystal, on the other hand, a "new" element $C = (1-x)A + xB$ is created and placed on all atomic sites. Consequently, the potential of the virtual crystal consists of the real-space average of the individual components in the real alloy. This results in a lattice where the full symmetry of the original material is retained, but at the expense of the local environmental features of the real crystal[36]. In alloys where the properties of the individual elements are very different, the local environment may vary throughout the alloy, resulting in a breakdown of the VCA, and the failure of the calculations of the alloy properties[36]–[38].

Special quasirandom structure

Another way to describe an alloy is through a special quasirandom structure (SQS)[39]. In the SQS, the substitutes are introduced in a random fashion resembling the real alloy. Thus, variations in the local environment of the lattice may be accounted for. However, not only the computation of the force constants become challenging, but also the computation of a representative configuration of the alloy from the numerous choices of possible configurations. In many cases, this representative configuration is found by statistically sampling over the possible configurations, and thus finding the most likely structure given the symmetry of the lattice and the elements it comprises. As the number of elements in the lattice increases, it soon becomes computationally infeasible to compute the statistically representative configuration this way. The SQS, however, is based on matching of the correlation function of the alloy with that of the infinite, random structure. Consider again the $A_{1-x}B_x$ alloy. Any given arrangement of A and B may be described by geometric figures $f = (k, m)$ where f has k vertices spanning the mth nearest neighbours as illustrated in figure 3.1. Each site in a figure is assigned with a spin value, $\hat{S}_i$, which is 1 for A- and -1 for B-occupied sites. The

correlation between A- and B-occupied sites of figure f is then given by:

$$\langle \overline{\Pi}_f \rangle = \sum_{\sigma} \overline{\Pi}_f(\sigma)\rho(\sigma) \tag{3.15}$$

where σ is the configuration of the alloy with N sites, $\overline{\Pi}_f(\sigma) = \frac{1}{ND_f}\sum_{\mathbf{l}} \Pi_f(\mathbf{l},\sigma)$ is the lattice average over all locations $\mathbf{l}$ of symmetry related figures f, $\Pi_f(\mathbf{l},\sigma) = \prod \hat{S}_i$ is the product of spin variables for figure f, and D_f is the number of figures per site. $\rho(\sigma)$ is the normalized configurational density matrix[39].

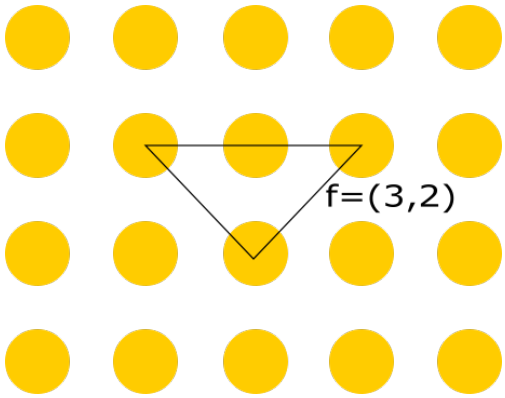

Figure 3.1: Illustration of a figure with three vertices spanning the second nearest neighbours

The correlation functions, $\langle \overline{\Pi}_f \rangle$, of an infinite, random alloy $A_{1-x}B_x$ can be computed explicitly. Thus, a representative configuration of the alloy may be found by comparing the correlation functions of that configuration to those of the infinite, random structure. The configuration for which the difference between the correlation functions of the configuration and the infinite, random alloy is below a set value, is chosen as the random alloy. In the cases where the correlation functions of the infinite, random alloy cannot be computed explicitly, statistical sampling must be performed to find an estimate for the correlations. While this is computationally exhausting, the procedure can be performed only once for a given material. For example, the "infinite, random" correlation functions of the $A_xB_yC_{1-x-y}YZ$ half-Heusler are valid for all combinations of A, B and C, as well as Y and Z. Consequently, computing the random structure becomes much less computationally costly than standard, statistical sampling of the random alloys, which must be performed for every concentration of a specific alloy.

Once a representative alloy for a given concentration of the elements on the position of the substitution is found, the TDEP method utilizes the AIMD of VASP to find pairs of forces and displacements as described in section 3.3.1. Now, to reduce the number of irreducible force constants such that the calculations of the force constants become tractable, the symmetry of the original lattice is reinstated[16]. Consequently, the force constants of randomly alloyed structures may be calculated without an unreasonable computational cost.

Utilization of the SQS with the TDEP method largely follows the same steps as described in section 3.3.4. The AIMD calculation is performed on the SQS, but

with the geometry constraints from the original lattice imposed on the calculation of the force constants. Utilization of the SQS may also impose different supercell size requirements as a certain size also is required to achieve reliable SQS's.

Chapter 4

Computational Approach

In this chapter the calculations performed in the present wok are described. While few VASP simulations were performed here, the calculations are based upon VASP simulations from the specialization project. Therefore, examples of VASP input files and parameters are given in Appendix B. In addition, the procedure used in the calculations utilizing the special quasirandom structure (SQS) are given in this chapter. Even though the calculations were unsuccessful, experience from the calculations performed in this thesis may be helpful in later attempts.

4.1 Implementation of SQS in the TDEP method

The implementation of SQSes in the TDEP method was investigated using 3x3x3 SQSes (i.e. three primitive cells in each lattice direction) of the binary half-Heusler alloy $Sc_xLa_{1-x}NiBi$. Note that while the 3x3x3 supercell gives converged results with respect to the thermal conductivity, figure 4.1 shows that a 4x4x4 supercell is required for converged 4th shell correlations functions of figures (1,1), (1,2) and (2,1). For converged 4th shell correlation functions of figure (2,2) even larger SQSes may be necessary. As the figure (2,2) in the 4th shell defines the correlation between neighbours relatively far from one another, they are, however, generally not required not be fully converged. Despite the convergence test of figure 4.1, 3x3x3 SQSes were explored in this project due to the greatly increased cost of the DFT force calculations of the larger supercells. Thus, calculations on 4x4x4 supercells were not feasible to perform within the schedule of this project.

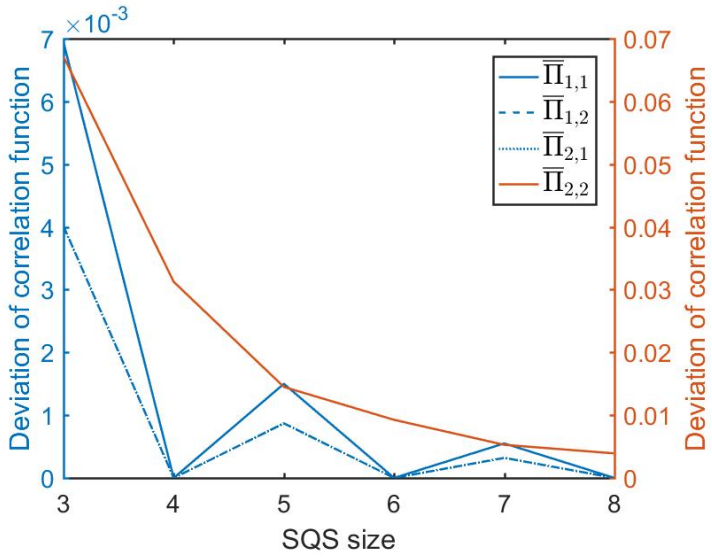

Figure 4.1: Deviation of the fourth shell correlation functions of figure (k,m) from the correlation function of the infinite random half-Heusler alloy. On the primary axis, $\overline{\Pi}_{1,1}$, $\overline{\Pi}_{1,2}$ and $\overline{\Pi}_{2,1}$ are shown, while $\overline{\Pi}_{2,2}$ is shown on the secondary y-axis

The 3x3x3 SQSes were relaxed over three loops with ISIF=2, ISIF=7 and ISIF=2 for the first, second and third loop, respectively (see Addendix B for an explanation of the VASP tag ISIF). The other INCAR tags were kept constant and as described in Appendix B.1.1. *Ab initio* molecular dynamics was performed on the relaxed structures, and the forces and displacements successfully extracted. To reduce the number of irreducible force constants to be calculated, the TDEP method reinstates the symmetry of the underlying lattice as described in section 3.3.5. However, due to a flawed implementation of the symmetry operations imposed on the SQS in the version of the TDEP method available to this project, the force constant calculations yielded nonphysical results. Even though it is possible to correct the mistakes in the method, the corrections were too time consuming to be performed before the conclusion of this project. Consequently, this thesis is unable to present results from calculations utilizing the SQS approach with the TDEP method.

4.2 Thermal properties of $Sc_xY_yLa_{1-x-y}NiBi$

In this part of the project, the thermal properties of the $Sc_xY_yLa_{1-x-y}NiBi$ alloys were investigated using the TDEP method implemented with the virtual crystal approximation (VCA). The following section describes the methods used to calculate the thermal properties considering both anharmonic and mass-disorder scattering. Thereafter, the calculations investigating different contributions to the thermal properties are described.

4.2.1 Lattice thermal conductivity

The calculations of the total thermal properties (i.e. considering both anharmonic and mass-disorder scattering) utilized Vegard's law. Thus, the lattice parameters and force constants of the alloys were found by linearly interpolating the corresponding properties of the parent materials. For example, the lattice parameter of $Sc_{0.25}La_{0.75}NiBi$ would be $a_{Sc_{0.25}La_{0.75}} = 0.25 \cdot a_{ScNiBi} + 0.75 \cdot a_{LaNiBi}$. The validity of Vegard's law was tested for 2x2x2 SQSes of the binary compositions $Sc_xLa_{1-x}NiBi$, $Sc_xY_{1-x}NiBi$ and $Y_xLa_{1-x}NiBi$ as shown in figure 4.2[1]. As the lattice parameters and force constants of the alloys were interpolated from the parent materials, no DFT calculations were required to calculate the thermal properties. In other word, the steps 1-8 in the procedure in section 3.3.4 were omitted, and only the last step was performed. However, the properties of the parent materials were calculated using the steps 1-8 in the specialization project.

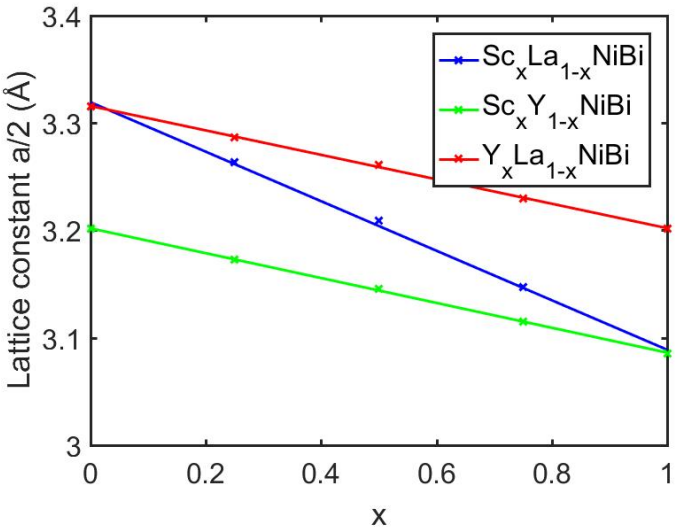

Figure 4.2: Lattice parameter of $Sc_xLa_{1-x}NiBi$ (in blue), $Sc_xY_{1-x}NiBi$ (in green) and $Y_xLa_{1-x}NiBi$ (in red) as a function of the composition x. The crosses represent the calculated values while the solid lines are linear interpolations

The thermal properties were calculated for the binary half-Heuslers $Sc_xLa_{1-x}NiBi$, $Sc_xY_{1-x}NiBi$ and $Y_xLa_{1-x}NiBi$ with x = (0.125, 0.25, 0.5, 0.75, 0.875), as well as the ternary half-Heusler $Sc_xY_yLa_{1-x-y}NiBi$ with x = (0.125, 0.25, 0.33, 0.5, 0.75) and y = (0.125, 0.25, 0.33, 0.5, 0.75). The calculation of the thermal conductivity was performed with the tetrahedron integration method for q-point meshes of 29, 31, 33 and 35 q-points in each lattice direction, and the thermal conductivity was interpolated using a least square method and found for q-distance equal 0. Note that in these calculations, both the anharmonic and the mass-disorder scattering are accounted for.

[1] Note that Vegard's law first was tested using a part of VASP that utilizes VCA (not to be confused with the VCA approach utilized in TDEP). However, the calculations failed. Thus, SQSes were used for the testing

4.2.2 Contributions to the thermal properties

Anharmonic vs mass-disorder scattering

In the relaxation time approximation, the two scattering mechanisms considered in the calculations described in the previous section, are independent. Thus, the thermal conductivity limited by the anharmonic scattering may be calculated separately from that limited by the mass-disorder scattering. However, this separation is not yet implemented in the TDEP method. Therefore, the anharmonic thermal conductivity, κ_{anh}, was calculated by linearly interpolating the lattice parameters and force constants according to the composition of the alloy while the X-position mass was allowed to remain that of the X-position element of the majority constituent. The thermal properties were then calculated as described in the previous section for the binary half-Heuslers $Sc_xLa_{1-x}NiBi$, $Sc_xY_{1-x}NiBi$ and $Y_xLa_{1-x}NiBi$ with x = (0.125, 0.25, 0.5, 0.75, 0.875), as well as the ternary half-Heusler $Sc_xY_yLa_{1-x-y}NiBi$ with x = (0.125, 0.25, 0.33, 0.5, 0.75) and y = (0.125, 0.25, 0.33, 0.5, 0.75).

Impact of interpolation

Changes in the thermal properties may also arise from other properties of the alloys. The impact of interpolation of the lattice parameter and the force constants on the thermal properties was investigated through calculations where both, one or neither of these properties were interpolated. In the cases where one or neither of the properties were interpolated, the non-interpolated property was taken from the parent material constituting the majority component of the alloy. In $Sc_{0.25}La_{0.75}NiBi$, for example, the majority component would be LaNiBi, and any non-interpolated property would be taken from LaNiBi.

An overview of the calculations performed on the bulk $Sc_xY_yLa_{1-x-y}NiBi$ half-Heusler alloys is shown in table 4.1. For simplicity, the calculations are divided into five categories, where the two first include the calculations described in section 4.2.1 and 4.2.2. The three last include the calculations described in this section. In category III, only the lattice parameter was interpolated from the parent materials, while the force constants were taken from one of the parents. In category IV, only the force constants were interpolated from the parents, and in category V neither the lattice parameter nor the force constants were interpolated, but merely taken form one of the parents. For all categories, except category II, mass substitution on the X-position according to the composition of the material was performed. As mentioned, the mass-substitution was omitted in category II to exclude the mass-disorder scattering. Note, however, that isotope scattering from the parent material still is included here.

Table 4.1: Overview of the calculations performed on $Sc_xY_yLa_{1-x-y}NiBi$ using the VCA approach

		Category					Force constants			Lattice parameter		
X-position element	Composition x, y	I	II	III	IV	V	Φ_{Sc}	Φ_Y	Φ_{La}	a_{Sc}	a_Y	a_{La}
Sc_xLa_{1-x}	0.125, 0.25, 0.5, 0.75, 0.875	x	x									
Sc_xY_{1-x}	0.125, 0.25, 0.5, 0.75, 0.875	x	x									
Y_xLa_{1-x}	0.125, 0.25, 0.5, 0.75, 0.875	x	x									
$Sc_xY_yLa_{1-x-y}$	0.125, 0.25, 0.33, 0.5, 0.75, 0.875	x	x									
Sc_xLa_{1-x}	0.25, 0.5, 0.75			x					x			
Sc_xLa_{1-x}	0.25, 0.5, 0.75			x			x					
Sc_xY_{1-x}	0.25, 0.5, 0.75			x				x				
Sc_xY_{1-x}	0.25, 0.5, 0.75			x			x					
Y_xLa_{1-x}	0.25, 0.5, 0.75			x					x			
Y_xLa_{1-x}	0.25, 0.5, 0.75			x				x				
Sc_xLa_{1-x}	0.25, 0.5, 0.75				x							x
Sc_xLa_{1-x}	0.25, 0.5, 0.75				x					x		
Sc_xY_{1-x}	0.25, 0.5, 0.75				x						x	
Sc_xY_{1-x}	0.25, 0.5, 0.75				x					x		
Y_xLa_{1-x}	0.25, 0.5, 0.75				x							x
Y_xLa_{1-x}	0.25, 0.5, 0.75				x						x	
Sc_xLa_{1-x}	0.25, 0.5, 0.75					x			x			x
Sc_xLa_{1-x}	0.25, 0.5, 0.75					x	x			x		
Sc_xY_{1-x}	0.25, 0.5, 0.75					x		x			x	
Sc_xY_{1-x}	0.25, 0.5, 0.75					x	x			x		
Y_xLa_{1-x}	0.25, 0.5, 0.75					x			x			x
Y_xLa_{1-x}	0.25, 0.5, 0.75					x		x			x	

Category I: Both lattice parameter and force constants interpolated from parents. Including anharmonic and mass-disorder scattering

Category II: Both lattice parameter and force constants interpolated from parents. Excluding mass-disorder scattering

Category III: Only lattice parameter interpolated from parents. Including anharmonic and mass-disorder scattering

Category IV: Only force constants interpolated from parents. Including anharmonic and mass-disorder scattering

Category V: Neither lattice parameter nor force constants interpolated from parents. Including anharmonic and mass-disorder scattering

Impact of strain During the course of the above calculations, the difference between the first and fourth category came out surprisingly small. The question of whether the calculations accounted for the increase and decrease of the lattice parameter was therefore raised. To evaluate the effect of strain, the thermal conductivity of pure ScNiBi (artificially) strained by -5%, -1%, 1% and 5% was calculated in two ways. In the first approach, the supercell was (artificially) strained and the force constants calculated for the strained structure using the TDEP method (i.e. following the procedure described in section 3.3.4 from point 2). In the second approach, the force constants from ScNiBi was used, and the thermal conductivity was calculated using the strained structure (i.e. omitting step 1-8, and only performing step 9 in the procedure in section 3.3.4)

4.3 Reducing the lattice thermal conductivity further

As discussed later in this thesis, the effect of alloying on the X-position in the XNiBi, X=(Sc, Y or La), is limited. Consequently, other methods to reduce the thermal conductivity was investigated.

4.3.1 Grain boundary scattering

One way to reduce the lattice thermal conductivity is to introduce grains to the bulk material, as discussed in section 2.3.5. The lattice thermal conductivity of the $Sc_xLa_{1-x}NiBi$ half-Heusler alloy with x=(0, 0.25, 0.5, 0.75, 1) and grain size of 50 nm in diameter was investigated using the VCA approach based on interpolation of the lattice parameter and force constants from ScNiBi and LaNiBi as described in section 4.2.1. Thus, both anharmonic and mass-disorder scattering was accounted for. The grain boundary scattering was included through the constant scattering term given in equation 2.21.

4.3.2 Isoelectronic substitution on the Bi-position

The effect of alloying with As and Sb on the Bi-position of YNiBi was investigated as a third way to reduce the lattice thermal conductivity. The calculations were performed using the VCA approach (described in section 4.2.1) with the lattice parameter and force constants from YNiBi. Thus, the lattice thermal conductivity of $YNiBi_xAs_{1-x}$ and $YNiBi_xSb_{1-x}$ with x=(0, 0.25, 0.5, 0.75) was found.

Chapter 5

Results

The results presented in this chapter are all calculated using the VCA approach as described in section 4.2. In the following section, both anharmonic and mass-disorder contribution contribute to the thermal properties. In addition, the properties of the alloy are interpolated from the parent materials. Later, however, different contributions will be considered alone, or in specified combinations.

5.1 Thermal properties of $Sc_xY_yLa_{1-x-y}NiBi$

The thermal properties in this section comprise both anharmonic and mass-disorder contributions as well as the contributions from the interpolated lattice parameter and force constants. In other words, the calculations belong to category I (see table 4.1).

5.1.1 Phonon density of states

The phonon density of states (DOS) of $Sc_xLa_{1-x}NiBi$, $Sc_xY_{1-x}NiBi$ and $Y_xLa_{1-x}NiBi$ with x=(0.25, 0.5, 0.75) is shown in figure 5.1. The acoustic, longitudinal optic and transverse optic phonon modes are plotted in red, purple and blue, respectively. The figure illustrates that as the average mass of the X-position element decreases (i.e. x goes from 0 to 1), the acoustic-optic phonon band gap increases. In addition, the DOS of the majority constituent is plotted. The phonon DOS of the $Sc_xY_{1-x}NiBi$ and $Y_xLa_{1-x}NiBi$ binaries are more closely related to that of the majority constituent than $Sc_xLa_{1-x}NiBi$ is. An exception from this general trend occurs for x=0.5 where, naturally, the phonon DOS of the alloy is located somewhere in-between the two parent half-Heuslers.

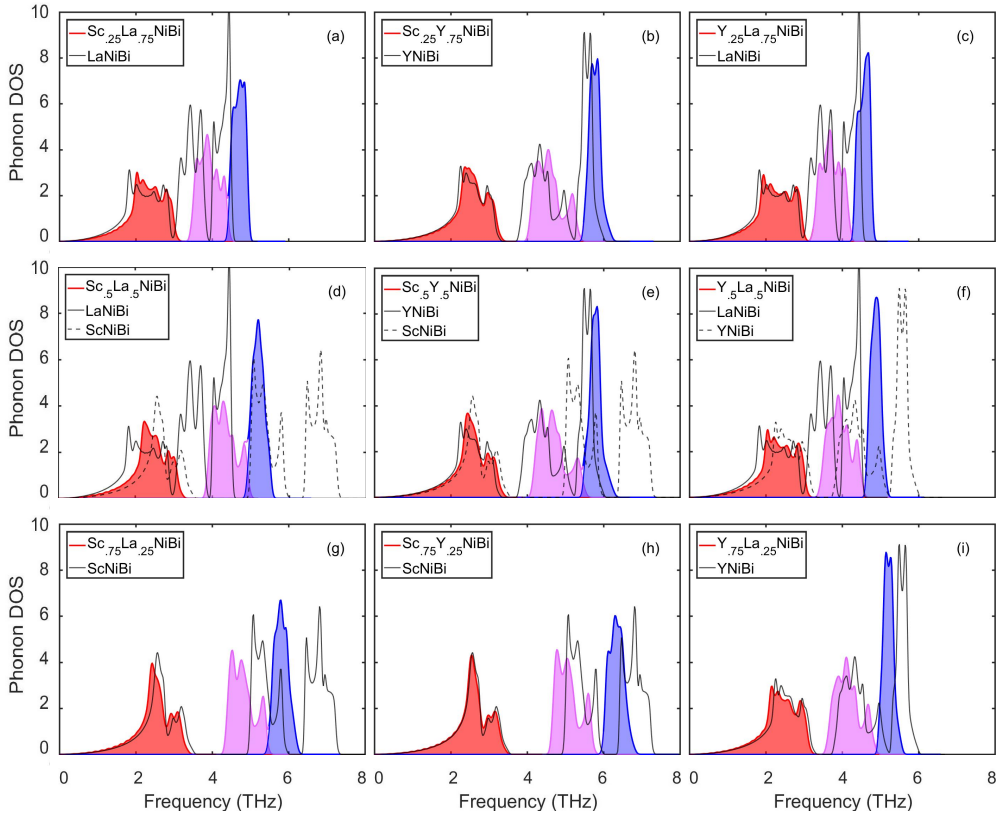

Figure 5.1: Phonon DOS projected on the phonon modes at 300 K for, from left to right, $Sc_xLa_{1-x}NiBi$, $Sc_xY_{1-x}NiBi$ and $Y_xLa_{1-x}NiBi$, and a-c) x=0.25, d-f) x=0.50, and g-i) x=0.75. The colours in the phonon DOS corresponds to acoustic (red), longitudinal optic (purple) and transverse optic (blue) phonon modes

While the the shape of the phonon DOS depends on the elements and concentrations of the elements on the X-position, the site projection of the elements within each phonon mode is similar for all of the alloys. Figure 5.2, showing the site-projected phonon modes for $Sc_xLa_{1-x}NiBi$, $Sc_xLa_{1-x}NiBi$ and $Sc_xLa_{1-x}NiBi$ with x=(0.25, 0.5, 0.75), illustrates that the acoustic phonon modes are dominated by Bi while the optic phonon modes are dominated by the X-position elements.

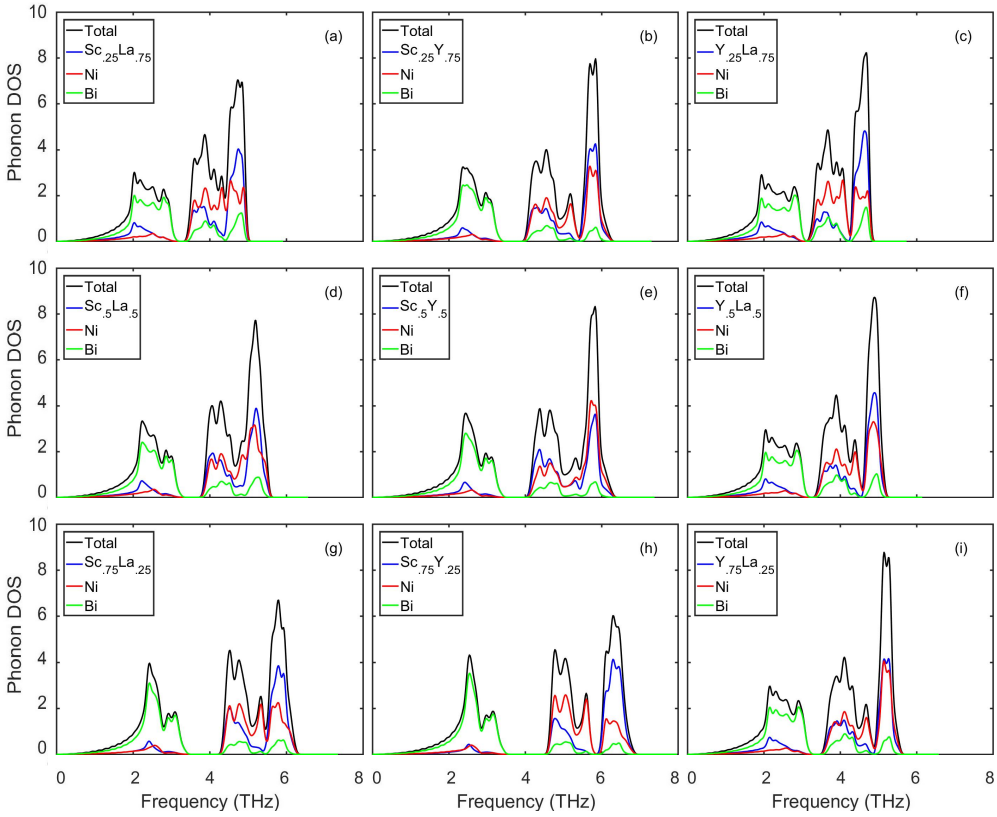

Figure 5.2: Phonon DOS projected on the atomic sites at 300 K for, from left to right, $Sc_xLa_{1-x}NiBi$, $Sc_xY_{1-x}NiBi$ and $Y_xLa_{1-x}NiBi$, and a-c) x=0.25, d-f) x=0.50, and g-i) x=0.75

5.1.2 Lattice thermal conductivity

Figure 5.3 shows the lattice thermal conductivity for $Sc_xLa_{1-x}NiBi$, $Sc_xY_{1-x}NiBi$ and $Y_xLa_{1-x}NiBi$ as a function of the composition, x, at a fixed temperature, T = 300 K. While the crosses represent the calculated values, the solid lines are fourth degree polynomial interpolations. The minimum value for $Sc_xLa_{1-x}NiBi$, $Sc_xY_{1-x}NiBi$ and $Y_xLa_{1-x}NiBi$ is 4.31 W/mKat 24% Sc, 7.13 W/mK at 25% Sc and 5.02 W/mK at 25% Y, respectively.

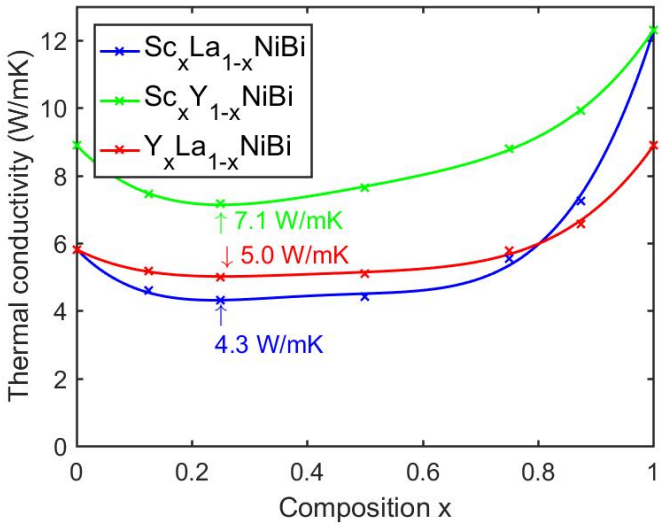

Figure 5.3: Lattice thermal conductivity of $Sc_xLa_{1-x}NiBi$, $Sc_xY_{1-x}NiBi$ and $Y_xLa_{1-x}NiBi$ as a function of the composition, x, at 300 K. The minimum conductivity of $Sc_xLa_{1-x}NiBi$, $Sc_xY_{1-x}NiBi$ and $Y_xLa_{1-x}NiBi$ is shown in green, red and blue, respectively. The crosses represent the calculated values, the solid lines are fourth degree polynomial interpolations.

The cumulative lattice thermal conductivity at 300 K is given as a function of the phonon mean free path in figure 5.4a, 5.4b and 5.4c for $Sc_xLa_{1-x}NiBi$, $Sc_xY_{1-x}NiBi$ and $Y_xLa_{1-x}NiBi$, respectively.

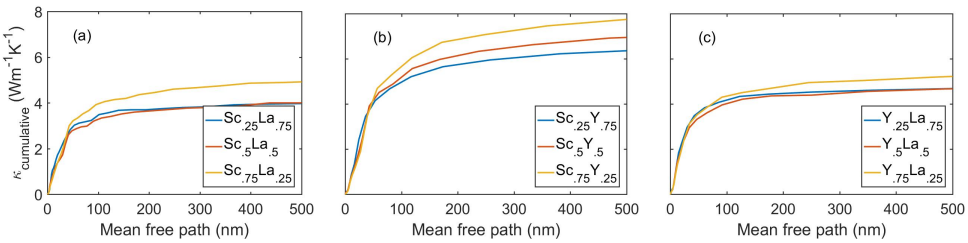

Figure 5.4: Cumulative lattice thermal conductivity as a function of the mean free path at 300 K of a) $Sc_xLa_{1-x}NiBi$, b) $Sc_xY_{1-x}NiBi$ and c) $Y_xLa_{1-x}NiBi$ for x=(0.25, 0.5, 0.75)

A ternary plot of the lattice thermal conductivity for $Sc_xY_yLa_{1-x-y}NiBi$ at 300 K is given in figure 5.5. The minimum thermal conductivity, 4.31 W/mK, is found for the binary alloy $Sc_xLa_{1-x}NiBi$ around x=0.25. The maximum thermal conductivity occurs at ScNiBi, but decreases rapidly as the concentration particularly of La increases.

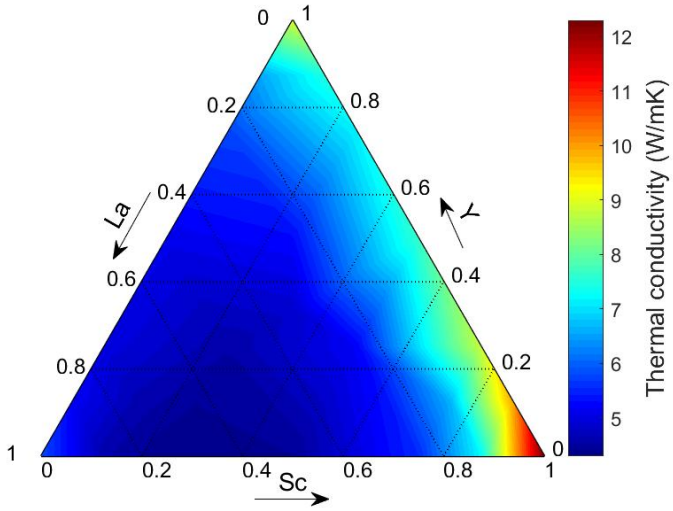

Figure 5.5: Ternary plot of the lattice thermal conductivity for $Sc_xY_yLa_{1-x-y}NiBi$ at 300 K. The lower left corner corresponds to LaNiBi, the lower right to ScNiBi and the top corner to YNiBi

5.2 Contributions to the thermal properties

5.2.1 Anharmonic vs mass-disorder scattering

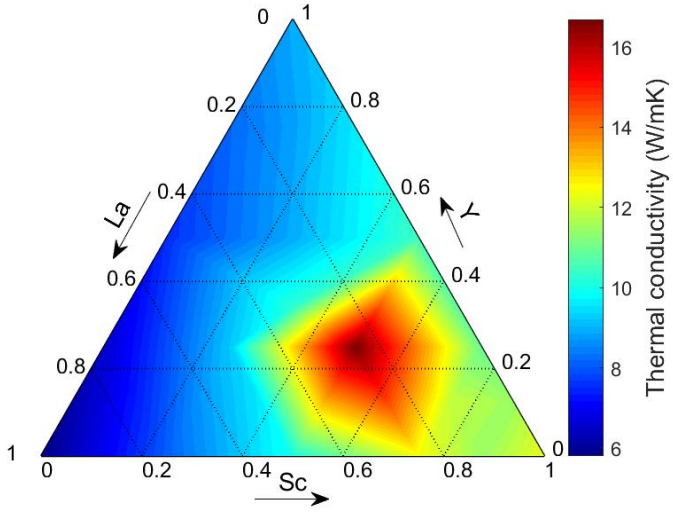

Figure 5.6: Ternary plot of the anharmonic lattice thermal conductivity of $Sc_xY_yLa_{1-x-y}NiBi$ at 300 K. The lower left corner corresponds to LaNiBi, the lower right to ScNiBi and the top corner to YNiBi

In this section, the results from the category II calculations (see definitions in table 4.1) are presented. Thus, both the lattice parameter and the force constants of the alloys are linearly interpolated, but only the anharmonic contributions are considered. The anharmonic lattice thermal conductivity of $Sc_xY_yLa_{1-x}NiBi$, κ_{anh}, at 300 K is shown in figure 5.6. The minimum κ_{anh} is 5.77 W/mK and occurs for LaNiBi. Note that the maximum κ_{anh} occurs not at ScNiBi, but $Sc_{0.5}Y_{0.25}La_{0.25}NiBi$. Similarly, the maximum κ_{anh} on the $Sc_xLa_{1-x}NiBi$ binary alloy occurs at $Sc_{0.75}La_{0.25}NiBi$ rather than ScNiBi. On the $Sc_xY_{1-x}NiBi$ and $Y_xLa_{1-x}NiBi$, however, the maximum κ_{anh} is found for ScNiBi and YNiBi, respectively. Note also that, in general, κ_{anh} is lower on the $Y_xLa_{1-x}NiBi$ side than the $Sc_xY_{1-x}NiBi$. However, the rapid decrease in the thermal conductivity as ScNiBi is alloyed with Y and/or La seen in figure 5.5, is not present in figure 5.6.

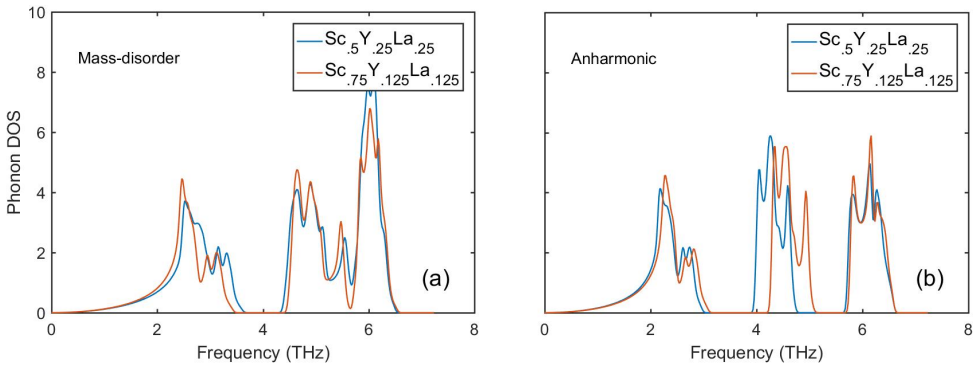

Figure 5.7: Phonon DOS at 300 K for $Sc_{0.5}Y_{0.25}La_{0.25}NiBi$ and $Sc_{0.75}Y_{0.125}La_{0.125}NiBi$ with a) both anharmonicity and mass-disorder included, and b) only anharmonicity included

To investigate the composition of the maximum κ_{anh} further, the phonon DOS of $Sc_{0.5}Y_{0.25}La_{0.25}NiBi$ is compared to that of $Sc_{0.75}Y_{0.125}La_{0.125}NiBi$ in figure 5.7. Figure 5.7a shows the phonon DOSes including contributions both from anharmonic and mass-disorder scattering (i.e. showing category I calculations). Here, the longitudinal optic-transverse optic phonon band gap increases from $Sc_{0.5}Y_{0.25}La_{0.25}NiBi$ to $Sc_{0.75}Y_{0.125}La_{0.125}NiBi$. Simultaneously, the total lattice thermal conductivity increases from 5.19 W/mK to 6.63 W/mK. In figure 5.7b where only the anharmonic contributions are considered, however, the longitudinal optic-transverse optic phonon band gap decreases from $Sc_{0.5}Y_{0.25}La_{0.25}NiBi$ to $Sc_{0.75}Y_{0.125}La_{0.125}NiBi$. This corresponds to a decrease in the anharmonic thermal conductivity from 16.48 W/mK to 11.74 W/mK as illustrated in figure 5.6.

5.2.2 Impact of interpolation

In figure 5.8, the lattice thermal conductivity of $Sc_xLa_{1-x}NiBi$ for category I, III and V calculations (defined in table 4.1) at 300 K are shown. The crosses in the figure defines the calculations while the solid lines are 4th degree polynomical interpolations. The category III calculations in figure 5.8a, κ_{III}, utilize the force constants of ScNiBi, whereas those of LaNiBi are used in figure 5.8b. Similarly, figure 5.8a and b show the

results from the category V calculations, κ_{V}, using the lattice parameter and force constants from ScNiBi and LaNiBi, respectively. The figures illustrate that κ_{III} and κ_{V} are similar both when properties from ScNiBi and from LaNiBi are used. $\kappa_{\mathrm{III,La}}$ and $\kappa_{\mathrm{V,La}}$ are also relatively similar to κ_{I}. $\kappa_{\mathrm{III,Sc}}$ and $\kappa_{\mathrm{V,Sc}}$, on the other hand, fail to estimate the lattice thermal conductivity of $\mathrm{Sc}_x\mathrm{La}_{1-x}\mathrm{NiBi}$ when x<0.8.

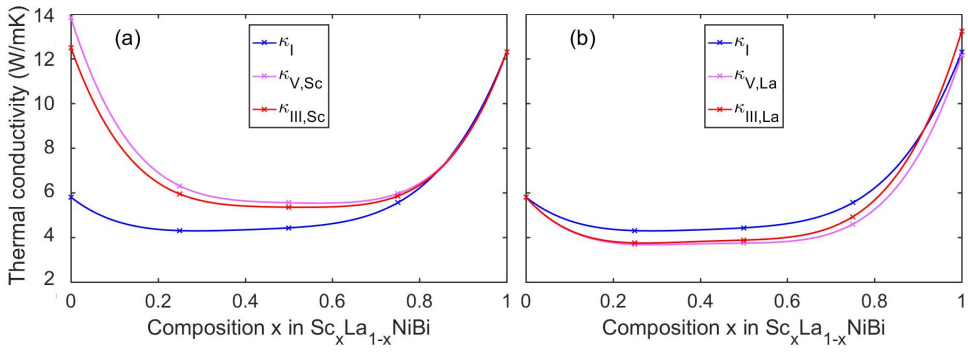

Figure 5.8: Lattice thermal conductivity of $\mathrm{Sc}_x\mathrm{La}_{1-x}\mathrm{NiBi}$ at 300 K for category III and IV calculations using lattice parameter and/or force constants from a) LaNiBi and b) ScNiBi. For comparison, the total thermal conductivity, κ_{I}, is shown in both a and b. The crosses in the figure defines the calculations while the solid lines are 4th degree polynomical interpolations.

The same trend is found for κ_{III} compared to κ_{I} in $\mathrm{Sc}_x\mathrm{La}_{1-x}\mathrm{NiBi}$ and $\mathrm{Sc}_x\mathrm{La}_{1-x}\mathrm{NiBi}$. When the force constants of the least anharmonic parent half-Heusler is used, κ_{III} of the most anharmonic parent (i.e. the opposite end point) deviates from κ_{I} as illustrated in figures 5.9a and b. If the force constants from the most anharmonic parent is used, on the other hand, figures 5.9c and d show that κ_{III} follow κ_{I} relatively well.

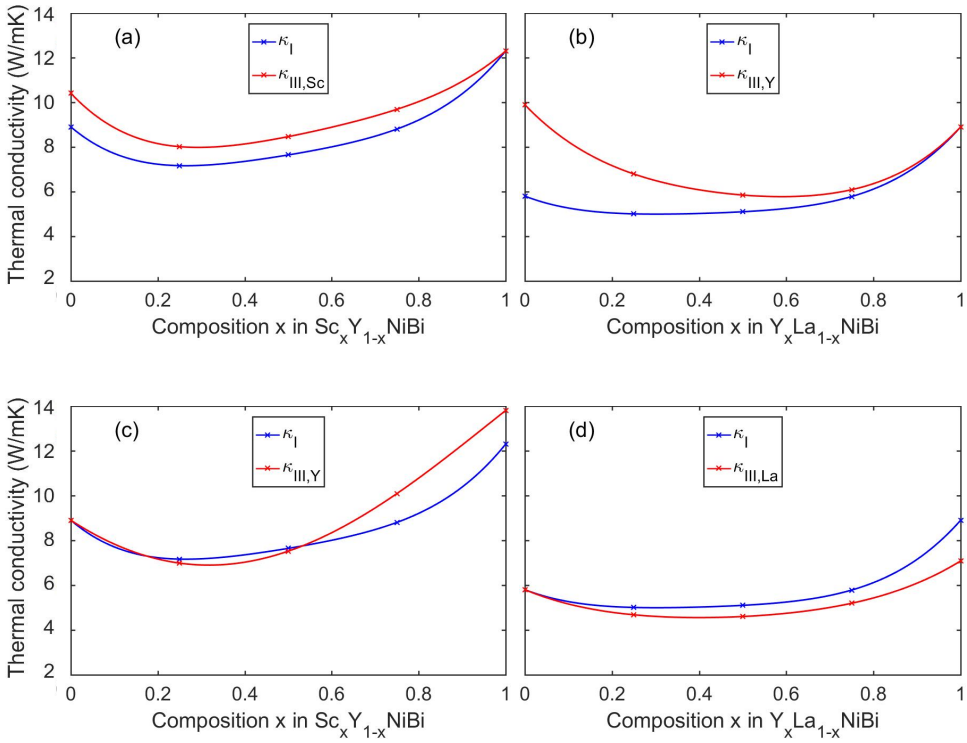

Figure 5.9: Category I and III calculations of the lattice thermal conductivity at 300 K of a) and c) $Sc_xY_{1-x}NiBi$, and b) and d) $Y_xLa_{1-x}NiBi$. The category III calculations use force constants from a) ScNiBi, b) YNiBi, c) YNiBi and d) LaNiBi. The crosses in the figure defines the calculations while the solid lines are 4th degree polynomical interpolations.

Effect of strain

The effect of uniform strain (i.e. equal elongation or compression of the lattice in each lattice direction) on the total lattice thermal conductivity of ScNiBi is shown in figure 5.10. κ_{TDEP} describes the thermal conductivity calculated with the complete TDEP method, meaning that step 2 through 9 of the list in section 3.3.4. κ_{VCA} is the thermal conductivity calculated with a "VCA like" approach where the force constants from the equilibrium ScNiBi are used directly in the thermal conductivity calculations (i.e. all steps, but step 9 in the list of section 3.3.4 are omitted). The crosses in the figure defines the calculations while the solid lines are 4th degree polynomical interpolations. In the figure, negative strain describes compression while positive describes elongation of the lattice in each lattice direction. The inset in figure 5.10 illustrates that κ_{TDEP} deviates from κ_{VCA} even for small changes in the lattice parameter. However, figure 5.11 shows that the phonon DOS of the 1% and -1% strained ScNiBi are relatively similar to that of the equilibrium (i.e. unstrained) ScNiBi.

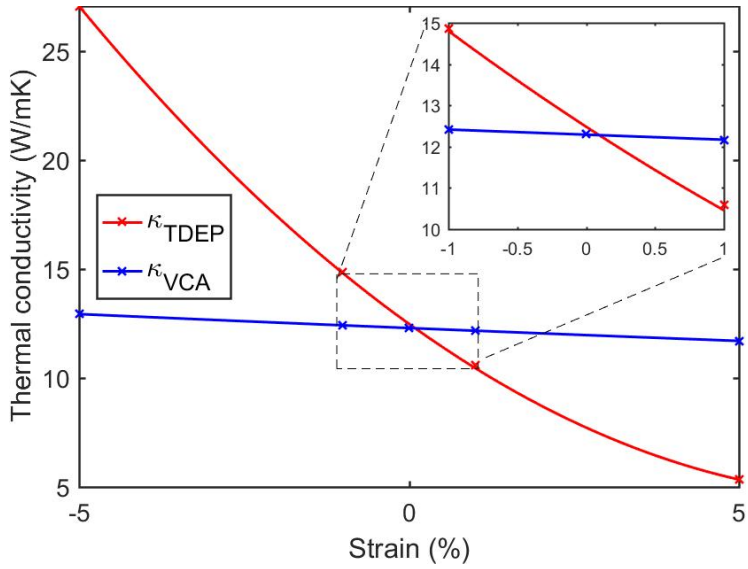

Figure 5.10: Lattice thermal conductivity of ScNiBi as a function of strain at 300 K. Negative strain describes compression in each lattice direction of the supercell while positive strain describes the elongation of the supercell in each lattice direction. κ_{VCA} is the thermal conductivity calculated with the "VCA like" approach (i.e. using the force constants of the equilibrium ScNiBi with artificially strained supercell). κ_{TDEP} is the thermal conductivity calculated with the complete TDEP method (i.e. from step 2 through 9 in the list in section 3.3.4). The inset shows the lattice thermal conductivity between -1% and 1% strain. The crosses in the figure defines the calculations while the solid lines are 2th degree polynomical interpolations.

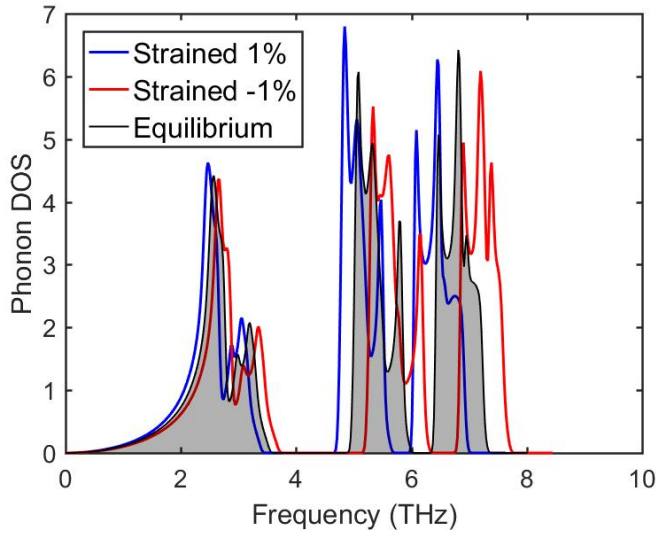

Figure 5.11: Phonon DOS at 300 K of 1% strained and -1% strained ScNiBi. The phonon DOS of the equilibrium ScNiBi is shown as the shaded area.

5.3 Reducing the lattice thermal conductivity further

5.3.1 Effect of grain boundary scattering

In the above presented results, a monocrystalline bulk material is considered. However, figure 5.12 illustrates the effect of introducing grains to the bulk material. With grains of size 50 nm, the lattice thermal conductivity of ScNiBi is reduced with 60%, of LaNiBi with 35% and minimum value of $Sc_xLa_{1-x}NiBi$ with 45% compared to the bulk material. While the global minimum still occurs for the alloy, the decrease upon alloying, particularly of ScNiBi, is significantly reduced compared to the effect of alloying on the bulk sample. Moreover, the composition for which the minimum occurs is shifted towards ScNiBi in the nanocrystalline material.

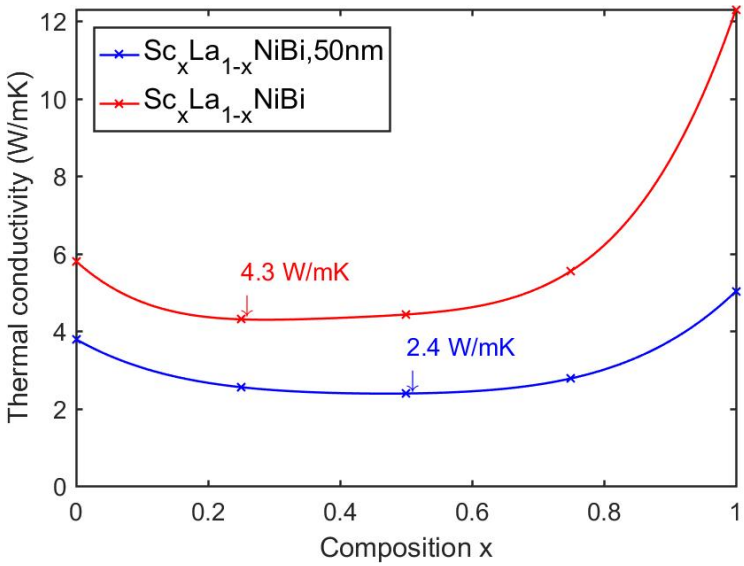

Figure 5.12: Lattice thermal conductivity of bulk $Sc_xLa_{1-x}NiBi$ compared to $Sc_xLa_{1-x}NiBi$ with 50 nm grains at 300 K as a function of the composition x. The crosses in the figure defines the calculations while the solid lines are 4th degree polynomical interpolations.

5.3.2 Effect of alloying on the Bi-position

While the alloying on the X-position, affects the optic phonons (as shown in figure 5.1), figure 5.13 shows that alloying on the Bi-position (i.e. the Z-position) with As or Sb affects the acoustic phonon modes. Particularly for $YNiBi_xAs_{1-x}$ as x goes from 0.25 to 0.5, the contribution to the acoustic phonon modes from Bi and As increases, but the trend (i.e. increasing contribution as x increases) is also seen for the rest of the $YNiBi_xAs_{1-x}$ alloys and the $YNiBi_xSb_{1-x}$ alloys. In addition, the acoustic-optic phonon band gaps increase as x increases, resulting in an increasing deviation from the phonon DOS of YNiBi. This is also illustrated in figure 5.14.

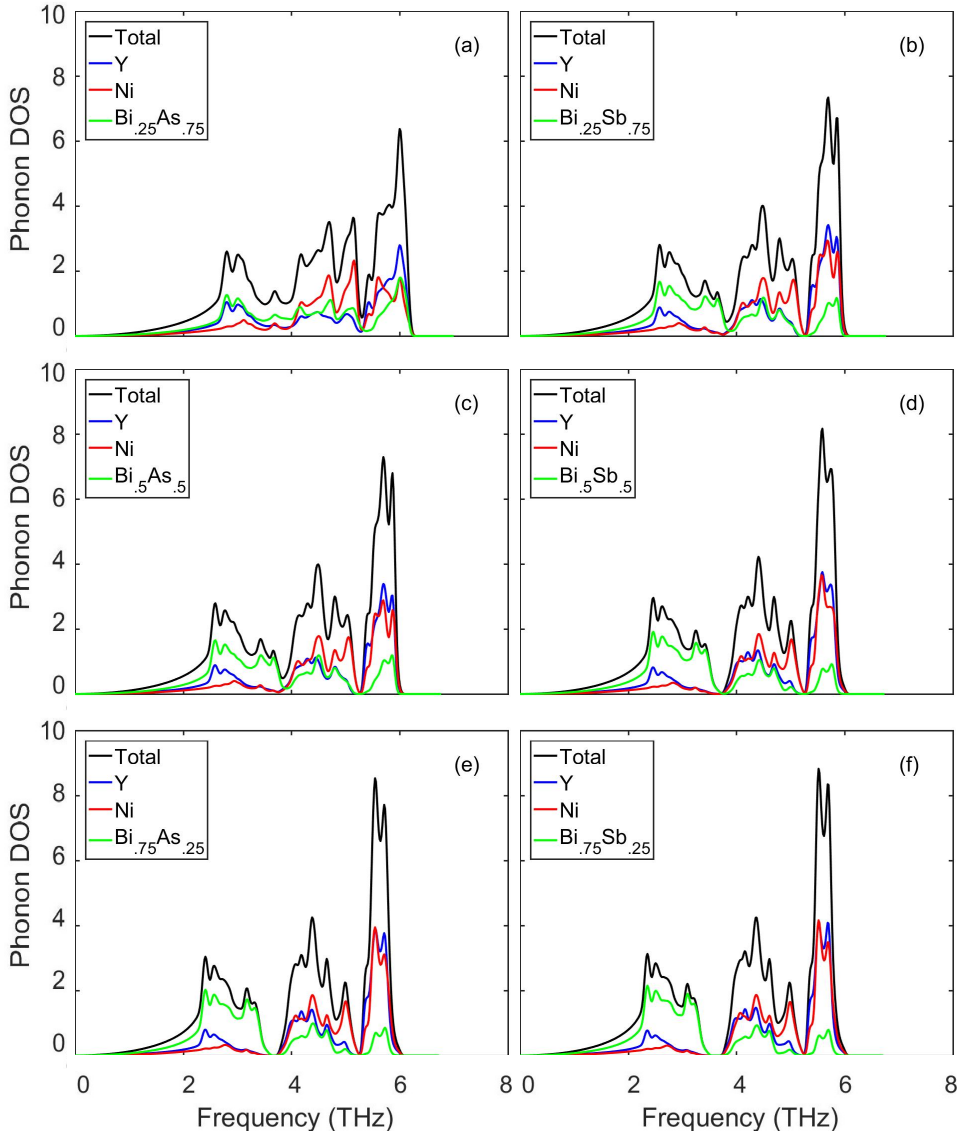

Figure 5.13: Phonon DOS projected on the sites of $YNiBi_xAs_{1-x}$ (left column) and $YNiBi_xSb_{1-x}$ (right column) for a-b) x=0.25, c-d) x=0.5 and e-f) x=0.75. The phonon DOSes are calculated for 300 K

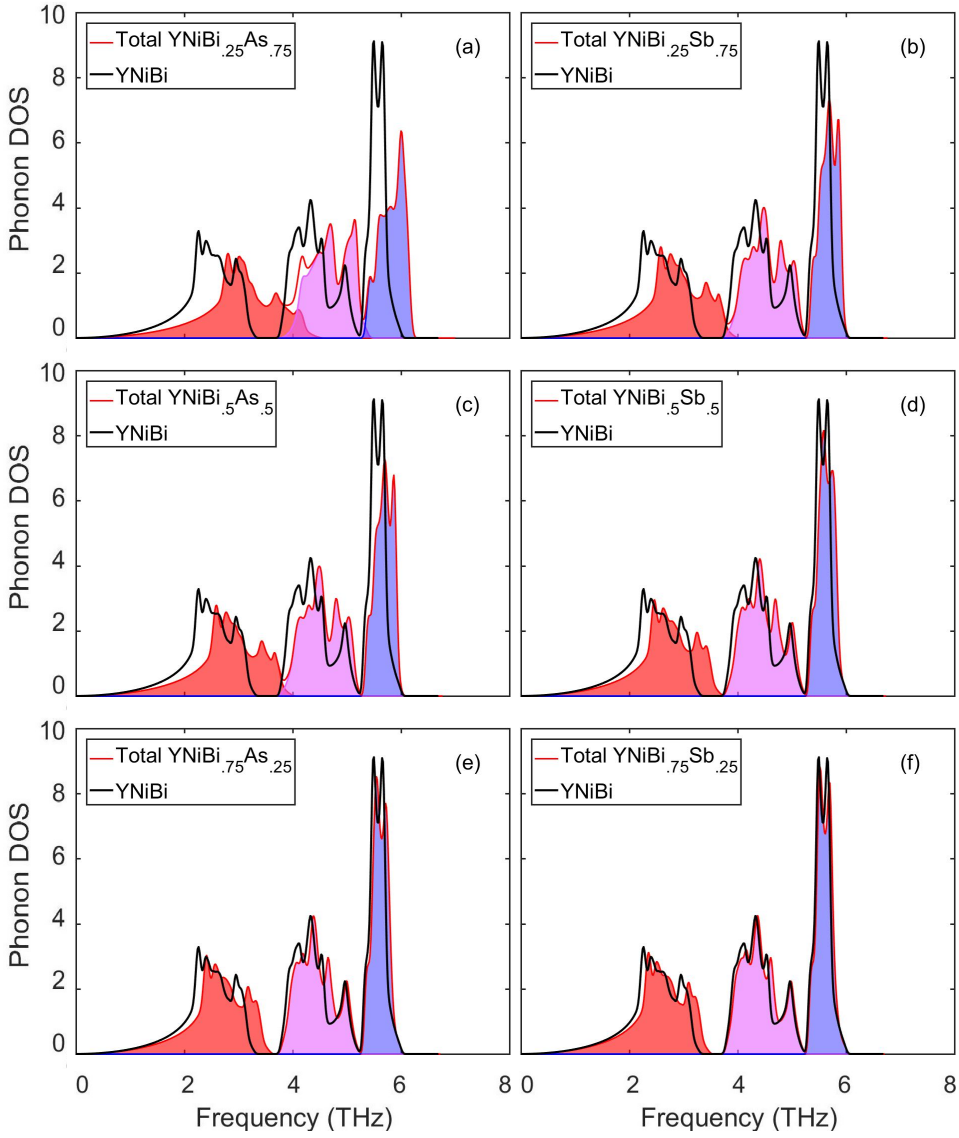

Figure 5.14: Phonon DOS projected on the phonon modes of $YNiBi_xAs_{1-x}$ (left column) and $YNiBi_xSb_{1-x}$ (right column) for a-b) x=0.25, c-d) x=0.5 and e-f) x=0.75. The phonon DOSes are calculated for 300 K. The colours in the phonon DOS corresponds to acoustic (red), longitudinal optic (purple) and transverse optic (blue) phonon modes. The phonon DOS of YNiBi is shown in black.

The lattice thermal conductivity of the $YNiBi_xAs_{1-x}$ and the $YNiBi_xSb_{1-x}$ binary alloys at 300 K is shown in figure 5.15. The crosses represent the calculated values while the solid lines are 4th degree polynomial fits of the calculated values. The minimum lattice thermal conductivity is 2.36 W/mK for $YNiBi_xAs_{1-x}$ at x=0.36 and 3.52 W/mK for $YNiBi_xSb_{1-x}$ at x=0.38. Note that while the thermal conductivity is lower for the $YNiBi_xAs_{1-x}$ binary as long as x is greater than 0.1, it is higher for YNiAs than for YNiSb.

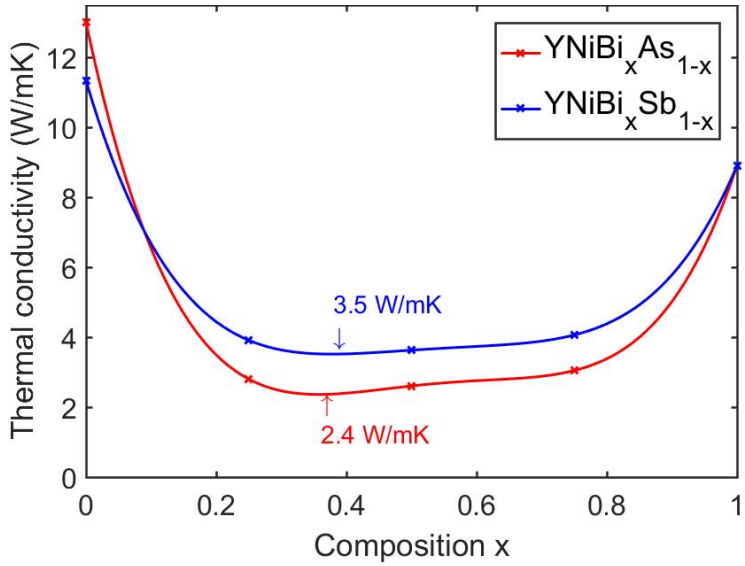

Figure 5.15: Lattice thermal conductivity of $YNiBi_xAs_{1-x}$ and $YNiBi_xSb_{1-x}$ at 300 K. The crosses in the figure defines the calculations while the solid lines are 4th degree polynomical interpolations.

Chapter 6

Discussion

6.1 Effect of alloying

In the specialization project, the calculated lattice thermal conductivity was found to decrease from ScNiBi to LaNiBi. The reason for the decrease was ascribed to the increase in the mass of the X-position element upon substitution of Sc with Y or La, which cause the acoustic-optic phonon band gap to decrease. As a result, the anharmonic scattering of the acoustic phonon modes increases and the lattice thermal conductivity decreases. Upon partial substitution on the X-position of one element with another, a similar trend is observed. Figure 5.1 shows that the acoustic-optic phonon band gap increases as the average mass of the X-position elements decreases. For example, the acoustic-optic phonon band gap of $Sc_xLa_{1-x}NiBi$ decreases as x goes from 1 to 0. Similarly, the phonon band gap of $Sc_xY_{1-x}NiBi$ is larger than that of $Sc_xLa_{1-x}NiBi$, which is larger that of $Y_xLa_{1-x}NiBi$.

As opposed to the pure XNiBi, X=(Sc, Y or La), half-Heuslers, however, the anharmonic scattering is not the only scattering mechanism in the $Sc_xY_yLa_{1-x}NiBi$ alloys. The partial substitution on the X-position introduces mass-disorder to the lattice, which causes the phonons to be scattered. The degree of mass-disorder scattering depends on the mass-disorder parameter from equation 2.19, which is shown in figure 6.1 for the $Sc_xY_yLa_{1-x-y}NiBi$ ternary alloy. The lattice thermal conductivity is therefore a function of the anharmonicity and the mass-disorder. Since the anharmonic and mass-disorder relaxation time are independent of one another in the relaxation time approximation, the anharmonic thermal conductivity, κ_{anh}, may be calculated separately from the mass-disorder thermal conductivity, κ_{md}. Figure 5.6 shows κ_{anh} for $Sc_xY_yLa_{1-x-y}NiBi$. In accordance with the trend in the phonon DOSes of the binary alloys discussed earlier in this section, κ_{anh} is lowest for the $Y_xLa_{1-x}NiBi$ binary where the acoustic-optic phonon band gap is lowest, highest for the $Sc_xY_{1-x}NiBi$ binary and reaches a minimum for LaNiBi. However, the composition for which κ_{anh} reaches a maximum conflicts with the presented hypothesis. This phenomenon is discussed at the end of this section.

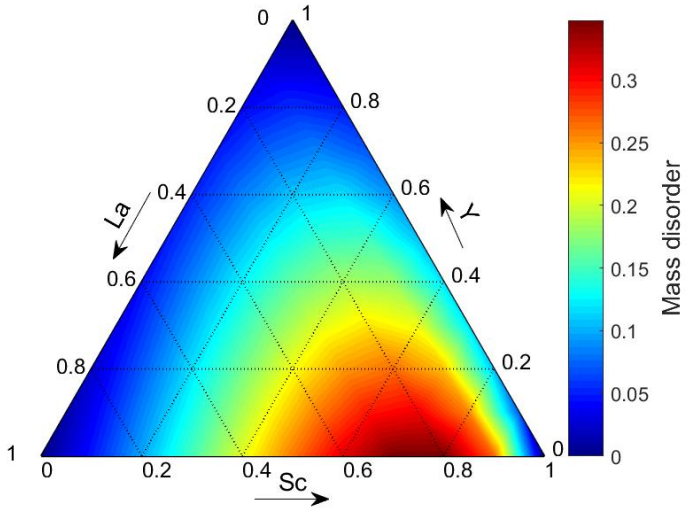

Figure 6.1: The mass-disorder parameter of $Sc_xY_yLa_{1-x-y}NiBi$. Pure ScNiBi, YNiBi and LaNiBi is found in the lower right, upper and lower left corner, respectively

Equation 2.20 and 2.16 show that the inverse of the mass-disorder parameter describes κ_{md}. Since the mass-disorder parameter is highest for the $Sc_xLa_{1-x}NiBi$ binary alloy, κ_{md} is expected to be smaller for $Sc_xLa_{1-x}NiBi$ than for $Sc_xY_{1-x}NiBi$ and $Y_xLa_{1-x}NiBi$. This behaviour is almost the exact opposite of κ_{anh}. κ_{md} and κ_{anh} will therefore counteract each other such that the minimum total lattice thermal conductivity occurs between the minimum of the individual contributors. This is illustrated in the ternary plot of the total lattice thermal conductivity at 300 K in figure 5.5, where the minimum thermal conductivity is found at the $Sc_xLa_{1-x}NiBi$ binary for 24% Sc and 76% La. Note that the minimum thermal conductivity occurs slightly closer to LaNiBi than expected if, as suggested in figure 5.6 and 6.1, κ_{md} was the exact opposite of κ_{anh}. This indicates that κ_{anh} contributes more to the total lattice thermal conductivity than κ_{md} causing a shift of the minimum total lattice thermal conductivity towards the minimum of κ_{anh} at LaNiBi.

The domination of κ_{anh} may be caused by the nature of the anharmonic and mass-disorder scattering. In figure 5.2, the phonon DOSes projected on the atomic sites of $Sc_xLa_{1-x}NiBi$, $Sc_xY_{1-x}NiBi$ and $Y_xLa_{1-x}NiBi$ show that the acoustic phonon modes are dominated by Bi whereas the optic phonon modes are dominated by the X-position elements. Consequently, mass-disorder primarily induces scattering of the optic phonon modes. The anharmonic scattering, on the other hand, affects the acoustic phonon modes, as discussed at the beginning of this section. Consequently, increasing the degree of anharmonicity scatters the heat carriers more efficiently than increasing the mass-disorder does. Thus, the minimum total lattice thermal conductivity is shifted towards LaNiBi.

The surprising location of the maximum κ_{anh} was mentioned briefly in the beginning of the section. As discussed above, the minimum κ_{anh} follows the trend of decreasing thermal conductivity as the concentration of La increases, and reaches its minimum at LaNiBi which exhibits the highest degree of anharmonicity of the three pure half-

Heuslers. The maximum κ_{anh}, on the other hand, occurs for $Sc_{0.5}Y_{0.25}La_{0.25}NiBi$, rather than the pure half-Heusler exhibiting the lowest degree of anharmonicity, ScNiBi. A possible explanation for this phenomenon may rest in the phonon DOS of the binary and ternary alloys containing Sc. Figure 5.7 shows the phonon DOS of $Sc_{0.5}Y_{0.25}La_{0.25}NiBi$ compared to $Sc_{0.75}Y_{0.125}La_{0.125}NiBi$ for mass-disorder scattering included (in a) and excluded (in b). In the case of the anharmonic DOS (figure 5.7b, the gap between the longitudinal and transverse optic modes decrease slightly from $Sc_{0.75}La_{0.25}NiBi$ to $Sc_{0.875}La_{0.125}NiBi$. This may cause an increase in the scattering of the optic phonon modes in the latter compared to the first composition, resulting in the unexpected decrease in the anharmonic thermal conductivity. When the mass-disorder scattering is included, however, the gap between the longitudinal and transverse optic increases from $Sc_{0.5}Y_{0.25}La_{0.25}NiBi$ to $Sc_{0.75}Y_{0.125}La_{0.125}NiBi$. Since the total lattice thermal conductivity increases from $Sc_{0.5}Y_{0.25}La_{0.25}NiBi$ to $Sc_{0.75}Y_{0.125}La_{0.125}NiBi$, there might be a relation between the LO-TO phonon band gap and the lattice thermal conductivity.

Interestingly, this phenomenon seems only to occur for binary and ternary compounds containing moderate amounts of Sc and La. For example, κ_{anh} decreases from $Sc_{0.75}La_{0.25}NiBi$ to $Sc_{0.875}La_{0.125}NiBi$, but increases as x goes from 0 to 1 both for the $Sc_xY_{1-x}NiBi$ and the $Y_xLa_{1-x}NiBi$ binary alloys. The mechanism of this behaviour is not fully understood. Artifacts in the simulations may cause the irregularities. However, they may also be caused by changes in the interatomic forces at these compositions, which affect the force constants, and thus κ_{anh}.

6.2 Impact of force interpolation

Figures 5.8a and b show the lattice thermal conductivity of $Sc_xLa_{1-x}NiBi$ for category III and V calculations (defined in table 4.1) with the lattice parameter and/or the force constants from LaNiBi and ScNiBi, respectively. In addition the total lattice thermal conductivity, κ_{I}, is shown in blue. In figure 5.8b the thermal conductivity with force constants from ScNiBi, $\kappa_{\mathrm{III,Sc}}$, deviates significantly from κ_{I} for increasing concentration of La on the X-position. At LaNiBi the deviation reaches its maximum at 115.5% as shown in table 6.1. As discussed previously, the anharmonic thermal conductivity dominates the total lattice thermal conductivity for high concentrations of La in the alloy. Replacing the interpolated force constants with force constants from ScNiBi, effectively removes the anharmonic contribution to the thermal conductivity resulting in higher thermal conductivity for the La-rich alloys than if the anharmonic scattering (in terms of the interpolated force constants) also was accounted for. In other words, the behaviour of $\kappa_{\mathrm{III,Sc}}$ in figure 5.8b supports the hypothesis of the relation between the anharmonic and mass-disorder thermal conductivity from the previous section; for the compositions close to ScNiBi, where the mass-disorder parameter shown in figure 6.1 is largest, the mass-disorder thermal conductivity dominates, causing $\kappa_{\mathrm{III,Sc}}$ to follow the total lattice thermal conductivity. However, as the concentration of La increases, the anharmonic thermal conductivity dominates, and $\kappa_{\mathrm{III,Sc}}$ starts to deviate from the total lattice thermal conductivity. At LaNiBi there is no mass-disorder on the X-position. $\kappa_{\mathrm{III,Sc}}$, having the force constants of ScNiBi and no mass-disorder to reduce the thermal conductivity, therefore increases to a value close to the total lattice thermal conductivity of ScNiBi. Equivalent trends are seen for the category III thermal conductivity of $Sc_xY_{1-x}NiBi$ and $Y_xLa_{1-x}NiBi$ using the force constants

from ScNiBi and YNiBi, respectively. This is illustrated in figures 5.9a and b.

Table 6.1: The deviations of κ_{III} from κ_{I}. Here, κ_{III}* denotes the lattice thermal conductivity utilizing the force constants from the most anharmonic parent half-Heusler. For $Sc_xLa_{1-x}NiBi$, for example, this is $\kappa_{\mathrm{III,La}}$. κ_{III}** denotes the lattice thermal conductivity utilizing the force constants from the least anharmonic parent half-Heusler. In $Sc_xLa_{1-x}NiBi$, this is $\kappa_{\mathrm{III,Sc}}$. The deviations are calculated as $\frac{\kappa_{\mathrm{III}}(\mathrm{material})}{\kappa_{\mathrm{I}}(\mathrm{material})} - 1$. Thus, in $Sc_xLa_{1-x}NiBi$, the deviation of κ_{III}* from κ_{I} is calculated at ScNiBi: $\frac{\kappa_{\mathrm{III,La}}(\mathrm{ScNiBi})}{\kappa_{\mathrm{I}}(\mathrm{ScNiBi})} - 1 \approx 7.6\%$. The definitions of the category I and III calculations from table 4.1 are included.

Material	κ_{III}*	Deviation from κ_{I} (%)	κ_{III}**	Deviation from κ_{I} (%)
$Sc_xLa_{1-x}NiBi$	$\kappa_{\mathrm{III,La}}$(ScNiBi)	7.6	$\kappa_{\mathrm{III,Sc}}$(LaNiBi)	115.5
$Sc_xY_{1-x}NiBi$	$\kappa_{\mathrm{III,Y}}$(ScNiBi)	12.2	$\kappa_{\mathrm{III,Sc}}$(YNiBi)	17.0
$Y_xLa_{1-x}NiBi$	$\kappa_{\mathrm{III,La}}$(YNiBi)	-20.4	$\kappa_{\mathrm{III,Y}}$(LaNiBi)	70.6

* κ_{III} from the most anharmonic parent (e.g. for $Sc_xLa_{1-x}NiBi$, this is $\kappa_{\mathrm{III,La}}$)

** κ_{III} from the least anharmonic parent (e.g. for $Sc_xLa_{1-x}NiBi$, this is $\kappa_{\mathrm{III,Sc}}$)

Category I: Both lattice parameter and force constants interpolated from parents. Including anharmonic and mass-disorder scattering. (Also referred to as the total lattice thermal conductivity)

Category III: Only lattice parameter interpolated from parents. Including anharmonic and mass-disorder scattering

The thermal conductivity of the opposite case, $\kappa_{\mathrm{III,La}}$ shown in figure 5.8a, where the interpolated force constants are replaced by force constants from LaNiBi, behaves in line with the argumentation above as x goes from 0; the LaNiBi force constants yield a higher degree of anharmonicity than the interpolated force constants while the mass-disorder remains the same. As a result, $\kappa_{\mathrm{III,La}}$ follows the same trend as the total lattice thermal conductivity, but is slightly smaller. According to the hypothesis discussed earlier in this section, the anharmonicity induced by the LaNiBi force constants is expected to prevent $\kappa_{\mathrm{III,La}}$ from increasing as much as the total lattice thermal conductivity does when x approaches 1. However, figure 5.8a shows that $\kappa_{\mathrm{III,La}}$ larger than the total lattice thermal conductivity at ScNiBi. The same trend is observed for $Sc_xY_{1-x}NiBi$ in figure 5.9c.

In figure 5.9d, however, $\kappa_{\mathrm{III,La}}$ is lower for YNiBi than κ_{I}. Nevertheless, $\kappa_{\mathrm{III,La}}$ also exhibits closer relation to the total lattice thermal conductivity than $\kappa_{\mathrm{III,Y}}$. Thus, $\kappa_{\mathrm{III,La}}$ behaves in line with the general trend; the lattice thermal conductivity utilizing the force constants from the most anharmonic parent, κ_{III}*, deviates less form the total lattice thermal conductivity, κ_{I}, than the lattice thermal conductivity utilizing the force constants of the least anharmonic parent, κ_{III}**. This trend is illustrated in table 6.1 when comparing the left with the right column.

6.3 Validity of linearly interpolated force constants

As discussed in section 2.3.3, the interaction strength between atoms in the lattice depends among others on the distance between the atoms. Changes in the lattice

parameter therefore affect the force constants, and ultimately the thermal conductivity. However, figure 5.8 shows that κ_{III} and κ_V are similar. Since the only difference between κ_{III} and κ_V is whether the lattice parameter is interpolated or not, this indicates, in contradiction to the theory of section 2.3.3, that the thermal conductivity is largely insensitive to changes in the lattice parameter.

Consequently, the question of whether changes in the lattice parameter are correctly accounted for in the calculations, is raised. Figure 5.10 shows the lattice thermal conductivity of ScNiBi as a function of changes in the lattice parameter for calculations utilizing the complete TDEP method, κ_{TDEP}, and calculations using the force constants of the equilibrium ScNiBi, κ_{VCA}. The latter approach is similar to that used to calculate the thermal conductivity of the half-Heusler alloys. As for the results shown in figure 5.8, κ_{VCA} is quite insensitive to changes in the lattice parameter. κ_{TDEP}, however, varies significantly as the lattice parameter increases or decreases, indicating that the calculations used to find κ_{VCA} does not account correctly for variations in the lattice parameter.

On the other hand, the comparability between κ_{VCA} and κ_{TDEP} may be questionable. The complete TDEP approach used to find κ_{TDEP} artificially strains the lattice of ScNiBi. Consequently, the atoms are forcibly displaced from their equilibrium position, and interatomic forces are created. This non-equilibrium structure forms the basis for the thermal conductivity calculations, and greatly affects the calculations of the second and third order force constants. In the calculation κ_{VCA}, on the other hand, the strained structure is assumed to be at equilibrium such that no interatomic net forces are present. As a result, the two calculations may not be comparable. Nevertheless, for very small changes in the lattice parameter, figure 5.11 shows that the phonon dispersion relations of the strained structures diverge little from that of the equilibrium structure. κ_{TDEP} and κ_{VCA} may therefore be comparable in this range. Since κ_{TDEP} still is more sensitive to changes in the lattice parameter than κ_{VCA}, the results indicate that the changes in the lattice parameter are not correctly accounted for. While this also may be true for the calculations of the thermal conductivity of the $\mathrm{Sc}_x\mathrm{Y}_y\mathrm{La}_{1-x-y}\mathrm{NiBi}$ half-Heusler alloys, the error might be corrected for through the interpolation of the force constants. Since the changes in the lattice parameter affects the force constants, the linear interpolation performed to achieve the force constants of the alloys in the present work, may not be valid. Conclusive testing of the validity of the linear interpolation of the force constants of the alloys is contingent on the existence of reliable results that inherently accounts for changes in the lattice parameter and force constants. Such results may be found through experiments. Another source may be the results of the calculations utilizing the SQS approach, if and when those are available.

6.4 Reducing the lattice thermal conductivity further

6.4.1 Effect of grain size

The cumulative lattice thermal conductivity is given as a function of the mean free path in figure 5.4a, b and c for $\mathrm{Sc}_x\mathrm{La}_{1-x}\mathrm{NiBi}$, $\mathrm{Sc}_x\mathrm{Y}_{1-x}\mathrm{NiBi}$ and $\mathrm{Y}_x\mathrm{La}_{1-x}\mathrm{NiBi}$ at 300 K. Since the cumulative thermal conductivity levels out around mean free paths of 300 nm for all of the binary alloys, the phonons with mean free path less than 300

nm must be scattered in order to reduce the thermal conductivity. In fact, since the phonons with mean free path between 0 and 50 nm contribute most to the thermal conductivity, these are the phonons to scatter for the most efficient reduction of the lattice thermal conductivity.

As discussed in section 2.3.5, the introduction of grains to the bulk materials induces yet another scattering mechanism; the grain boundary scattering. Since phonons with mean free paths comparable to the size of the grain are scattered at the grain boundary, figure 5.4 indicates that the grain sizes in $Sc_xLa_{1-x}NiBi$, $Sc_xY_{1-x}NiBi$ and $Y_xLa_{1-x}NiBi$ should be ranging from 0 to 50 nm in order to reduce the thermal conductivity most. Indeed, the minimum lattice thermal conductivity at 300 K of $Sc_xLa_{1-x}NiBi$ with 50 nm grains is 2.4 W/mK found for $Sc_{0.5}La_{0.5}NiBi$. This is a reduction of 45% compared to that of the bulk binary alloy as illustrated in figure 5.12.

Although the lattice thermal conductivity of LaNiBi decreases significantly upon nanostructuring (with 35%), the thermal conductivity of the nanostructured ScNiBi is reduced with 60%. Thus, the lattice thermal conductivity of the nanostructured ScNiBi becomes comparable to that of the LaNiBi. This confirms the efficiency of the grain boundary scattering. Moreover, it indicates that the grain boundary scattering largely affects the acoustic phonon modes. Consequently, the effect of the grain boundaries is smaller in LaNiBi where anharmonicity already targets the acoustic phonon modes, than in the less anharmonic ScNiBi. This is supported by the shift of the minimum lattice thermal conductivity towards ScNiBi in the nanostructured alloys. If the grain boundary scattering largely affects the acoustic phonon modes, the effect of increasing anharmonicity introduced as Sc is substituted with La is diminished. Thus, the effect of mass-disorder increases, and the minimum lattice thermal conductivity is shifted towards the maximum of the mass-disorder parameter at x=0.8 (see figure 6.1). In other words, the trends in figure 5.12 confirm the hypothesis from section 6.1 that the increasing concentration of La, increases the anharmonicity of the alloy which increases the scattering of the acoustic phonon modes. The contribution from the increased anharmonicity therefore dominates over the contribution from the mass-disorder scattering, which targets the optic phonon modes.

While the presented results indicate a large effect of nanostructuring on the lattice thermal conductivity, introducing nanosized grains may also reduce the electrical conductivity. This is shown for various materials[40]–[44] although a reduction of the grain sizes to a few hundred nanometers has increased the figure of merit from equation 2.4 in several half-Heuslers[45]–[48]. A decrease in the grain size down to 50 nm, however, may affect the electrical conductivity more, and thus result in lower figure of merit than expected. In addition, the synthesis of materials with grain sizes down to 50 nm may be challenging. Even though grain sizes below 100 nm have been reported for other materials using ball milling and spark plasma sintering[49], sizes of 200-300 nm are reported for half-Heuslers using the same methods[45]–[48].

6.4.2 Effect of alloying on the Bi-position

Although the partial isoelectronic substitution on the X-position in XNiBi, X=(Sc, Y or La), reduces the lattice thermal conductivity, the mass-disorder primarily scatters the optic phonon modes as discussed in section 6.1 and 6.4.1. Because scattering of the acoustic phonon modes decreases the thermal conductivity more efficiently than

scattering of the optic, the site of the alloying is important. As the acoustic modes are dominated by Bi for all of the $Sc_xY_yLa_{1-x-y}NiBi$ alloys, alloying on the Bi- (or Z-) position would perhaps decrease the thermal conductivity more efficiently than the substitution on the X-position. Moreover, the phonon DOSes projected on atomic sites in figure 5.2 indicate a general relationship between the mass of an element and the phonon mode it dominates; the acoustic phonon modes are dominated by the heaviest element in the lattice while the lightest dominates the optic. This trend is also seen in other half-Heuslers (such as TiNiSn, ZrNiTi and HfNiSn[50]). Thus, to achieve mass-disorder scattering of the acoustic phonon modes, alloying on the site of the heaviest element of the half-Heusler should be performed. Moreover, for the Z-position elements to remain the dominant contributors to the acoustic phonon modes, the substitute should be heavier than the remaining two elements of the structure. On the other hand, the mass-disorder scattering also depends on the mass-disorder parameter which increases for increasing mass difference. Hence, the choice of substitutes on the Z-position is a balance between the desire to dominate the acoustic phonon modes, and to maximize the mass-disorder parameter.

In the case of the XNiBi, X=(Sc, Y or La), half-Heuslers, two of the elements than may be used for isoelectronic substitution are As and Sb. While both of these are lighter than La and heavier than Sc, only Sb is heavier than Y. On the other hand, the average mass of Bi and As is smaller than the mass of Y only for concentrations of less than 10% Bi. Consequently, the Z-position elements in $YNiBi_xAs_{1-x}$ are expected to either dominate or, in the case of $x < 0.1$, contribute strongly to the acoustic phonon modes. Since the mass-disorder parameter is maximized when Bi is substituted with As, as illustrated in figure 6.2, the lattice thermal conductivity is expected to decrease more for alloying with As than with Sb.

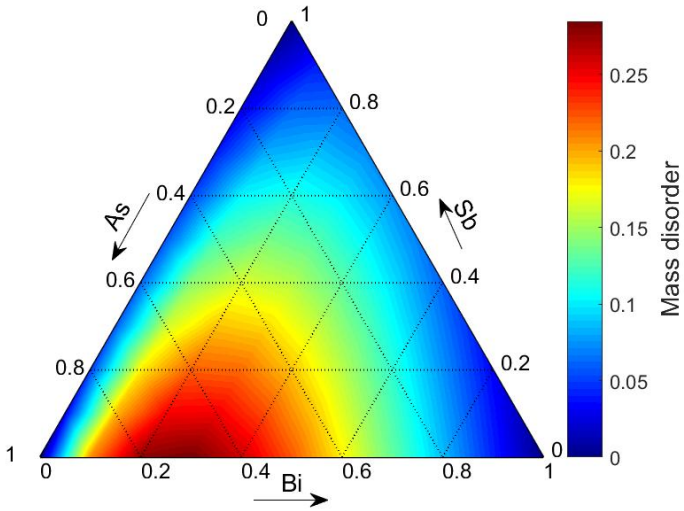

Figure 6.2: Mass-disorder parameter of $YNiBi_{1-x-y}As_xSb_y$. Pure YNiBi, YNiSb and YNiAs is found in the lower right, upper and lower left corner, respectively

Even though the lattice thermal conductivity of neither YNiAs nor YNiSb is cal-

culated in the present work, it may be approximated using the lattice parameter and force constants of YNiBi. In table 6.1, the lattice thermal conductivity using the force constants from the most anharmonic parent, κ_{III}*, shows reasonable agreement with the total lattice thermal conductivity, κ_{I}. On the other hand, since As and Sb are lighter than Bi, the results from the specialization project indicate that the acoustic phonon modes of YNiAs and YNiSb might experience a shift towards higher frequencies. In that case, the acoustic-optic phonon band gap is reduced, and the scattering of the acoustic phonon modes increased. Consequently, YNiAs and YNiSb may be more anharmonic than YNiBi, and the approximation of the lattice thermal conductivity less accurate, as illustrated by the deviations of κ_{III}** from κ_{I} in table 6.1. Nonetheless, an idea of the behaviour of YNiBi when Bi is substituted with As or Sb may be achieved using the lattice parameter and force constants of YNiBi. Thus, estimates of the lattice thermal conductivity of $YNiBi_xAs_{1-x}$ and $YNiBi_xAs_{1-x}$ is given in figure 5.15.

As expected, figure 5.13 showing the site-projected phonon DOS of $YNiBi_xAs_{1-x}$ and $YNiBi_xSb_{1-x}$ indicates that the Z-position elements dominate the acoustic phonon modes. Thus, the mass-disorder efficiently reduces the lattice thermal conductivity to 2.4 W/mK and 3.5 W/mK found for $YNiBi_{0.36}As_{0.64}$ and $YNiBi_{0.38}Sb_{0.62}$, respectively. These compositions correspond with the compositions of each binary exhibiting the highest mass-disorder. Thus, the dominance of the mass-disorder contributions to the lattice thermal conductivity is emphasized.

Moreover, in line with the expectations, the lattice thermal conductivity of $YNiBi_xAs_{1-x}$ is generally lower than that of $YNiBi_xSb_{1-x}$. However, at compositions close to x=0, the lattice thermal conductivity of $YNiBi_xAs_{1-x}$ exceeds that of $YNiBi_xSb_{1-x}$. Since As is lighter than Sb, the acoustic-optic phonon band gap is smaller in YNiAs compared to YNiSb as suggested in figure 5.14. Here, the acoustic and optic phonon modes are increasingly overlapping as x decreases, and overlapping more in $YNiBi_{0.25}As_{0.75}$ than in $YNiBi_{0.25}Sb_{0.75}$. According to the discussion in section 6.1, the lattice thermal conductivity of YNiAs should therefore be smaller than that of YNiSb. Rather than contradicting the hypotheses presented earlier, however, this phenomenon may arise from errors caused by the utilization of the YNiBi lattice parameter and force constants. Similar to $Sc_xLa_{1-x}NiBi$ with LaNiBi force constants, the lattice thermal conductivity as x approaches 0 may be overestimated. On the other hand, the phonon DOSes exhibit less overlap and closer resemblance to those of YNiBi as x goes to 1. Hence, the approximated lattice thermal conductivity of $YNiBi_xAs_{1-x}$ and $YNiBi_xSb_{1-x}$ may be closer to the true value as the compositions approaches YNiBi.

Although the lattice thermal conductivity resulting from alloying on the Bi-position is an estimate, the results presented here indicate a large improvement to the lattice thermal conductivity compared with that of the pure XNiBi, X=(Sc, Y or La), half-Heuslers. On the other hand, there is no work performed on these structures that may verify the presented results. Moreover, even though there are theoretical studies on YNiAs and YNiBi[51], [52] suggesting the stability of these structures, it remains to be seen if stable solid solutions of the $YNiBi_xAs_{1-x}$ and $YNiBi_xSb_{1-x}$ alloys can be achieved experimentally.

6.5 Lattice thermal conductivity compared

In this thesis, three different methods to reduce the lattice thermal conductivity have been investigated; partial substitution on the X-position, nanostructuring of the bulk materials, and partial substitution on the Bi-position. In table 6.2 the minimum lattice thermal conductivity of each method is given in the top three rows. Comparing any of these to the lattice thermal conductivity of the pure ScNiBi, YNiBi and LaNiBi half-Heuslers, immense improvements are achieved. In fact, the reduction is such that the lattice thermal conductivity is comparable with that of $Ti_{0.5}Hf_{0.5}NiSn$ which is one of the best performing thermoelectric half-Heuslers. Moreover, the minimum lattice thermal conductivity of the $YNiBi_xAs_{1-x}$, and nanostructured $Sc_xY_yLa_{1-x-y}NiBi$ alloy is comparable with that of Bi_2Te_3, one of the best commercial thermoelectrica.

Table 6.2: Lattice thermal conductivity at 300 K of selected materials investigated in the present study compared to the lattice thermal conductivity of pure ScNiBi, YNiBi and LaNiBi, in addition to $Ti_{0.5}Hf_{0.5}NiSn$ and Bi_2Te_3

Material	Lattice thermal conductivity (W/mK)	Method	Source
$Sc_{0.5}La_{0.5}NiBi$, 50 nm grains	2.4	RTA - BTE	This work
$YNiBi_{0.36}As_{0.84}$	2.4	RTA -BTE	This work
$Sc_{0.24}La_{0.76}NiBi$	4.3	RTA - BTE	This work
LaNiBi, 50 nm grains	3.8	RTA - BTE	This work
ScNiBi, 50 nm grains	5.0	RTA - BTE	This work
ScNiBi	12.3	RTA - BTE	Specialization project
ScNiBi	14.3	HTC	Carrete et al. [7]
YNiBi	8.9	RTA - BTE	Specialization project
YNiBi	10.6	HTC	Carrete et al. [7]
LaNiBi	5.8	RTA - BTE	Specialization project
$Ti_{0.5}Hf_{0.5}NiSn$	3.2	RTA - BTE	Eliassen et al. [50]
Bi_2Te_3	1.38	ZR	Goldsmid [53]

RTA - BTE: Relaxation time approximation - Boltzmann equation

HTC: High-throughput computations

ZR: Zone refining

Interestingly, the present work indicate that the alloying on the Bi-position reduces the lattice thermal conductivity as much as the nanostructuring of $Sc_xLa_{1-x}NiBi$. However, the lattice thermal conductivity resulting from alloying on the Bi-positions are estimates, and may be associated with large errors. On the other hand, indications are that the values are overestimated. If that is the case, the alloying on the Bi-position outperform the nanostructuring. In addition, this method may not as susceptible to influencing the electronic structure as the nanostructuring. However, the nanostructuring is more flexible, and may be applied efficiently over a range of compositions. Thus, as a method to reduce the lattice thermal conductivity it holds an advantage over the method utilizing alloying on the Bi-position.

6.6 Evaluation of the simulation methods

The calculations performed in the present work are based on the density functional theory (DFT) calculations performed in VASP in the specialization project (see Appendix A). As discussed briefly in section 3.1.5, the approximated exchange-correlation functional utilized in the DFT calculations may introduce physical inaccuracies in the calculated forces. Although the functional used for the DFT calculations of the pure XNiBi, X=(Sc, Y or La), is the PBEsol functional, which includes some empirical parameters to ensure higher physical accuracy, the lack of experimental work on the XNiBi, X=(Sc, Y or La), based materials makes the evaluation of the DFT simulations difficult. Moreover, there are other parameters that may influence both the physical and numerical accuracy of the DFT calculations. If, for example, the pseudopotentials utilized do not match the physical properties of the materials under inspection, large errors may be introduced. Standard pseudopotentials recommended in VASP are used for the Sc, Y, La, Ni and Bi elements in the DFT calculations. However, the impact of the choice of pseudopotentials is not investigated neither in this nor the previous project. Particularly f-block elements may not be handled well in the VASP pseudopotentials. Thus, the potential used for the f-block element, La, may be susceptible to self-interaction errors[31]. Again, such errors may be difficult to detect due to the lack of experimental work.

On the other hand, table 6.2 shows that the obtained lattice thermal conductivity of ScNiBi and YNiBi from the specialization project are in good agreement with the anharmonic lattice thermal conductivity estimated by Carrete and co-workers[7]. Although the values reported by Carrete et al. also are found through DFT calculations, and may be susceptible to similar errors as those of the present work, a different method based on high-throughput computations is used. The agreement between the results presented by Carrete et al. and those presented here may therefore suggest that the calculations performed in this thesis are relatively robust with respect to the simulation method. Consequnetly, they accuracy may be relatively good.

Even if the DFT calculations are accurate for the pure half-Heusler, ScNiBi, YNiBi and LaNiBi, the VCA approach utilized in this study may introduce errors to the calculations of the $Sc_xY_yLa_{1-x-y}NiBi$, $YNiNiBi_xAs_{1-x}$ and $YNiBi_xSb_{1-x}$ alloys. These errors arise from the implicit substitution enforced by the VCA approach. Consequently, it does not mimic the alloying of real materials, where the substitution is random. Particularly if the forces introduced to the lattice by the different substitutes are very different from each other, the VCA approach may yield erroneous results. This is because the changes in the forces around the individual positions where alloying occurs are ignored in the VCA as discussed in section 3.3.5. These potential errors are difficult to assess. Table 6.1 shows relatively small deviations for κ_{III}* (lattice thermal conductivity with force constants from the most anharmonic parent) compared to the total lattice thermal conductivity, κ_{I}. Thus, the force constants of, for example, LaNiBi may estimate the lattice thermal conductivity of ScNiBi. This may indicate that the local environments are relatively constant throughout the alloys such that the VCA approach may be applied. On the other hand, the deviations for κ_{III}** (lattice thermal conductivity with force constants from the least anharmonic parent) compared to the total lattice thermal conductivity, κ_{I}, are large. Consequently, larger variations in the local environments are indicated, and the VCA may not be valid. Furthermore, there might be errors associated with the interpolation of the force constants,

as discussed in section 6.2. Even though a comparison with experimental results are required to conclude on the validity of the VCA approach, results utilizing the SQS approach may also indicate whether the VCA is a good approximation or not. This is because the SQS approach enforces explicit alloying, and calculates the forces directly using DFT. Thus, the challenges concerning the variations of local environments and the interpolation of the force constants are omitted.

6.7 Further work

The present work provides information on the effect of anharmonic, mass-disorder and grain boundary scattering on the lattice thermal conductivity of the $Sc_xY_yLa_{1-x-y}NiBi$ half-Heusler alloys. However, the enhanced effect of alloying on the Bi-position was merely indicated by this thesis. The calculations performed here were estimates based on the lattice parameter and force constants of YNiBi, and the accuracy of these calculations remains unknown. Consequently, a full calculation of the effect of isoelectronic substitution of Bi with As or Sb should be performed.

Furthermore, the effect of grain boundary scattering was only investigated in the $Sc_xY_yLa_{1-x-y}NiBi$ alloys. It would be interesting to explore this effect in the $YNiNiBi_xAs_{1-x}$ and $YNiBi_xSb_{1-x}$ alloys to see if grains of reasonable size may target the remaining acoustic phonon modes, and reduce the lattice thermal conductivity. Herein lies another unanswered question; the sensitivity of the grain boundary scattering to grain size. As discussed previously, it may be challenging to synthesize materials with grains as small as 50 nm. Thus, it is important to investigate whether the same, or similar, effects on the lattice thermal conductivity may be achieved for larger grain sizes.

In addition, most of the calculations performed in this thesis use the VCA approach. While this approach is computationally inexpensive and easily applied with the TDEP method, it is inherently erroneous as it enforces implicit rather than explicit substitution. Results closer to the real materials are therefore expected when introducing the substitutes explicitly to the lattice using the SQS approach. Consequently, comparing results from calculations using the VCA and the SQS approach may yield information on whether the local environment changes throughout the alloys, in which case the results from the VCA should deviate from those of the SQS approach. Moreover, the relationship between the force constants and the lattice parameter may be investigated further. Thus, the question of whether the linear interpolation of the force constants in the VCA approach is valid, may be answered.

Due to the lack of experimental results on the XNiBi, X=(Sc, Y or La), based materials, the overall physical accuracy of teh presented calculations remains unknown. Rigorous testing of the impact of a number of DFT parameters, such as the exchange-correlation functional and the pseudopotential, may indicate if there are large errors associated with the calculations depending on the parameters utilized. However, experimental work on the materials under investigation is required for a conclusive assessment of the physical accuracy the presented calculations.

Chapter 7

Conclusion

The aim of this thesis was to study multiple contributions to the thermal properties of XNiBi, X=(Sc, Y or La), based half-Heuslers. Mass disorder was introduced to the materials through isoelectronic substitution with Sc, Y or La on the X-position, and with As or Sb on the Bi-position. The resulting alloys, $Sc_xY_yLa_{1-x-y}NiBi$, $YNiNiBi_xAs_{1-x}$ and $YNiBi_xSb_{1-x}$, were represented within the virtual crystal approximation (VCA). Although this representation does not capture the local environments of the real alloys, it retains the full symmetry of the parent half-Heusler. Thus, finite temperature calculations of the thermal properties could be performed using density functional theory (DFT) together with the temperature dependent effective potential (TDEP) method. The lattice thermal conductivity of the $Sc_xY_yLa_{1-x-y}NiBi$, $YNiNiBi_xAs_{1-x}$ and $YNiBi_xSb_{1-x}$ half-Heusler alloys was found by solving the Boltzmann transport equation (BTE) within the relaxation time approximation (RTA). The additional effect of nanostructuring, introduced to the $Sc_xY_yLa_{1-x-y}NiBi$ half-Heusler alloys by means of 50 nm grains, was also investigated.

The effect of alloying in the XNiBi, X=(Sc, Y or La), based half-Heuslers was found to depend on the site of alloying. The introduction of heavier elements on the X-position of ScNiBi and YNiBi decreases the acoustic-optic phonon band gap, and thus increases the anharmonic scattering of the acoustic phonon modes of the resulting alloys. The increased anharmonicity combined with the mass-disorder on the X-position reduces the lattice thermal conductivity to a minimum lattice thermal conductivity of 4.3 W/mK found for $Sc_{0.24}La_{0.76}NiBi$. This is comparable with the smallest lattice thermal conductivity of the $Ti_xHf_{1-x}NiSn$ half-Heusler alloys. However, the site-projected phonon DOS reveals that the alloying of the X-position mainly introduces scattering of the optic phonon modes. Since the optic phonon modes contribute less to the lattice thermal conductivity than the acoustic modes, the reduction in the lattice thermal conductivity of $Sc_{0.24}La_{0.76}NiBi$ is largely ascribed to the increased anharmonicity rather than the increased mass-disorder as La substitutes Sc. In contrast, alloying on the Bi-position with As or Sb affects the acoustic phonon modes since these modes are dominated by Bi in the XNiBi, X=(Sc, Y or La), half-Heuslers. Consequently, the mass-disorder on the Bi-position efficiently reduces the lattice thermal conductivity to 2.4 W/mK and 3.5 W/mK for $YNiBi_{0.36}As_{0.64}$ and $YNiBi_{0.38}As_{0.62}$, respectively. The minimum lattice thermal conductivity of $YNiNiBi_xAs_{1-x}$ and $YNiBi_xSb_{1-x}$ is comparable to, and even lower than, the smallest lattice thermal conductivity of the $Ti_xHf_{1-x}NiSn$ half-Heusler alloys.

Moreover, it is comparable to that of the commercial bismuth tellurides.

Even though the introduction of mass-disorder, particularly on the Bi-position, reduces the lattice thermal conductivity of the half-Heusler alloys considerably, nanostructuring was found to scatter the acoustic phonon modes more efficiently over a range of compositions. In the pure half-Heusler, ScNiBi, the introduction of nanoscaled grains reduces the lattice thermal conductivity from 12.3 W/mK in the bulk material to 5.0 W/mK in the nanostructured. This is the largest single reduction found in the presented work. However, combining nanostructuring with alloying reduces the lattice thermal conductivity further. In $Sc_xLa_{1-x}NiBi$, the lattice thermal conductivity was reduced with 45% compared to the bulk $Sc_xLa_{1-x}NiBi$ alloys, and reached a minimum at 2.4 W/mK in $Sc_{0.5}La_{0.5}NiBi$. As for the alloying on the Bi-position, the lattice thermal conductivity resuting from the nanostructuring is comparable to that of the commercial bismuth tellurides.

The present work indicates that the lattice thermal conductivity of XNiBi, X=(Sc, Y or La), based half-Heuslers may be reduced sufficiently through nanostructuring and alloying on the Bi-position to be competitive with state-of-the-art thermoelectric materials. Moreover, the understanding of how different mechanisms influence the lattice thermal conductivity achieved in this thesis may be applied to other materials. Thus, the ability to predict the potential of unexplored materials within thermoelectric applications may increase, and aid the continued progress of the performance of thermoelectric devices.

Bibliography

[1] U. E. P. Agency. (2014). Global greenhous gas emissions data, [Online]. Available: https://www.epa.gov/ghgemissions/global-greenhouse-gas-emissions-data.

[2] I. Johnson, W. T. Choate, and A. Davidson, "Waste heat recovery. Technology and opportunities in US industry," BCS, Inc., Laurel, MD (United States), Tech. Rep., 2008.

[3] A. I. Kalina *et al.*, "Combined cycle system with novel bottoming cycle," *ASME J. Eng. Gas Turbines Power*, vol. 106, no. 4, pp. 737–742, 1984.

[4] W. Liu, Q. Jie, H. S. Kim, and Z. Ren, "Current progress and future challenges in thermoelectric power generation: From materials to devices," *Acta Mater.*, vol. 87, pp. 357–376, 2015.

[5] Fitriani, R. Ovik, B. Long, M. Barma, M. Riaz, M. Sabri, S. Said, and R. Saidur, "A review on nanostructures of high-temperature thermoelectric materials for waste heat recovery," *Renew Sust Energ Rev*, vol. 64, pp. 635–659, 2016.

[6] S. Chen and Z. Ren, "Recent progress of half-heusler for moderate temperature thermoelectric applications," *Mater Today*, vol. 16, no. 10, pp. 387–395, 2013.

[7] J. Carrete, W. Li, N. Mingo, S. Wang, and S. Curtarolo, "Finding unprecedentedly low-thermal-conductivity half-heusler semiconductors via high-throughput materials modeling," *Phys. Rev. X*, vol. 4, p. 011 019, 1 Feb. 2014.

[8] C. Fu, S. Bai, Y. Liu, Y. Tang, L. Chen, X. Zhao, and T. Zhu, "Realizing high figure of merit in heavy-band p-type half-Heusler thermoelectric materials," *Nat. Commun.*, vol. 6, 2015.

[9] S.-W. Kim, Y. Kimura, and Y. Mishima, "High temperature thermoelectric properties of TiNiSn-based half-Heusler compounds," *Intermetallics*, vol. 15, no. 3, pp. 349–356, 2007.

[10] T. J. Seebeck, "Ueber die magnetische polarisation der metalle und erze durch temperatur-differenz," *Ann Phys*, vol. 82, no. 2, pp. 133–160, 1826.

[11] A. da Rosa, "Chapter 5 - Thermoelectricity," in *Fundamentals of Renewable Energy Processes (Third Edition)*, A. d. Rosa, Ed., Third Edition, Boston: Academic Press, 2013, pp. 149–212.

[12] G. J. Snyder and E. S. Toberer, "Complex thermoelectric materials," *Nat. Mater.*, vol. 7, pp. 105–114, 2008.

[13] A. Minnich, M. Dresselhaus, Z. Ren, and G. Chen, "Bulk nanostructured thermoelectric materials: Current research and future prospects," *Energy Environ. Sci.*, vol. 2, no. 5, pp. 466–479, 2009.

[14] T. Graf, C. Felser, and S. S. Parkin, "Simple rules for the understanding of heusler compounds," *Prog Solid State Ch*, vol. 39, no. 1, pp. 1–50, 2011.

[15] W. Xie, A. Weidenkaff, X. Tang, Q. Zhang, J. Poon, and T. M. Tritt, "Recent advances in nanostructured thermoelectric half-Heusler compounds," *Nanomaterials*, vol. 2, no. 4, pp. 379–412, 2012.

[16] N. Shulumba, "Vibrations in solids: From first principles lattice dynamics to high temperature phase stability," PhD thesis, Linköping University Electronic Press, 2015.

[17] M. T. Dove, *Structure and dynamics: An atomic view of materials*. Oxford University Press, 2003, vol. 1.

[18] C. Kittel, *Introduction to solid state*, 8th. John Wiley & Sons, 2005.

[19] S. L. Shindé and J. S. Goela, *High thermal conductivity materials*. Springer Science + Business Media, 2006.

[20] G. P. Srivastava, *The physics of phonons*. CRC press, 1990.

[21] W. Kim, S. L. Singer, and A. Majumdar, "Tuning thermal transport in crystalline solids using embedded nanoparticles," *J Phys Ser*, vol. 92, no. 1, p. 012 085, 2007.

[22] M. Dresselhaus, G. Chen, M. Tang, R. Yang, H. Lee, D. Wang, Z. Ren, J.-P. Fleurial, and P. Gogna, "New directions for low-dimensional thermoelectric materials," *Adv Mat*, vol. 19, no. 8, pp. 1043–1053, 2007.

[23] O. Hellman. (2016). Temperature dependent effective potential 1.0, [Online]. Available: `http://ollehellman.github.io/index.html`.

[24] B. Fultz, "Vibrational thermodynamics of materials," *Prog. Mater Sci.*, vol. 55, no. 4, pp. 247–352, 2010.

[25] D. S. Sholl and J. A. Steckel, *Density Functional Theory*. Wiley, 2009.

[26] A. G. Rebaza, V. I. Fernández, L. T. Eleno, L. Errico, C. G. Schön, and H. M. Petrilli, "Influence of the exchange-correlation functional on the energy of formation and magnetic behavior of binary D03 intermetallic compounds FeM3 (M= Ti, Zr, Hf)," *J. Phase Equilib. Diff.*, pp. 1–7, 2017.

[27] G. Kresse and J. Hafner, "*Ab initio* molecular dynamics for liquid metals," *Phys. Rev. B*, vol. 47, pp. 558–561, 1 Jan. 1993.

[28] G. Kresse and J. Furthmüller, "Efficiency of ab-initio total energy calculations for metals and semiconductors using a plane-wave basis set," *Comp Mater Sci*, vol. 6, no. 1, pp. 15–50, 1996.

[29] G. Kresse and J. Furthmüller, "Efficient iterative schemes for *ab initio* total-energy calculations using a plane-wave basis set," *Phys. Rev. B*, vol. 54, pp. 11 169–11 186, 16 Oct. 1996.

[30] G. Kresse and D. Joubert, "From ultrasoft pseudopotentials to the projector augmented-wave method," *Phys. Rev. B*, vol. 59, pp. 1758–1775, 3 Jan. 1999.

[31] G. Kresse, M. Marsman, and J. Furthmüller. (2016). Vasp the guide, [Online]. Available: `http://cms.mpi.univie.ac.at/vasp/vasp/vasp.html`.

[32] O. Hellman, I. A. Abrikosov, and S. I. Simak, "Lattice dynamics of anharmonic solids from first principles," *Phys. Rev. B*, vol. 84, p. 180 301, 18 Nov. 2011.

[33] O. Hellman, P. Steneteg, I. A. Abrikosov, and S. I. Simak, "Temperature dependent effective potential method for accurate free energy calculations of solids," *Phys. Rev. B*, vol. 87, p. 104 111, 10 Mar. 2013.

[34] O. Hellman and I. A. Abrikosov, "Temperature-dependent effective third-order interatomic force constants from first principles," *Phys. Rev. B*, vol. 88, p. 144 301, 14 Oct. 2013.

[35] B. Abeles, "Lattice thermal conductivity of disordered semiconductor alloys at high temperatures," *Phys. Rev.*, vol. 131, pp. 1906–1911, 5 Sep. 1963.

[36] N. J. Ramer and A. M. Rappe, "Application of a new virtual crystal approach for the study of disordered perovskites," *J. Phys. Chem. Solids*, vol. 61, no. 2, pp. 315–320, 2000.

[37] C. Chen, E. G. Wang, Y. M. Gu, D. M. Bylander, and L. Kleinman, "Unexpected band-gap collapse in quaternary alloys at the group-III-nitride/GaAs interface: GaAlAsN," *Phys. Rev. B*, vol. 57, pp. 3753–3756, 7 Feb. 1998.

[38] J. M. Larkin and A. J. McGaughey, "Predicting alloy vibrational mode properties using lattice dynamics calculations, molecular dynamics simulations, and the virtual crystal approximation," *J. Appl. Phys.*, vol. 114, no. 2, p. 023 507, 2013.

[39] A. Zunger, S.-H. Wei, L. G. Ferreira, and J. E. Bernard, "Special quasirandom structures," *Phys. Rev. Lett.*, vol. 65, pp. 353–356, 3 Jul. 1990.

[40] S. Bandyopadhyay and A. Pal, "The effect of grain boundary scattering on the electron transport of aluminium films," *J. Phys. D: Appl. Phys.*, vol. 12, no. 6, p. 953, 1979.

[41] M. I. Mohammed, A. Elbadawi, and H. Abuellhassan, "Temperature and grain size effect on the electrical conductivity of," *J. App. Ind. Sciences*, vol. 1, no. 3, pp. 12–22, 2013.

[42] Q. Zhang, X. Zhang, B. Cao, M. Fujii, K. Takahashi, and T. Ikuta, "Influence of grain boundary scattering on the electrical properties of platinum nanofilms," *App. Phys. Lett.*, vol. 89, no. 11, p. 114 102, 2006.

[43] Q. Zhang, B. Cao, X. Zhang, M. Fujii, and K. Takahashi, "Influence of grain boundary scattering on the electrical and thermal conductivities of polycrystalline gold nanofilms," *Phys. Rev. B*, vol. 74, no. 13, p. 134 109, 2006.

[44] H. Marom, M. Ritterband, and M. Eizenberg, "The contribution of grain boundary scattering versus surface scattering to the resistivity of thin polycrystalline films," *Thin Solid Films*, vol. 510, no. 1, pp. 62–67, 2006.

[45] S. Bhattacharya, T. M. Tritt, Y. Xia, V. Ponnambalam, S. J. Poon, and N. Thadhani, "Grain structure effects on the lattice thermal conductivity of Ti-based half-Heusler alloys," *Appl Phy Lett*, vol. 81, no. 1, pp. 43–45, 2002.

[46] G. Joshi, X. Yan, H. Wang, W. Liu, G. Chen, and Z. Ren, "Enhancement in thermoelectric figure-of-merit of an n-type half-heusler compound by the nanocomposite approach," *Adv. Energy Mater.*, vol. 1, no. 4, pp. 643–647, 2011.

[47] X. Yan, G. Joshi, W. Liu, Y. Lan, H. Wang, S. Lee, J. Simonson, S. Poon, T. Tritt, G. Chen, *et al.*, "Enhanced thermoelectric figure of merit of p-type half-heuslers," *Nano Lett.*, vol. 11, no. 2, pp. 556–560, 2010.

[48] M. Mikami, A. Matsumoto, and K. Kobayashi, "Synthesis and thermoelectric properties of microstructural heusler fe 2 val alloy," *J. Alloys Compd.*, vol. 461, no. 1, pp. 423–426, 2008.

[49] N. Shkodich, A. Rogachev, S. Vadchenko, D. Moskovskikh, N. Sachkova, S. Rouvimov, and A. Mukasyan, "Bulk Cu–Cr nanocomposites by high-energy ball milling and spark plasma sintering," *J. Alloys Compd.*, vol. 617, pp. 39–46, 2014.

[50] S. N. H. Eliassen, A. Katre, G. K. H. Madsen, C. Persson, O. M. Løvvik, and K. Berland, "Lattice thermal conductivity of $Ti_xZr_yHf_{1-x-y}NiSn$ half-heusler alloys calculated from first principles: Key role of nature of phonon modes," *Phys. Rev. B*, vol. 95, p. 045 202, 4 Jan. 2017.

[51] H. C. Kandpal, C. Felser, and R. Seshadri, "Covalent bonding and the nature of band gaps in some half-heusler compounds," *J. Phys. D: Appl. Phys.*, vol. 39, no. 5, p. 776, 2006.

[52] P. Larson, S. Mahanti, S. Sportouch, and M. Kanatzidis, "Electronic structure of rare-earth nickel pnictides: Narrow-gap thermoelectric materials," *Phys. Rev. B*, vol. 59, no. 24, p. 15 660, 1999.

[53] H. Goldsmid, "The thermal conductivity of bismuth telluride," *P Phys Soc B*, vol. 69, no. 2, p. 203, 1956.

Appendix A

Specialization project

In the following, a summary of the specialization project, *DFT simulations of phonon propagation in the thermoelectric half-Heusler XNiBi (X = Sc, Y or La)*, performed by the author in the fall of 2016 is given. The results from the DFT and TDEP calculations are relevant for the calculations performed in this thesis.

A.1 Methods

The thermal properties of XNiBi, X=(Sc, Y or La), was calculated using the temperature dependent effective potential (TDEP) method together with the Vienna *Ab initio* Simulation Package (VASP). The PBEsol functional was used in all of the thermal property calculations, and the pseudopotential was build from standard, recommended PAW pseudopotentials in VASP; Sc_sv, Y_sv, La, Ni and Bi_d. Convergence of the VASP force calculations was found to be within 1meV for an energy cutoff of 500 eV and a k-point density of 8 in each lattice direction for the primitive half-Heusler lattice. Thus, relaxation of the primitive lattices of XNiBi, X=(Sc, Y or La), was performed using the converged energy cutoff and k-point density. The molecular dynamics calculations were performed with VASP on 3x3x3 supercells with cutoff energy of 500 eV and k-point density of 1. The second and third order force constants were calculated from the pairs of forces and displacements using a second order cutoff radius of 7 Å, and a third order cutoff radius of 6 Å. Based on the low-accuracy force constants and a Monte Carlo routine, 100 structures with size 3x3x3 and representative displacements of the atoms were generated. High-accuracy force calculations were performed on each of these structures using a k-point density of 2 in each lattice direction and an energy cutoff of 500 eV. The force constants were calculated using the same cutoff radii as before. From the high-accuracy force constants, the thermal conductivity was calculated using four q-point meshes with 29, 31, 33 and 35 q-points in each lattice direction, and the tetrahedron integration over the q-point mesh. The thermal conductivity was then extrapolated using a least square method such that the thermal conductivity at q-point distance equal 0 was found.

A.2 Results

Figures A.1a-f) show the dispersion relations and group velocities of ScNiBi, YNiBi and LaNiBi. The acoustic, longitudinal optic and transverse optic phonon modes are indicated with the red, purple and blue colour in all plots. The phonon dispersion relations show that there is no direct overlap between the three groups of phonon modes in any of the materials. A phonon can therefore not transition between different modes without addition of momentum to the phonon. Moreover, the shape of the phonon modes in the three different materials is similar. This observation is confirmed by the group velocities shown in figure A.1b, d and f, where the group velocity of the different modes are of similar shapes and magnitudes in all of the three materials. Also note that the acoustic phonon modes dominate the group velocity of the materials, and its group velocity is of similar magnitude regardless of the material.

Although the dispersion relations in figure A.1a, c and d were not overlapping directly, the phonon DOS of ScNiBi, YNiBi and LaNiBi shows that the optic phonon modes, shown in figures A.2b, d and f, shift towards lower frequencies as Sc is substituted with Y and La. Eventually, in LaNiBi, the acoustic-optic phonon band gap is closed. the shift of the optic rather than the acoustic phonon modes may be explained by the phonon DOS projected on the atomic sites given in figures A.2b, d and f. For all three materials, the acoustic phonon modes are dominated by bismuth. Moreover, there is a trend of increasing bismuth contribution to the optic phonon modes from ScNiBi to LaNiBi. The contributions from the X-position element and nickel, however, differ between the materials. While nickel contributes most to the longitudinal and the X-position element most to the transverse optic modes in ScNiBi and LaNiBi, their contributions are similar to both longitudinal and transverse optic modes in YNiBi.

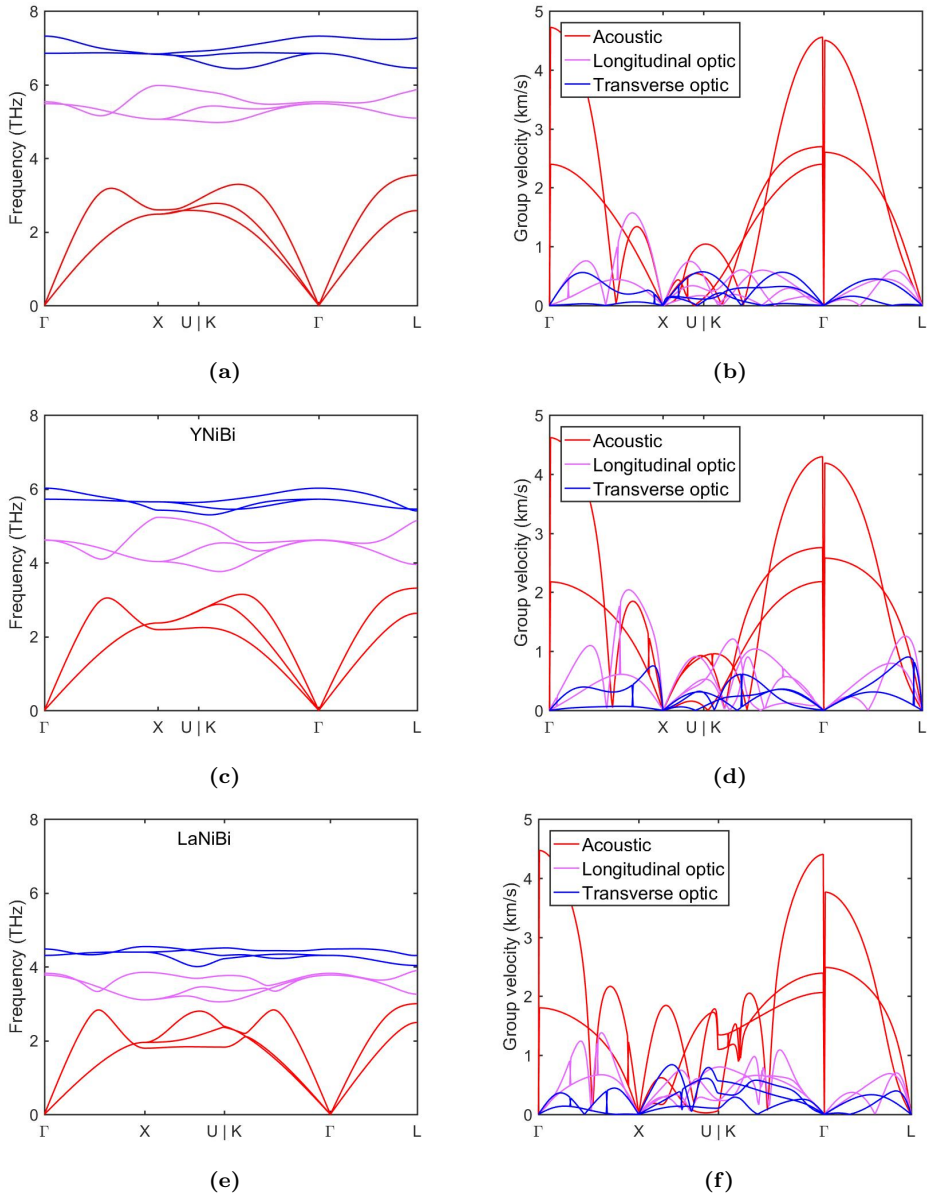

Figure A.1: The phonon dispersion relation and group velocity of a) and b) ScNiBi, c) and d) YNiBi, and e) and f) LaNiBi. The red colour corresponds to acoustic, the purple to longitudinal optic and the blue to transverse optic phonon modes

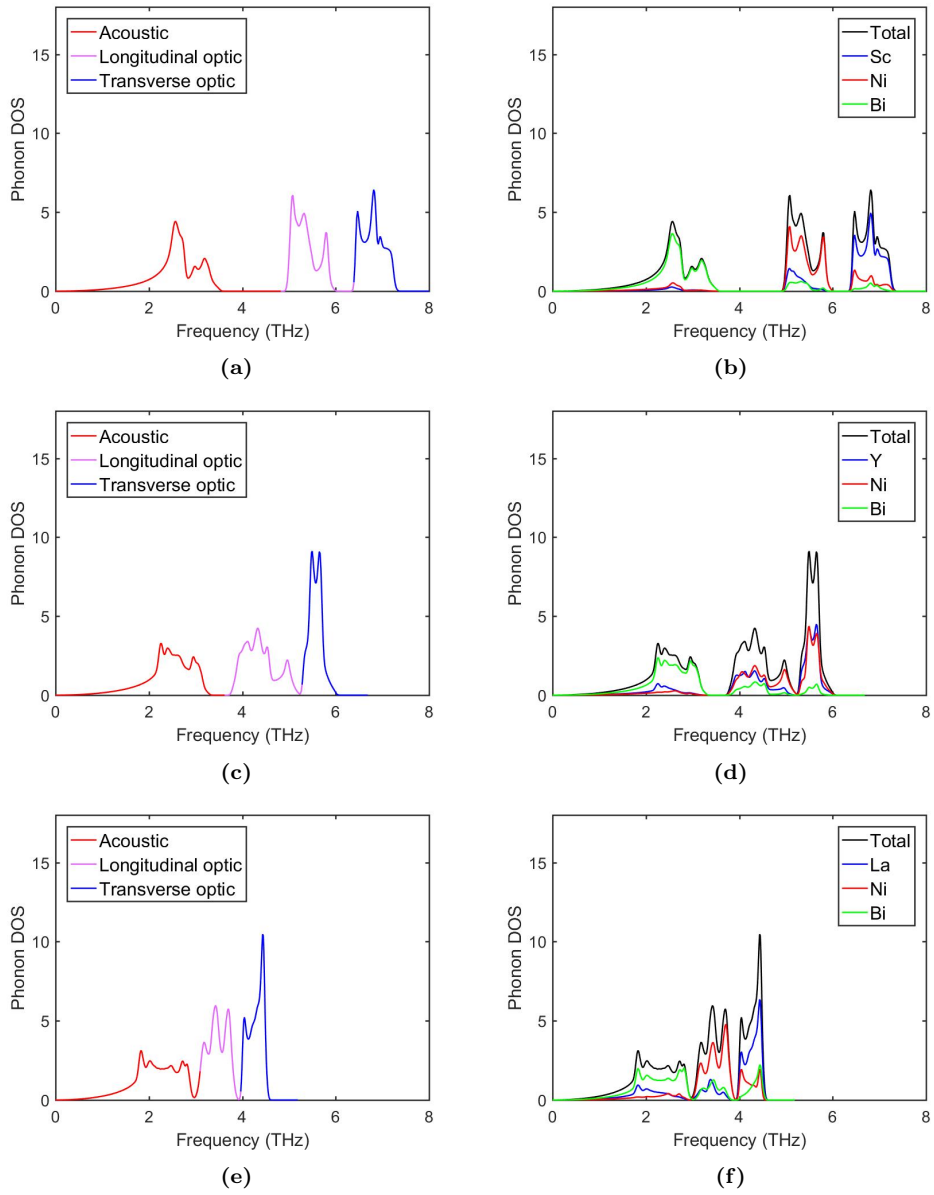

Figure A.2: The phonon DOS projected on the phonon modes and atomic sites of a) and b) ScNiBi, c) and d) YNiBi, and e) and f) LaNiBi. The red colour corresponds to acoustic, the purple to longitudinal optic and the blue to transverse optic phonon modes

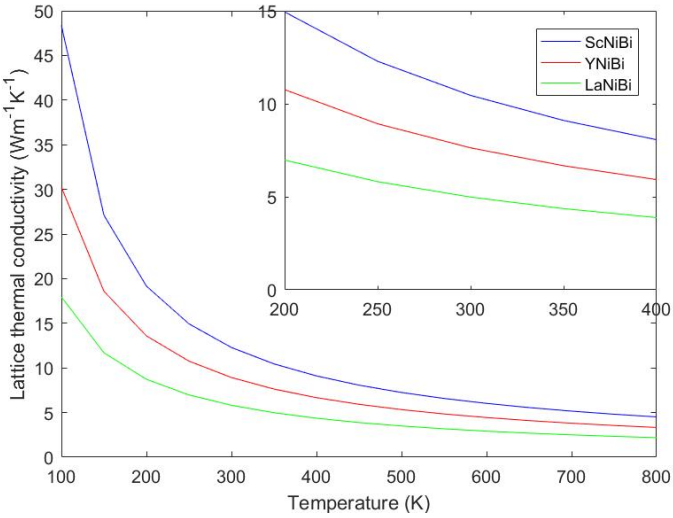

Figure A.3: The lattice thermal conductivity of ScNiBi (in blue), YNiBi (in red) and LaNiBi (in green) as a function of temperature. The inset shows the thermal conductivity zoomed in around 300 K

Figure A.3 shows the lattice thermal conductivity as a function of temperature for ScNiBi, YNiBi and LaNiBi, respectively.The inset in the figure shows the lattice thermal conductivity zoomed in around 300 K. At 300 K the thermal conductivity of ScNiBi, YNiBi and LaNiBi is 12.3, 8.9 and 5.8 W/mK, respectively.

A.3 Conclusion

The phonon dispersion relations of the XNiBi (X = Sc, Y or La) materials exhibit a shift in the phonon modes towards lower frequencies as the X-position element is substituted with a heavier element. Since the optic phonon modes have higher contributions from the X-position elements than the acoustic phonon modes, the shift is larger in the optic modes. As a result, the acoustic-optic frequency band gap decreases from ScNiBi to LaNiBi. Simultaneously, the group velocity of the different materials remains similar. This indicates that the reduction in the calculated thermal conductivity from ScNiBi to LaNiBi is caused by the increasing phonon-phonon scattering as the acoustic-optic frequency band gap decreases.

Appendix B

VASP

In this appendix, technical details of VASP input files are given. The first section of the appendix is intended to give a general overview of the structure of the input files. In the following sections, specifications of the VASP input files used in this project are given.

B.1 Structure and specifications of VASP input files

As mentioned in section 3.1.6 there are four vital input files to VASP: the INCAR, POSCAR, KPOINTS and POTCAR files.

B.1.1 INCAR parameters

The INCAR file contains the input parameters defining how a calculation should be performed. Listing B.1 shows the parameters of a general VASP calculation.

Listing B.1: INCAR file showing the most important general input parameters

```
! Electronic convergence loop
NELMIN = 4          ! Minimum # of electronic steps
ENCUT  = 500        ! Cutoff energy
LREAL  = .FALSE.    ! Projection in reciprocal space
ISMEAR = 0          ! Gaussian smearing of partial occupancies
SIGMA  = 0.02       ! Smearing width
ISPIN  = 1          ! No spin polarization

! XC-functional
GGA = PS

! Ionic relaxation
EDIFFG = -0.001   ! Tolerance for ions
```

- NELMIN Defines the minimum number of electronic steps in each electronic convergence loop

- ENCUT Defines the cutoff energy
- ISMEAR Determines how the partial occupancies are set for each orbital. ISMEAR = 0 gives Gaussian smearing.
- SIGMA Defines the smearing width in eV
- ISPIN Determines whether spin polarized calculations are performed. ISPIN = 1 gives non-spin polarized calculations
- GGA Determines the specific GGA functional used. GGA = PS defines the PBEsol functional

To do relaxations, some extra parameters are required. These are shown in listing B.2.

Listing B.2: INCAR file showing the most important extra input parameters for relaxations

```
! Electronic convergence loop
EDIFF  = 1E-5       ! Accuracy for electronic groundstate
PREC = Accurate     ! Low/Normal/Accurate
LREAL  = .FALSE.    ! Projection in real space

! Ionic relaxation
EDIFFG = -0.001      ! Tolerance for ions
NSW    = 80         ! Max # of ionic steps
IBRION = 1          ! Algorithm for ions. 0: MD 1: QN/DIIS 2: CG
ISIF   = 3          ! Relaxation. 2: ions 3: ions+cell
```

- EDIFF Defines the convergence criterion of the electronic convergence loop
- PREC Determines the accuracy of the calculation. VASP automatically optimizes other parameters, such as the energy cutoff (if not specified already in the INCAR file) and the convergence of the stress tensor, according to the specified level of precision. For PREC = Accurate, high precision calculations are performed
- LREAL Determines whether the projection operators are evaluated in real or reciprocal space. The cost of real space evaluation increases with supercell size, but yields higher accuracy. The reciprocal space evaluation gives less accurate results, but is independent of supercell size
- EDIFFG Defines the convergence criterion for the ionic convergence loop
- NSW Defines the maximum number of ionic steps
- IBRION Determines how the ions are updated and moved. For IBRION = 1, the ions are relaxed into their instantaneous ground state using a quasi-Newton algorithm
- ISIF Determines whether the stress tensor is calculated. This affects how the cell shape and volume are changing. For ISIF = 3, the ions are relaxed, and both the cell volume and shape may change

For molecular dynamics calculations, however, there are other more important parameters as defined in the following listing.

Listing B.3: INCAR file showing the most important extra input parameters for molecular dynamics

```
! Electronic relaxation
ALGO   = Fast     ! Algorithm for electronic relaxation
EDIFF  = 1E-4     ! Accuracy for electronic groundstate
PREC   = Low      ! Precision of calculation
LREAL  = Auto     ! Projection in reciprocal space

! Ionic relaxation
IBRION = 0        ! MD calculations
NSW    = 1500     ! Number of MD steps
POTIM  = 1.0      ! Time per step (fs)
TEBEG  = 300      ! Start temperature
TEEND  = 300      ! Start temperature
SMASS  = 0        ! MD in microcanonical ensemble
ISIF    = 2       ! Relax ions, not cell
```

- ALGO Determines the algorithm by which the electrons are relaxed. For ALGO = Fast, a mixture of the blocked Davidson and the RMM-DIIS scheme is used
- POTIM Defines the time between the MD steps in femtoseconds (fs)
- TEBEG Defines the temperature at the beginning
- TEEND Defines the temperature at the end
- SMASS Determines the velocities of the ions. For SMASS = 0, a canonical ensemble is used

Lastly, the essential INCAR-tags for high precision calculations are defined in listing B.4

Listing B.4: INCAR file showing the most important extra input parameters for high accuracy calculations

```
! Electronic convergence loop
ALGO   = Fast     ! Algorithm for electronic relaxation
EDIFF  = 1E-6     ! Accuracy for electronic groundstate
PREC   = High     ! Precision of the calculation

! Ionic relaxation
NSW    = 0        ! No ionic relaxation
ISIF    = 2       ! Relax ions, not cell
```

B.1.2 POSCAR structure

The POSCAR file contains all information about the geometry and composition of the supercell. Listing B.5 shows an example of a POSCAR for the primitive half-Heusler

structure. The first line is a comment line, naming the system. The next line defines the scaling factor for the Cartesian vectors spanning the supercell, which are defined in the three following lines. In the sixth and seventh line, the atomic species and the number of each species comprising the supercell are given. It is important that the order of the atomic species equals the order of the elemental pseudopotentials of the respective species in the POTCAR file. The eight line specifies whether the atomic positions are given in fractional or Cartesian coordinates, where *Direct* defines fractional atomic coordinates. The remaining lines provides the atomic coordinates.

Listing B.5: POSCAR file for LaNiBi half-Heusler

```
LaNiBi Half-Heusler
 1.00000000000000
    3.4613141013166100   3.4613141013166100   0.0000000000000000
    0.0000000000000000   3.4613141013166100   3.4613141013166100
    3.4613141013166100   0.0000000000000080   3.4613141013166100
   La    Ni    Bi
   1     1     1
Direct
   0.0000000000000000   0.0000000000000000   0.0000000000000000
   0.2500000000000000   0.2500000000000000   0.2500000000000000
   0.5000000000000000   0.5000000000000000   0.5000000000000000
```

B.1.3 KPOINTS structure

The KPOINTS file defines the density of points on the mesh projected onto the 1BZ. An example of a KPOINTS file is shown in listing B.6. Here, the first and second line specifies that an automatic k-point mesh is generated. The third line generates an automatic mesh centered at the gamma point. The fourth line specifies the number of k-points within the 1BZ along each reciprocal lattice vector, and the last line defines the shift of the mesh. For all calculations in this project, an automatic, Γ-centered k-point mesh is used.

Listing B.6: KPOINTS file

```
Automatic mesh
0
Gamma
1  1  1
0  0  0
```

B.2 VASP files for molecular dynamics on SQS

The SQS supercell for molecular dynamics was generated using the Monte Carlo algorithm discussed in section 3.3.5, which is included in the TDEP method. The starting point is the POSCAR file of the primitive cell defining the position of the element to be substituted and the composition of the structure as shown in listing B.7.

Listing B.7: POSCAR file for generation of SQS supercell

```
Primitive POSCAR for SQS
 1.00000000000000
   0.0000000000000000   3.2696479435326578   3.2696479435326578
   3.2696479435326578   0.0000000000000000   3.2696479435326578
   3.2696479435326578   3.2696479435326578   0.0000000000000000
 ALLOY1  Ni  Bi
 1  1  1
Direct
0.00000000000 0.00000000000 0.00000000000 2 Sc 0.222 La 0.778
0.25000000000 0.25000000000 0.25000000000  site 2: 2 Ni
0.50000000000 0.50000000000 0.50000000000  site 3: 3 Bi
```

A minimal example of a SQS structure is shown in listing B.8.

Listing B.8: POSCAR file describing the SQS supercell

```
SQS
 1.00000000000000
   0.0000000000000000   9.8089438305979737   9.8089438305979737
   9.8089438305979737   0.0000000000000000   9.8089438305979737
   9.8089438305979737   9.8089438305979737   0.0000000000000000
 Sc  La  Ni  Bi
 6  21  27  27
Direct
0.000000000000  0.333333333333  0.000000000000 site 1: 1 Sc
0.000000000000  0.333333333333  0.666666666667 site 2: 1 Sc
      ...             ...            ...
0.000000000000  0.666666666667  0.000000000000 site 7: 2 La
0.000000000000  0.666666666667  0.333333333333 site 8: 2 La
      ...             ...            ...
0.083333333333  0.083333333333  0.083333333333 site 28: 3 Ni
      ...             ...            ...
0.166666666667  0.166666666667  0.166666666667 site 55: 4 Bi
      ...             ...            ...
```

The POSCAR shown in listing B.8 was used for the molecular dynamics calculation, together with the INCAR file specified in B.1.1, and the KPOINTS file defined only for the gamma point (i.e. only one k-point along each lattice vector).

B.3 VASP files for high accuracy calculations on SQS

The POSCAR from listing B.8 together with the force constants extracted after the molecular dynamics calculation, was used to generate 100 structures where the atoms were displaced from their equilibrium position. Thus, the POSCAR files were similar to listing B.8, but with atomic positions slightly deviating from those given in this POSCAR file. The INCAR file defined high accuracy calculations as described in

section B.1.1, and there were two k-points along each lattice vector defined in the KPOINTS file.